Metals and organic adsorbates on GaAs(110): A scanning tunneling microscopy, spectroscopy and luminescence study

Dissertation

zur Erlangung des Doktorgrades der
Mathematisch-Naturwissenschaftlichen Fakultät der
Christian-Albrechts-Universität zu Kiel

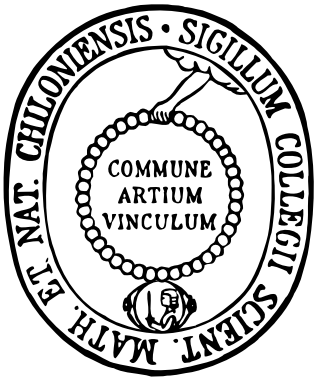

vorgelegt von

Svenja Mühlenberend

Kiel, 2016

Erster Gutachter:	Prof. Dr. Richard Berndt
Zweiter Gutachter:	Prof. Dr. Michael Bauer
Tag der mündlichen Prüfung:	22.03.2016
Zum Druck genehmigt:	_____
gez.	_____
	Prof. Dr. Wolfgang J. Duschl

Typeset in LaTeX 2_ε.

Hiermit erkläre ich an Eides statt, diese Arbeit selbstständig unter der Beratung meiner wissenschaftlichen Lehrer angefertigt und keine weiteren Hilfsmittel, außer den im Text angegebenen sowie den bekannten Nachschlagewerken der Naturwissenschaften, verwendet zu haben. Diese Arbeit wurde weder ganz noch in Teilen an anderer Stelle im Rahmen eines Prüfungsverfahrens vorgelegt. Frühere Promotionsversuche wurden von mir nicht vorgenommen. Die Arbeit ist unter Einhaltung der Regeln guter wissenschafticher Praxis der Deutschen Forschungsgemeinschaft entstanden.
Folgende Teile der Arbeit wurden in wissenschaftlichen Fachzeitschriften veröffentlicht:

- Kapitel 4: Svenja Mühlenberend, Natalia L. Schneider, Markus Gruyters and Richard Berndt, *Plasmon-induced fluorescence and electroluminescence from porphine molecules on GaAs(110) in a scanning tunneling microscope.* Applied Physics Letters **101**, 203107 (2012)

- Appendix A: Svenja Mühlenberend, Markus Gruyters and Richard Berndt, *Fe impurity-induced electronic states at the GaAs(110) surface.* Physical Review B **88**, 115301 (2013)

- Kapitel 5 : Svenja Mühlenberend, Markus Gruyters and Richard Berndt, *Plasmon-mediated circularly polarized luminescence of GaAs in a scanning tunneling microscope.* Applied Physics Letters **107**, 241110 (2015)

Svenja Mühlenberend

Abstract

This thesis reports on scanning tunneling microscopy, spectroscopy and luminescence studies of the interaction of GaAs with nanoscale metallic objects and organic adsorbates.

Surface plasmon polaritons of the tip of a scanning tunneling microscope are used to induce fluorescence from tetraphenylporphine molecules on GaAs(110) surfaces at very low coverages. Light spectra exhibiting vibrationally resolved Q-band transitions reveal that the luminescence is of molecular origin. The emission is not directly induced by the tunneling current. Rather, radiationless energy transfer from plasmon modes of the tip leads to molecular excitation.

The spin transfer efficiency from a remanently magnetized ferromagnet to p-type GaAs across a tunneling barrier is studied. A strong energy dependence of the circular polarization of the recombination luminescence and unexpectedly high maximum values exceeding 50 % are found. A model of a two-parts light generation process with a plasmon induced excitation dominating at low energies, and a superimposed electron injection luminescence becoming dominant at energies of ≈ 100 meV above the conduction band edge is proposed. The degree of circular polarization above 50 %, seemingly contradictory to the well-known selection rules, is tentatively explained in terms of a dopant induced broadening of the acceptor level and its merging with the valence band.

Evidence is presented that individual phthalocyanine molecules on unpassivated GaAs(110) largely preserve their electronic characteristics. The tip of an STM can be used to manipulate the band structure of the substrate, leading to a reversible modification of the charge state of the molecule.

The room temperature growth of the planar FePc and the non-planar AgPc on GaAs(110) is discussed. For both species, unidirectionally growing islands with very high long-range order are found, and their electronic as well as structural properties are examined. For AgPc, irreversible switching between different molecular appearances is observed and attributed to a transition between a non-planar and a planar conformation.

Zusammenfassung

Diese Arbeit untersucht die Interaktion von GaAs mit Metallen und organischen Adsorbaten mithilfe von Rastertunnelmikroskopie, -spektroskopie und -lumineszenz.

Oberflächenplasmonen auf der Spitze eines Rastertunnelmikroskops werden genutzt, um Tetraphenylporphin bei sehr niedrigen Bedeckungen zur Fluoreszenz anzuregen. Vibrationsaufgelöste Q-Band-Übergänge in Lumineszenzspektren belegen, dass es sich um Fluoreszenz molekularen Ursprungs handelt. Die Emission wird nicht direkt vom Tunnelstrom sondern durch strahlungslosen Energietransfer von Plasmonenmoden der Spitze angeregt.

Die Effizienz des Spintransports von einem remanent magnetisierten Ferromagneten über eine Tunnelbarriere hinweg in p-GaAs hinein wird untersucht. Eine starke Abhängigkeit der Zirkularpolarisation der Rekombinationslumineszenz und unerwartet hohe Maximalwerte oberhalb von 50 % werden beobachtet. Eine Erklärung basierend auf einem zweiteiligen Lichterzeugungsprozess wird vorgeschlagen, bestehend aus einer bei niedrigen Spannungen dominierenden plasmoneninduzierten Anregung und einer überlagerten Injektionslumineszenz, welche ab Spannungen von ≈100 meV oberhalb der Leitungsbandkante bestimmend wird. Der Zirkularpolarisationsgrad oberhalb von 50 % scheint den wohlbekannten Auswahlregeln zu widersprechen. Dies wird im Rahmen einer möglichen Verbreiterung des Akzeptorniveaus und dessen Vermischung mit Valenzbandzuständen erklärt.

Es wird gezeigt, dass einzeln adsorbierte Phthalocyanin-Moleküle auf unpassiviertem GaAs(110) ihre elektronischen Eigenschaften zum Großteil bewahren. Die Spitze eines Rastertunnelmikroskops kann verwendet werden um die Bandstruktur des Substrats zu beeinflussen und so den Ladungszustand des Moleküls reversibel zu verändern.

Das Wachstum des planaren FePc und des nichtplanaren AgPc auf GaAs(110) bei Raumtemperatur wird behandelt. Beide Spezies zeigen ein unidirektionales Inselwachstum mit ausgeprägter langreichweitiger Ordnung, und sowohl ihre elektronischen als auch ihre strukturellen Eigenschaften werden untersucht. AgPc zeigt irreversible Schaltvorgänge zwischen verschiedenen Erscheinungsbildern, die mit einem Übergang von einer nicht-planaren zu einer planaren Molekülkonformation erklärt wird.

Contents

List of Abbreviations

AFM	Atomic Force Microscope / Microscopy
AgPc	Silver Phthalocyanine
CdS	Cadmium Sulfide
CuN	Copper Nitride
CuPc	Copper Phthalocyanine
DFT	Density Functional Theory
FePc	Iron Phthalocyanine
GaAs	Gallium Arsenide
Ge	Germanium
GMR	Giant Magnetoresistance
HOMO	Highest Occupied Molecular Orbital
HOPG	Highly Oriented Pyrolytic Graphite
Ir	Iridium
LDOS	Local Density of States
LT	Low Temperature
LUMO	Lowest Occupied Molecular Orbital
MgPc	Magnesium Phthalocyanine
NaCL	Sodium Chloride
NDC	Negative Differential Conductance
PbPc	Lead Phthalocyanine
Pc	Phthalocyanine
Si	Silicon
SmCo	Samarium Cobalt
SnNc	Tin Naphthalocyanine
SnPc	Tin Phthalocyanine
STL	Scanning Tunneling (induced) Luminescence
STM	Scanning Tunneling Microscope / Microscopy
TPP / H_2TPP	Tetraphenylporphyrin
UHV	Ultrahigh Vacuum
WKB	Wentzel-Kramers-Brillouin
ZnPc	Zinc Phthalocyanine

List of Figures

1 Introduction

Over the course of the last decades, the compound semiconductor gallium arsenide (GaAs) has been studied extensively. A massive amount of information can be found in textbooks, reviews, and scientific publications, e.g. in [1–7, and references therein]. Its unique electronic and optical properties, notably a high electron mobility and efficient photon-electron interconversion, have led to a widespread use in modern electronics devices, either as a bulk material or in heterostructures. Compounds with additional elements like aluminum or indium are also used extensively. Examples for GaAs-based devices include high frequency transistors [8, 9], light emitting diodes (LED) [10, 11] and laser diodes [12–14], photodetectors for the near infrared [9] and solar cells [15, 16].

Due to the peculiar band structure of GaAs, it is widely employed in spintronic devices. By illumination with circularly polarized light, spin-selective pumping of electrons to the conduction band can be achieved [17]. The reverse process, namely the injection of spin-polarized carriers and the subsequent detection of the circular polarization of the recombination luminescence, make GaAs a valuable "spin detector" [18–22]. When injecting a spin polarized current via a metallic interface, however, plasmonic excitations within the metal provide an additional spin-pumping mechanism that is not yet fully understood [23, 24].

Just like spintronics, molecular electronics is a topic of intense research in the area of semiconductors. Organic molecules have proven to add highly beneficial functionality to conventional electronics. For example, organic light emitting diodes (OLED) are being produced on a large scale, allowing for a competitive fabrication of flexible displays. Organic field effect transistors (OFET) [25–27], on the other hand, are still under active development. One of their major issues is the low electron mobility within the organic layers. As self-assembled, highly ordered molecular structures have shown

orders of magnitude higher mobilities than disordered films, they are of particular interest in current examinations [28–33, and references therein].

Understanding the interplay of GaAs with organic and inorganic adsorbates or nanoscopic entities promises to provide insight into fundamental interface properties. This thesis investigates the interaction of GaAs with different nanoscale systems by means of scanning tunneling microscopy (STM), scanning tunneling spectroscopy (STS) and scanning tunneling induced luminescence (STL):

In chapter 2, basic properties of GaAs and the employed organic molecules (porphine and different phthalocyanines) are presented and the principles of STM, STS and STL are explained.

Chapter 3 contains a brief description of the experimental setup.

In chapter 4, evidence for the fluorescence of individual porphine molecules adsorbed on GaAs(110) is presented. Interestingly, the molecules are excited by a surface plasmon on the tip of an STM and not by the tunneling current, as fluorescence is detected while the tip is in nm distance to the closest molecules. This surface plasmon can also be used to excite electron-hole pairs in GaAs. Chapter 5 shows that upon recombination of these electron-hole pairs, highly polarized electroluminescence can be emitted. This effect competes with electroluminescence stemming from electron injection and dominates only at very low bias.

Interaction between phthalocyanine (Pc) molecules and the GaAs(110) surface is sufficiently strong to prevent lateral diffusion during scanning at low temperatures, but weak enough to preserve molecular electronic characteristics to a large extent. Chapter 6 reports on the charging of single silver phthalocyanine (AgPc) molecules on GaAs(110). It is explained in terms of a tip-induced band bending (TIBB) of GaAs and a resulting shift of the lowest unoccupied molecular orbital (LUMO) across the sample Fermi level.

When phthalocyanines are deposited at room temperature, intermolecular π-π interaction leads to self-assembly into highly ordered monolayer islands. Depending on the coverage as well as on the central metal atom, different growth modes are found. In chapter 7, iron Pc (FePc) and AgPc islands on GaAs are studied. At coverages of ≈ 10 %, FePc is found to assemble into very long islands that grow unidirectionally in a zigzag manner. Molecules within the island stand upright, promising efficient charge transfer parallel to the surface through π-π coupling. AgPc, being a non-planar molecule, shows slightly different behavior. It is studied at comparable coverages, where very thin islands of upright standing molecules are formed. Three different regions with varying spectroscopic signatures and apparent heights are identified. Irreversible switching of two of the regions into the remaining type is observed.

Further measurements that were conducted over the course of this thesis and that have been published will not be discussed in depth. A publication on iron (Fe) impurity-induced electronic states at the GaAs(110) surface is annexed in appendix A. It discusses spectra of the differential conductance taken on single Fe atoms incorporated into the first Ga layer of GaAs(110). They reveal distinct peaks that are assigned to hybridized As-Fe states.

Measurements on the morphology of iron-bis(dihydrobis(pyrazolyl)borate)-1,10--phenanthroline (Fe(bpz)2(phen)) on GaAs were contributed to a publication by Gopakumar et al. [34]. Due to an enhanced molecule-substrate interaction on GaAs(110) as compared to Au(111), intact molecules as well as fragments could be imaged and identified. Thereby, the rate of Fe(bpz)2(phen) decomposition upon deposition could be estimated and an assignment of the fragments to molecular building blocks could be made.

2 Fundamentals

2.1 Gallium Arsenide

The general electronic and optical virtues of GaAs as well as its current and prospective technological use have been discussed in the introduction. In the following section, specific structural, electronic and optical characteristics that are crucial for the understanding of the presented data will be explained in more detail.

2.1.1 Crystal Structure

GaAs is a binary III-V semiconductor with a zinc blende crystal structure and a lattice constant of 5.65 Å. Each Ga and each As atom form sp^3-hybridized bonds to four neighboring atoms of the other kind, each bond containing two electrons. Ga with an electronic configuration of $4s^2 4p^1$ contributes 3 electrons, whereas As with a configuration of $4s^2 4p^3$ contributes 5. The charge, however, is not distributed equally between Ga and As. In fact, Ga donates roughly 0.5 electrons to As [35], leaving the latter slightly negatively charged. This kind of bonding is neither completely covalent nor ionic, but an intermediate form.

Throughout this thesis, the (110) surface of GaAs is used as the sample material. It can easily be prepared by cleaving in vacuo, because it contains the same number of Ga and As atoms, leaving it with no net charge. The resulting planes are usually very clean and atomically flat on a large scale. The GaAs(110) plane relaxes in a rippled geometry where the As atoms protrude from the surface [36–39] (see fig. 2.1). Due to missing neighbors, Ga as well as As form dangling bonds at the surface. It has been shown experimentally and theoretically that the electrons on the surface pair up at the As site [1, 6, 36, 40, 41]. This leads to a filled surface state located at the As sites

and an empty surface state located at the Ga sites. Those two states are rather close to the valence and conduction band edges, respectively [41]. Therefore, at moderate tunneling bias, either As or Ga atoms appear as protrusions in an STM topograph, whereas the other kind appears as a depression [6]. A topograph of the surface is shown in figure 2.2, where the As atoms appear as bright and well-separated protrusions at negative bias.

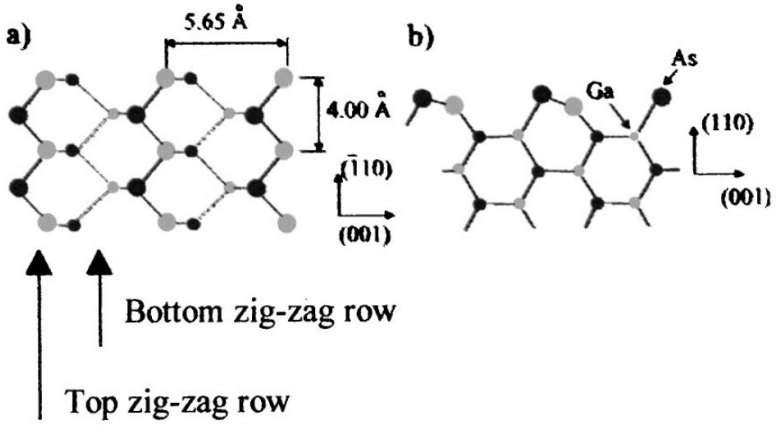

FIGURE 2.1: The crystal structure the (110) surface of GaAs. (a) Top view. (b) Side view. Taken from [39].

2.1.2 Band Structure and Tip Induced Band Bending

GaAs is a direct band gap semiconductor with a fundamental gap E_g of ≈ 1.5 eV. As all sp^3-hybridized bonds are completely filled, the valence band of GaAs is fully occupied, whereas the conduction band is empty at zero temperature. The bulk band structure around the Γ-point is sketched in fig. 2.3 (a), which has been adapted from [17]. At the Γ-point, the valence band is subdivided into degenerate heavy and light hole bands ($p_{3/2}$ and $p_{1/2}$, respectively), and the split-off band, which is lowered by $E_{SO} = 340$ meV due to spin orbit coupling. In the case of Zn-doped p-type GaAs, the Fermi level is close to the valence band edge (24 meV above the band edge [42]).

Fig. 2.3 (b) shows the spin-resolved energetic positions at Γ. The allowed optical transitions under irradiation with left (σ^+) and right (σ^-) circularly polarized light are denoted with their respective relative transition probabilities. Optical transitions will be discussed in more detail in sections 2.1.3 and 2.7.2.

In STM experiments, the presence of a metallic tip close to the surface of a semiconductor causes some peculiarities. Due to a lack of free charge carriers, the electric field of the tip is only poorly screened and penetrates into the semiconductor [43, 44]. Therefore, a noticeable fraction of the electric potential between tip and sample drops

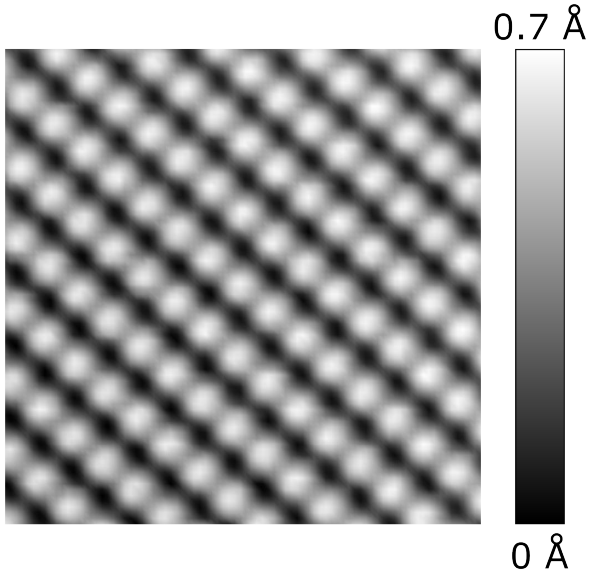

Figure 2.2: STM topograph of the clean GaAs(110) surface (I_T = 30 pA, V_T = -2.8 V). Bright protrusions identify the location of Arsenic atoms.

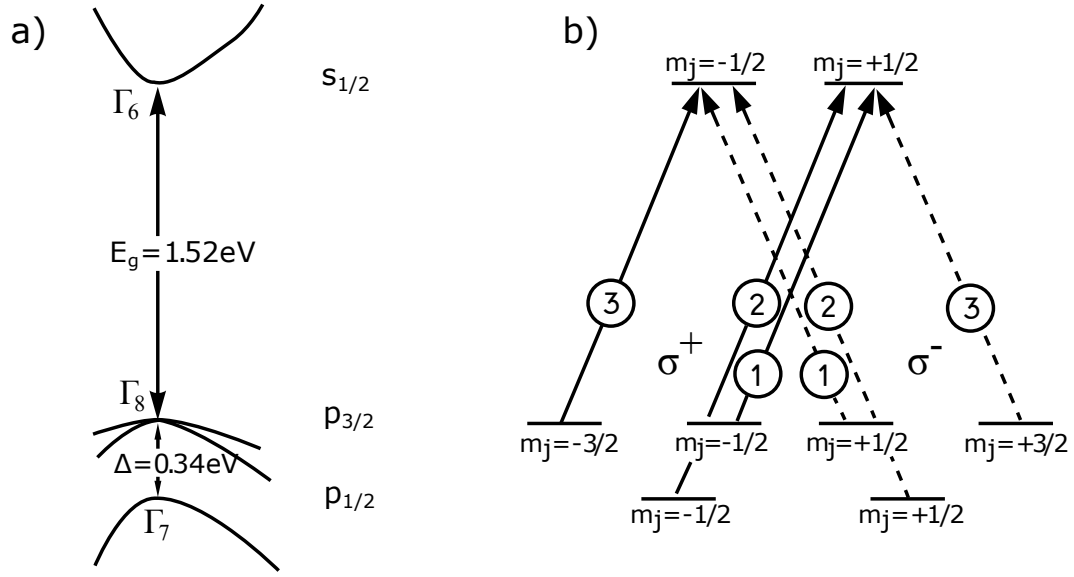

Figure 2.3: (a) Bulk band structure of GaAs around the Γ-point, adapted from [17]. (b) Spin-resolved energy levels at the Γ-point with possible optical transitions under the irradiation with circularly polarized light. Circled numbers denote relative transition probabilities.

within the upper layers of the sample. This can be described as a bending of the near-surface bands. This so-called tip-induced band bending (TIBB) leads to considerable changes of the energetic positions of valence and conduction bands. Figure 2.4 shows a sketch of the conduction and valence band edges close to the surface. Depending on the tunneling bias, they are bent either downwards or upwards. For high tunneling

bias, the band edges can cross the Fermi level, leaving valence states unoccupied and conduction states occupied at the surface.

The exact magnitude and lateral extent of the bending depends not only on the bias, but also on parameters that are subject to a relatively large uncertainty. This includes the geometry of the tip apex, the distance between tip and sample, the doping density, the temperature and the contact potentials of tip and sample [43]. The TIBB can, however, be estimated with the program *SEMITIP*, a numerical simulation written by Randall M. Feenstra [45]. As mentioned before, many parameters are not known exactly, thus the results of the simulation must be taken with precaution. Figure 2.5 shows the results of a calculation with *SEMITIP*. The tip-sample separation was set to 7 Å and the acceptor concentration to $2 \times 10^{19}\ cm^{-1}$. The plot shows the calculated surface potential (i.e. the potential drop between surface band edge and bulk band edges) versus tunneling bias. For negative bias, the bending is much more pronounced than for positive bias. Flat bands are obtained at around 1.2 V.

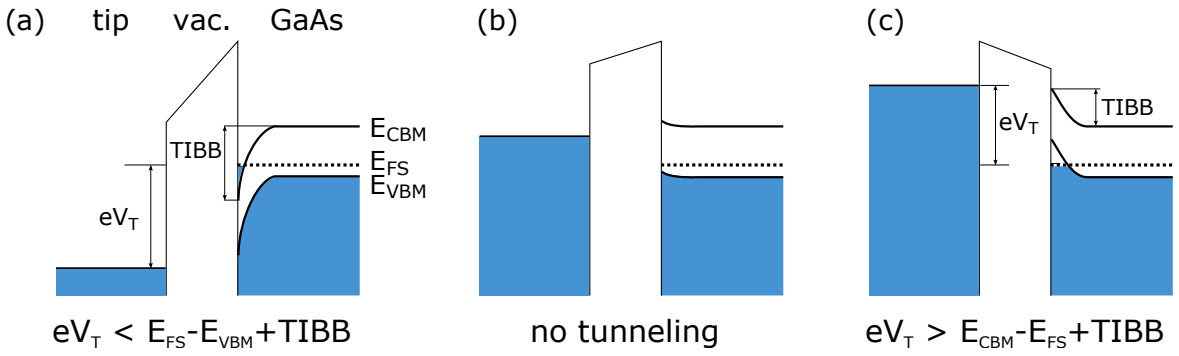

FIGURE 2.4: Schematic of the bending of the near-surface bands in the presence of a metallic tip. Three regions are distinguished: (a) $eV_T < E_{FS} - E_{VBM} + TIBB$: downward band bending. The conduction band can be pulled below the Fermi level, leaving it partially populated close to the surface. (b) No states accessible to tunneling. (c) $eV_T > E_{CBM} - E_{FS} + TIBB$: upward band bending. The valence band maximum can be shifted across the Fermi level, leading to empty states in the valence band. Energies are not to scale.

Due to the potential drop within the sample, electrons tunneling from the tip to the conduction band need an energy that is higher by the amount of TIBB, compared to the case without band bending. This shifts the onset of the tunneling current at the band edge towards higher voltages. At negative bias, the situation is analogous. In dI/dV-spectra, this causes an apparent broadening of the band gap. This effect is particularly strong at the negative bias side, as the surface potential there is much larger than at the positive side (compare fig. 2.5). As the TIBB is sensitive to the tip shape, spectra vary substantially with different (microscopic) tips. Fig. 2.6 shows a characteristic dI/dV-spectrum. The band gap is marked as a shaded area, and it is clearly seen that at negative bias, tunneling does not occur until a bias of $\lessapprox$ -0.3 V.

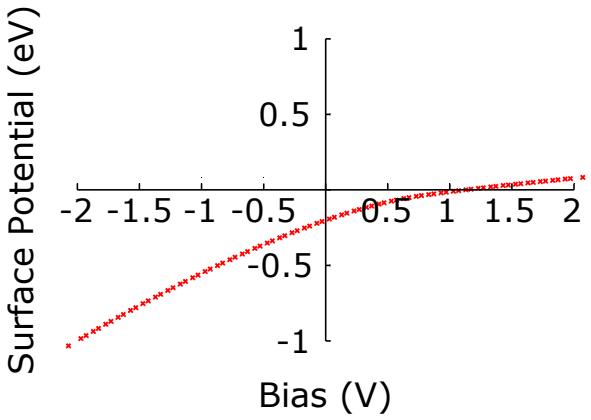

Figure 2.5: Simulated TIBB as a function of tunneling bias, calculated using *SEMITIP* [45]. See text for parameters.

In other words, an additional potential barrier V_{TIBB} of the magnitude of the TIBB within the semiconductor suppresses or strongly impairs tunneling at energies close to the band gap.

2.1.3 Optical Orientation in GaAs

Optical orientation in GaAs means that a spin polarized electron population is created in the conduction band by irradiation with circularly polarized light of energy E_{in} with $E_g < E_{in} < E_g + E_{SO}$ [46]. Consider the following example: when unpolarized electrons in the valence band are irradiated with σ^+-light, transitions from m_j=-3/2 to m_j=-1/2 and from m_j=-1/2 to m_j=+1/2 satisfy the selection rule of $\Delta m = +1$ (see fig. 2.3 (b)). As the former transition is three times as likely as the latter [17], three times as many electrons will populate the m_j=-1/2 level, compared to the m_j=+1/2 level. The total spin polarization in the conduction band amounts to

$$P = \frac{n(m_j = -1/2) - n(m_j = +1/2)}{n(m_j = -1/2) + n(m_j = +1/2)} \tag{2.1}$$

with $n(m_j)$ the number of electrons in the corresponding level. This leads to a maximum degree of polarization of 50 %.

In contrast, in the case of the injection via a spin polarized current, electrons are directly and selectively placed in one of the two conduction band levels, leading to a maximum attainable polarization of the conduction electrons of 100 %. When they recombine, the same weighted transitions as for optical orientation apply, and the polarization of the emitted light corresponds to the one needed for the orientation process. As holes will preferably be located in the uppermost valence bands, recombination will mostly take place between the conduction band edge and the heavy and light hole bands, and not the split-off band. This holds particularly true for p-type GaAs. The

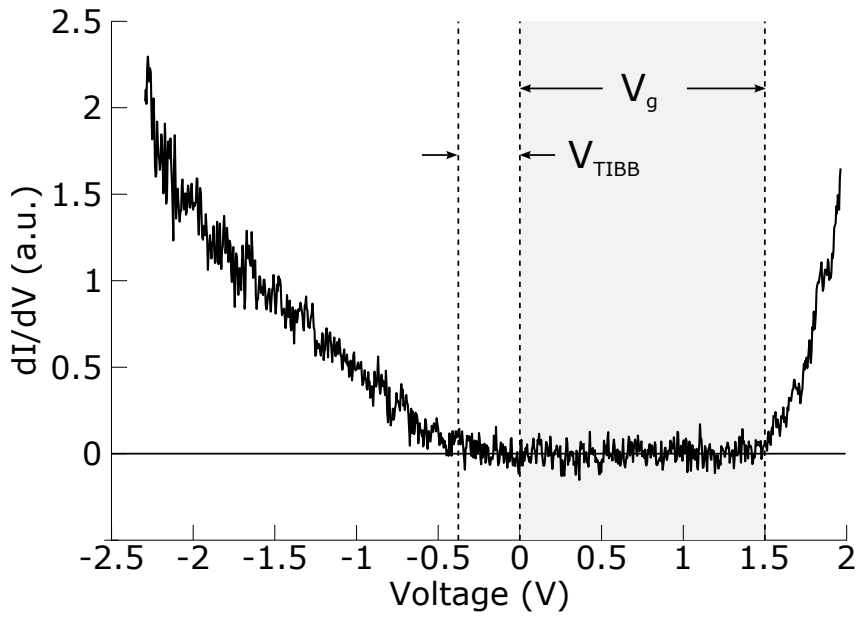

FIGURE 2.6: dI/dV-spectrum taken on GaAs. The shaded area marks the band gap. Tunneling is suppressed in the band gap as well as for negative biases $\gtrapprox$ -0.3 V due to an additional potential barrier resulting from TIBB.

3 to 1 ratio of the allowed transitions will then lead to a maximum degree of circular polarization of the recombination luminescence of 50 % (as opposed to a maximum of 25 % in experiments where electrons are optically pumped to the conduction band first). Depending on the spin of the injected electrons, the luminescence will be either left or right circularly polarized. This means that by analyzing the recombination luminescence, the spin polarization of the injected electrons can be inferred [47].

Different conventions exist as to how *left* and *right* are to be interpreted in a physical sense. One defines the sense of rotation as seen from the observer, the other as seen from the source, yielding contrary denominations. Throughout this thesis, the actual direction of the circular polarization is not relevant. Thus, instead of using the terms left and right, absolute values of the degree of circular polarization are given to facilitate readability.

2.2 Porphyrins

Porphyrins are macrocyclic aromatic organic compounds composed of four pyrrole rings connected via methine bridges. They are building blocks for many biological substances like hemoglobin, as well as for tailored supramolecular assemblies. Fig. 2.7 (a) shows the chemical structure of Tetraphenylporphyrin (TPP), which consists of a central porphine unit with four phenyl groups attached. It has strong absorption bands in the

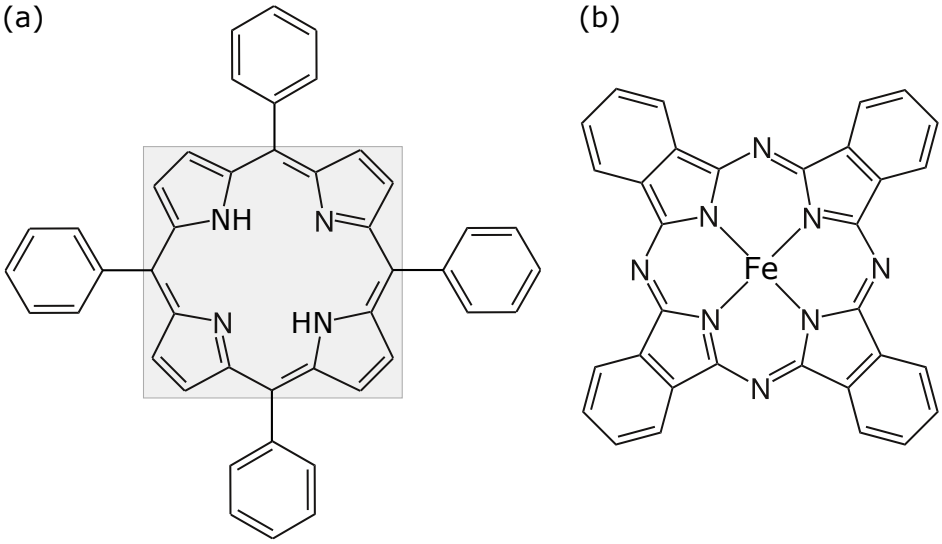

Figure 2.7: (a) Structure diagram of Tetraphenylporphyrin. The shaded area marks the porphine building block. (b) Structure diagram of iron phthalocyanine.

visible spectral range (so-called S and Q-bands) and shows red fluorescence [48]. Due to its stability it can be sublimed under UHV conditions.

2.3 Phthalocyanines

Phthalocyanines (Pc) are a group of aromatic macrocyclic organic dyes that are closely related to porphyrins. Due to their exceptional chemical and thermal stability that allows for UHV sublimation, they are easily prepared in STM experiments. Their structure is well-understood and they are available in a great variety. They form complexes with many elements, including magnetic as well as non-magnetic metals. A large share of the world production is used for dyes and pigments, as phthalocyanines exhibit brilliant and intense blue and green colors. This is due to a pronounced absorption band in the 600 to 700 nm region (Q-band), caused by the excitation of an electron from the HOMO to the LUMO. This transition also enables their use in photovoltaics [49].

Fig. 2.7 (b) shows the chemical structure of a metalated phthalocyanine, here with a central iron atom. Most phthalocyanines are planar, although some centers (Ag, Sn, Pb) protrude from the plane due to their size. In this thesis, mainly iron PC (FePc) and silver PC (AgPc) have been examined.

A comprehensive discussion of the properties and applications of phthalocyanines is well beyond the scope of this work. The reader is thus referred to the abundant literature on the topic [e.g. 50–57].

2.4 Scanning Tunneling Microscopy

After its invention in 1982 by Gert Binnig and Heinrich Rohrer [58–60], STM has found its way into surface science at an incredible pace. It enabled for the first time real-space imaging of conductive surfaces with atomic resolution as well as spectroscopy of the energetic structure of surfaces, molecules and other adsorbates. This was accomplished by scanning an atomically sharp tip in nanometer distance across a surface. The gap between tip and sample (vacuum, air or a liquid) acts as an energetic barrier whose height is determined by the work functions of the tip and sample materials. In a classical picture, electrons with a lower kinetic energy cannot pass this barrier. In quantum mechanics, however, the wave nature of electrons is taken into account. For energies below the barrier height, the electron's wave function decays exponentially inside the barrier. Once the gap becomes so narrow ($\approx$ 1 nm) that the electron wave functions in the tip and in the sample overlap, transmission through the barrier becomes possible. This is called the quantum mechanical tunneling effect.

The superior resolution of STM can only be understood when looking at the underlying principles. Theories for tunneling through a barrier have been developed long before the STM. As only for the simplest cases can the Schrödinger-equation be solved analytically, approximations are usually made. The semiclassical WKB (Wentzel-Kramers-Brillouin) approximation describes tunneling through a one-dimensional potential barrier of arbitrary shape [61–63]. For a trapezoidal barrier, it yields a tunneling probability (or transmission coefficient) that depends exponentially on the distance z between tip and sample:

$$T(z,V,E) = e^{-2\kappa z},\ \kappa = \sqrt{\frac{2m}{\hbar^2}\left(\frac{\phi_S+\phi_T}{2}+\frac{eV}{2}-E\right)} \tag{2.2}$$

V is the bias, E is the electron energy, m is the electron mass, and ϕ_S and ϕ_T are the work functions of sample and tip, respectively.

In the limit of low temperatures and voltages, the tunneling current can then be written as [64]

$$I \propto T(z,V,E)V \tag{2.3}$$

Inserting typical work function values of metals of 5 eV into equation 2.3, we find that the current decreases by roughly one order of magnitude when the distance z is increased by 1 Å. Applied to STM, this strong susceptibility to distance changes is responsible for the high spatial sensitivity perpendicular to the surface.

Although the theory given above is useful in many cases, it lacks important aspects of STM measurements. It neglects, e.g., the electronic wave functions of tip and sample. In 1983, shortly after the invention of STM, Tersoff and Hamann published an improved model [65] based on Bardeen's tunneling theory [66]. There, the tip and sample states are modeled as independent wave functions, with the bias voltage being

a weak perturbation. The approach includes a temperature dependence through the Fermi-Dirac distribution. The tunneling current can be expressed as [67]

$$I = \frac{4\pi e}{\hbar} \int_{-\infty}^{+\infty} [f(E_{FT} - eV + \epsilon) - f(E_{FS} + \epsilon)] \; \rho_T(E_{FT} - eV + \epsilon)\rho_S(E_{FS} + \epsilon) \; |M|^2 \; d\epsilon \tag{2.4}$$

where $f(E)$ is the Fermi-Dirac distribution[1], ρ_T and ρ_S are the LDOS of tip and sample, respectively, and M is the Bardeen tunneling matrix element. For low temperatures, the Fermi-Dirac distribution can be approximated with a step function. The integration can then be confined to the range $0 < \epsilon < \text{eV}$:

$$I = \frac{4\pi e}{\hbar} \int_{0}^{eV} \rho_T(E_{FT} - eV + \epsilon)\rho_S(E_{FS} + \epsilon)|M|^2 d\epsilon \tag{2.5}$$

The tunneling current is now basically proportional to the convolution of the LDOS of tip and sample. Further simplification can be achieved under the assumptions of a flat tip DOS and a slowly varying sample DOS in the energy interval of interest, a spherical symmetry of the tip state that dominates tunneling, and the tunneling matrix element not depending on the energy [67]:

$$I \approx \frac{4\pi e}{\hbar} \rho_T |M|^2 \int_{0}^{eV} \rho_S(E_{FS} + \epsilon) d\epsilon \tag{2.6}$$

We see that the assumption regarding the tip lead to a simple relation between tunneling current and LDOS of the sample. This means that when tunneling at a constant current, contours of constant sample LDOS are traced. Although the assumptions listed above may seem arbitrary, this model has proven to be very valuable in the interpretation of STM topographs.

It does have limitations, though. In particular the assumption of a purely s-wave-like tip leads to disagreement between theory and experiment. The resolution of features smaller than a few Å as well as strong apparent corrugations cannot be explained without the inclusion of p- or d-wave states [67]. In fact, it has been calculated that for most metals, the contribution of the s-wave-state at the Fermi level is expected to be rather weak compared, e.g., to p_z- or d_{z^2}-states [68–70]. Furthermore, when tunneling on semiconductors, the low-voltage assumption is usually violated. In this case, enhanced WKB-approaches are typically employed [71].

[1] The temperature dependence of f has not been indicated for the sake of readability.

2.5 Scanning Tunneling Microscopy Modes

Depending on the requirements for scanning speed and noise resistance as well as on the surface roughness of the sample, STM offers two scanning modes [67]. For high-speed imaging, the tip is scanned across the surface at a constant distance while the tunneling current is recorded. Due to the known exponential dependence of distance and current, a topographic map of the surface can be calculated. This is called the constant height mode. As no feedback control is needed, this mode allows for the highest scanning speeds, as required, e.g., in video STM [72, 73]. Its major drawback is the great demand on surface smoothness, as the tip will collide with any obstacle with a corrugation larger than the tip-sample distance. Furthermore, the exponential dependence of current and distance constricts the scan range in the z-direction to a narrow range. Thus, it is restricted to very smooth, untilted surfaces.

The second operating mode is the so-called constant current mode. As the name suggests, the tip is scanned across the surface, while the distance is constantly adjusted so as to hold the current constant. This requires a fast feedback loop that reads the current, compares it to a setpoint value, and readjusts the z position. This procedure is usually repeated several times per imaging point, and possibly in between imaging points to prevent tip collisions. The z outputs are stored and used as a representation of a topographic map. Due to the time consumption of the feedback loop, the constant current mode is much slower than the constant height mode. It is, however, also much more robust, as even large topographic features like multiple step edges or large molecules can be circumscribed. The z range is only limited by the total travel of the z piezo. In this thesis, all topographs shown were recorded in the constant current mode.

2.6 Scanning Tunneling Spectroscopy

2.6.1 dI/dV Spectra

The primary intention behind the development of STM was to perform spectroscopy with nanoscale resolution [60]. However, thanks to the unanticipated variety of new experiments that STM rendered possible, it took several years until the first studies that made use of Scanning Tunneling Spectroscopy (STS) were published [74–78].

STS exploits the fact that, as seen from equation 2.5, the tunneling current is proportional to the convolution of the DOS of tip and sample. Differentiating I_T with respect to V and assuming a constant tip DOS, the differential conductance $\frac{dI}{dV}$ is proportional to the sample LDOS. Hence, this mode of spectroscopy is referred to as dI/dV spectroscopy. In order to obtain quantitative information about the sample LDOS, different normalization procedures have been proposed, like, e.g., a division by the conductance [76]. In most experimental situations, however, the tip DOS will not be flat. In order to obtain a largely featureless DOS, different tip preparation procedures have been proposed. They are based on locally heating the tip apex by field emission [76] or by gently touching the surface with the tip [79]. These methods

are often able to improve tip stability and yield a reasonably flat tip DOS. Nevertheless, in most cases the tip will be less sharp and imaging quality will be impaired.

As the tunneling current is prone to electronic noise, a direct derivation of I_T is usually not ideal. Instead, the derivation is usually performed by modulating the tunneling bias V_T with a small, sinusoidal signal ΔV of high frequency, and measuring the fluctuation ΔI of I_T at that frequency. As ΔI is proportional to the difference quotient $\frac{\Delta I}{\Delta V}$, this gives an approximation of the derivative. The measurement of the current fluctuation is usually carried out with the lock-in technique [80].

A spectroscopic measurement at constant height is carried out by opening the feedback loop and then ramping up or down the voltage while simultaneously measuring the lock-in signal. Care has to be taken that the waiting time at each voltage step is matched with the settling time for lock-in detection. up or down the voltage while simultaneously measuring the lock-in signal. Care has to be taken that the waiting time at each voltage step is matched with the settling time for lock-in detection.

Broadening of spectral features is expected both from thermal and instrumental effects [67, 81]. Thermal broadening is due to the temperature dependence of the Fermi-Dirac distribution, and is of the order of 3.5 $k_B T$ ($\approx$ 1.5 meV at 5 K). Broadening due to voltage modulation can be estimated as 1.7 V_m [81], with V_m being the modulation voltage.

2.6.2 dI/dV Maps

In addition to dI/dV spectroscopy at a single position, STM offers the possibility to record spatial maps of the differential conductance. To this end, at each point of a topograph the differential conductance at one specific bias value[2] is measured. As this method is time-consuming, it requires stable measurement conditions and is thus mostly limited to low temperatures where drift is negligible. It provides the unique possibility of mapping the differential conductance and thus the LDOS of nanoscale systems like, e.g., single ad-atoms or defects [82, 83], molecules [84–86] or other nanoscale structures [87–89].

2.7 Scanning Tunneling Induced Luminescence

Not long after the invention of STM, pioneering experiments of Gimzewski, Berndt and co-workers demonstrated for the first time photon emission from an STM junction [90–92]. In rapid succession, light emission from noble metals [93], transition metals [90], bulk semiconductors [90, 94] and semiconductor heterostructures [95] was reported. Later on, the detection of fluorescence from molecules [96] and nanostructures [97–99] was achieved. Theories have been developed shortly after the experimental demonstrations [100–102]. Though, eventually, all light emission processes are attributed to

[2]Other measurement electronics allow for the recording of a complete spectrum at each point of the topograph.

the tunneling current, the underlying principles differ strongly. In the following, those processes will be categorized and discussed.

2.7.1 Plasmon-induced Luminescence in STM

According to the Drude-Sommerfeld theory, conduction electrons in metals can move freely between the positively charged atomic nuclei [103]. At the surface, those free electrons oscillate collectively when irradiated with light of suitable frequency [104]. In a quasi-particle description, this collective excitation is called a surface plasmon polariton. Their resonance frequency, the so-called plasma frequency, is dependent on the material. For noble metals, it is in the visible range [105].

It has been known long before the invention of STM that electrons impinging on metals can excite surface plasmon polaritons that decay radiatively on rough surfaces [see 106, and references therein]. However, when STL was developed, it was quickly noticed that strongly enhanced integral photon yields (i.e. the rate of injected electrons to emitted photons) in the range of 10^{-4} photons/electron are obtained when a metallic tip is positioned in nm distance to a metallic surface [93, 105]. This enhancement was attributed to the radiative decay of localized, tip induced plasmon (TIP) modes between tip and sample. They are excited by a strong interaction with inelastically tunneling electrons. The proximity of the tip causes a loss of translational invariance (comparable to the case of a rough surface), giving rise to an efficient TIP to photon conversion [100, 105].

Each metal has characteristic plasmonic emission spectra and photon yields. Silver is among the most efficient emitters with yields up to 10^{-3} photons/electron [107]. The yield as well as the spectral distribution of light are highly voltage dependent. The energetic range for the emitted photons is restricted to energies below the cutoff energy[3] $h\nu_{max} = |eV_T|$. Higher voltages thus lead to a shift of the emission threshold. This threshold does not necessarily need to be the onset of luminescence; In case no TIP modes are present at this energy, no emission is expected either.

For the yield, two competing processes must be considered [100, 109]: On the one hand, above threshold, the energy range available for photon emission processes increases with $|V_T|$. On the other hand, higher voltages at constant current lead to a retraction of the tip, reducing inelastic tunneling. At voltages around ≈ 4 V, the voltage-distance characteristic changes from linear to larger than quadratic. As the probability for inelastic tunneling is roughly inversely proportional to this, the decrease due to tip retraction then quickly outperforms the increase due to an augmenting energy range. In summary, this means that for small voltages, the yield increases with voltage, but for biases above ≈ 4 V it decreases again.

[3]Strictly speaking, this is only valid for one-electron processes. Higher energies can be obtained due to multi-electron excitations [108], sometimes misleadingly denominated as "forbidden" emission. As those processes are several orders of magnitude less efficient, they will not be considered here.

2.7.2 Electroluminescence

Electroluminescence in semiconductors is caused by the radiative recombination of electrons with holes (see fig. 2.8). In direct band gap semiconductors like GaAs or cadmium sulfide (CdS), the conduction band minimum and the valence band maximum are at the same position in k-space. This leads to relatively high internal quantum efficiencies (the rate of injected electrons to generated photons) close to unity at cryogenic temperatures [14, 110–112]. In contrast, indirect band gap semiconductors like silicon (Si) or germanium (Ge) have quantum efficiencies that are several orders of magnitude lower [113], as the k-mismatch needs to be compensated for by a simultaneous phonon emission.

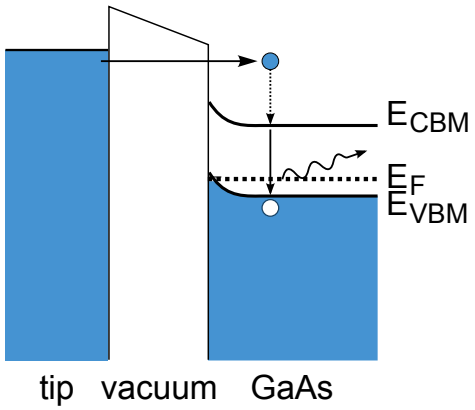

Figure 2.8: Schematic of electroluminescence generation. Electrons tunneling from the tip into the sample relax to the conduction band minimum and recombine with holes at the valence band maximum or the acceptor level under emission of a photon. Energies are not to scale.

As described in section 2.1.3, when spin-polarized electrons recombine, circularly polarized light is emitted. This is, in a way, the inverse of the optical orientation mechanism. Due to the degeneracy of the heavy and light hole bands (compare fig. 2.3 (b)), it is generally assumed that the maximum attainable degree of circular polarization is 50 %, corresponding to a 100 % spin polarized electron population in the conduction band. There are, however, exceptions to this rule. Several effects are known to lift the degeneracy, like strain and stress [114–116] or heterostructured geometries like quantum wells or quantum dots [117]. It is also known that heavy doping (above $\approx 7 \times 10^{18} cm^{-3}$) can have a substantial effect on the band structure [118–122]. The acceptor level broadens and eventually merges with the valence band, or rather, as reported in [119], with the heavy hole band. In this case, the degeneracy of heavy and light hole bands could be lifted. In this case, the limit of 50 % circular polarization is not valid any more. Instead, a maximum of 100 % is expected.

This maximum value, however, would only be measured if solely those photons were detected that propagate along the tip's magnetization axis (and, thereby, the orientation of the electrons spins). In practice, this would correspond to a detection axis collinear with the tip's axis. In our setup, however, the light is collected at an angle of 60° towards the surface normal. Our data thus require correction. Figure 2.9 sketches the geometric situation of the light detection. Due to the high index of refraction of GaAs of 3.66 at 850 nm, total reflection is achieved already at 15.9° towards the surface normal. According to Snell's Law, the detector, placed at an angle of 60°, gathers light that propagates under an angle of 14.8° within the sample. Although an angular range is covered by the in-situ lens, we will limit our discussion to this central angle. Projecting the initial direction of the electron's spin onto the optical path of an emitted photon, we find that the measured polarization p_{circ} is lower than the actual polarization p^*_{circ} of the photon emitted in the bulk by $cos(14.8°) = 0.97$. In addition, refraction itself leads to a decrease of polarization. According to the Fresnel equation, this factor amounts to 0.93, yielding a total correction factor of 0.90. This connects the actual degree of circular polarization to the measured one like $p^*_{circ} = 1.11 \times p_{circ}$. Assuming a maximum degree of polarization of 50 %, this gives a maximum measurable value of 45 %.

By means of the selection rules, we can infer the maximum initial spin polarization of the recombining electron. For degenerate heavy and light hole bands, a 100 % spin polarized electron population in the conduction band causes the emission of 50 % circularly polarized light. This factor-of-two relation together with the correction factor due to refraction allows us to calculate the electron's spin polarization p like

$$p = 2 \times 1.11 \times p_{circ} = 2.22 \times p_{circ} \tag{2.7}$$

In the case of non-degenerate heavy and light hole bands (as discussed above), this factor-of-two relation does not hold. Accordingly, the factor between the electron's spin polarization and the degree of circular polarization is smaller than two. It may be close to one, like, e.g., for quantum dots, where heavy and light holes are also non-degenerate. An exact number, however, cannot be established based on the present data.

2.7.3 Molecular Fluorescence

Molecules can be excited by the absorption of electromagnetic radiation of suitable energy. After a certain time, they will return to their ground state, releasing the excess energy. This can happen via radiative or non-radiative processes, and the transition can be direct or via intermediate states. The emission of a photon during direct de-excitation is called fluorescence. By analyzing the luminescence emitted from molecules, conclusions about the energetic positions of their ground and excited states (and associated vibrational levels) can be drawn.

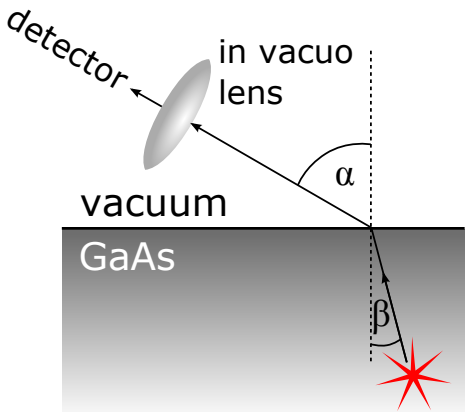

Figure 2.9: Schematic of the geometry in the light emission process. Light is generated in the bulk (marked by a red star), propagates towards the surface and is refracted there. In order to leave the crystal under an angle of $\alpha = 60°$ (toward the detector), it must approach the surface under an angle of $\beta = 14.8°$. Total reflection occurs for angles $\beta > 15.9°$.

As STL evolved into a standard method, the desire to investigate molecular fluorescence in conjunction with spatial and electronic proprties of single molecules arose. Such a technique promised, e.g., to put chemical sensitivity in STM within reach. Furthermore, it would allow for the combination of advanced spectroscopical methods for the investigation of fluorescence with the high spatial resolution of STM.

The first STL experiments were made with fullerenes on metal surfaces [96, 123]. The data clearly showed that the presence of molecules even in the first monolayer has an impact on the quantum yield and on the spectral distribution of the emitted luminescence. It was tentatively claimed that this was due to the excitation of molecules by inelastically tunneling electrons and subsequent fluorescent relaxation, which was further supported by experiments on porphyrine molecules [124]. This claim, however, remained controversial, as it was generally assumed that molecules in close proximity to metallic interfaces are subject to strong non-radiative damping and fluorescence is thus quenched [125, 126]. This was also corroborated by experiments that compared luminescence from monolayers with emission from higher coverages [127–130] or from decoupled molecules [131, 132]. There, it was found that fluorescence was indeed quenched for molecules that were in direct contact with a metallic substrate, whereas luminescence from molecules in the second layer was detected.

Another explanation for the observed changes in spectra and intensity was then given by Hoffmann et al [133]. They presented evidence that the changes are merely due to a modification of the tip-sample distance when scanning over a molecule. This affects the rates for inelastic tunneling as well as the TIP to photon conversion. In other words, the molecule acts as a passive spacer that alters the TIP, thereby affecting the emitted plasmonic luminescence.

Considering that a vast majority of experiments find no or strongly suppressed fluorescence from molecules in close proximity to metals, it appears reasonable that

investigations of molecular fluorescence now generally rely on decoupling mechanisms. This is achieved via stacking of molecular layers [127, 128, 134, 135], insulating layers like NaCL or CuN [131, 132, 136, 137], or self-decoupling molecules that are detached from the surface owing to their geometry [138]. It is, however, also possible to use non-metallic substrates like HOPG [139] or GaAs [140]. For those substrates, plasmonic resonances in the relevant spectral range are too faint to affect the lifetimes of molecular excited states [141–143]. Thereby, quenching of fluorescence is greatly reduced.

3 Experimental Setup

All experiments described in this thesis were performed in a home-built STM operated under ultrahigh vacuum (UHV) conditions and at liquid helium temperatures, called LT-STM below. In this chapter, I will briefly explain the setup and the operation of the STM and the light analysis installation. For a comprehensive description the reader is referred to [144] for the vacuum setup, [145] for the STM and [146] for the optical detection setup. Extensive information on the general operation of an STM can be found in textbooks [67, 147–150].

3.1 UHV system

The vacuum setup consists of a preparation chamber with adjacent load lock, and an STM chamber. For tip and sample preparation, a 4-axis manipulator with a filament for electron bombardment heating, a sputter gun, an electron beam evaporator and an evaporation station for the deposition of molecules and metals are provided. Temperature control is achieved via monitoring with a pyrometer, and evaporation rates can be determined with a quartz balance.

Tips and samples can be moved between the chambers without breaking the vacuum via wobble stick manipulators and linear transfer arms. Usually, base pressures of 10^{-10} mbar and $< 10^{-11}$ mbar are obtained for preparation and STM chamber, respectively.

In measurement operation, the whole setup is lifted with a pressured air damping system. Additionally, a smaller damping stage decouples the helium dewar from the rest of the frame, improving vibration resistance of the STM.

All control signals are generated in a separate room and led into the chamber via shielded cables. Measurement signals are transferred back the same way. Tunneling current and voltage are transmitted differentially via two leads to reduce the effect of electrical pick-up noise.

3.2 Low-Temperature STM

The STM is based on a design by Robert Gaisch [151, 152] with modifications by Jörg Kliewer [144]. It is mounted inside a copper cylinder which is firmly screwed to a liquid helium dewar. A second cooling stage consists of a liquid nitrogen dewar surrounding the helium tank. Radiation shields in both stages minimize thermal input. Usually, temperatures of 5.2 K are achieved. When the optical setup is used (see section 3.3), temperatures rise to $\approx$ 5.6 K. The standing times are between 6 and 7 hours for the liquid nitrogen dewar and 24 to 26 hours for the liquid helium dewar.

The samples are mounted on stainless steel holders. These are clamped to a slider which is used for coarse movement. Cooling samples from room temperature to 5 K usually takes less than one hour. For coarse approach and sample positioning, the slider can be moved in two directions by a slip-stick drive. The tip is inserted into a horizontally mounted segmented piezo tube, enabling three dimensional movement for z positioning and scanning.

For a detailed description of the STM the reader is referred to the references given above.

3.3 Light-Detection Setup

The optical setup consist of an in-vacuo and different interchangeable ex-vacuo parts. They are interconnected in a light-tight fashion to rule out disturbances from ambient light.

Inside the chamber, a tube oriented at $\approx 30°$ towards the surface normal of the sample can be led through holes in the radiation shields up to the STM (see figure 3.1 for a detail of the tube in the measurement position). A plano-convex lens (focal length 27 mm, diameter 25.4 mm) is mounted in the front of the tube. Optical adjustment is achieved by mechanically tilting the tube and traversing it linearly, so that the tip apex can be positioned in the focal point of the lens. That way, the light emitted in the tunneling junction is converted into a parallel beam of light, and then led out of vacuum through a fused silica viewport. The tube that is inserted into the cryogenic environment is cooled via a copper braid connected to the liquid nitrogen dewar in order to prevent excessive heat introduction to the STM stage. Further details on the light collection setup can be found in reference [153].

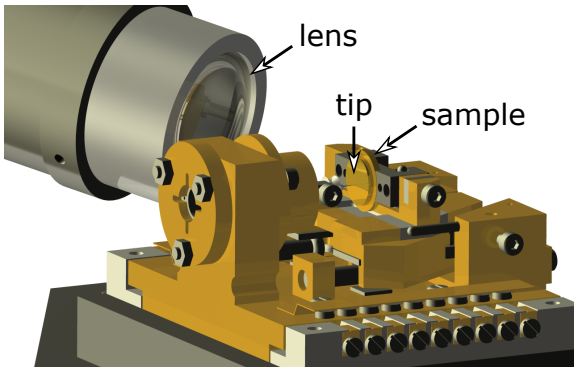

Figure 3.1: In-vacuo lens in front of STM

Outside the chamber, the light can be processed in different ways. For adjustment purposes, a beam reducer with an iris diaphragm is attached, enabling visual examination of the lens position. As the focal length of the in-vacuo lens is wavelength dependent, a final re-adjustment to maximum signal strength must be executed with a suitable detector attached.

All light data presented in this thesis are corrected for dark counts and, in the case of the CCD camera, for the readout background signal. Dark signals are measured by retracting the tip from the sample but leaving the rest of the setup unchanged.

3.3.1 Spectral Analysis Setup

For spectral analysis, the parallel beam of light is focused onto a fiber and then guided through a grating spectrometer (Andor Shamrock SR-303i) onto a thermoelectrically cooled CCD camera (Andor iDus DU420A-BU). Usually, an integration time over several minutes is chosen to maximize signal strength, and the data is read out in full binning mode in order to minimize readout noise. Spectra, unless otherwise noted, are not corrected for CCD or spectrometer sensitivity. Typical sensitivities are listed in section 3.3.3.

3.3.2 Polarization Analysis Setup

For polarization analysis, the beam of light is firstly reduced in diameter and then led through a liquid crystal quarter wave plate setup (Thorlabs) that can be switched electrically from minus to plus one quarter wave retardation (see figure 3.2). Thereby, left (right) circularly polarized light is converted to horizontally[1] (vertically) linearly polarized light, and vice versa. Subsequently, it passes a horizontally aligned linear

[1]The term “horizontal” is chosen to facilitate understanding of the underlying principles. The absolute direction of polarization is of course irrelevant, only the relative orientation of the quarter wave plate towards the linear polarizer matters. A horizontal orientation of the linear polarizer is thus only one possible arrangement of this setup.

polarizer and is eventually focused onto a thermoelectrically cooled avalanche photo diode module (Perkin Elmer SPCM-AQRH-16) with a dark count rate of $\approx 18\ \mathrm{s}^{-1}$. By measuring the two intensities $I(\sigma_+)$ and $I(\sigma_-)$ for left and right circularly polarized light, respectively, the degree of circular polarization P_{circ} can be calculated as

$$P_{circ} = \frac{I(\sigma_+) - I(\sigma_-)}{I(\sigma_+) + I(\sigma_-)} \tag{3.1}$$

In order to minimize the influence of long-term fluctuations (e.g. intensity variations due to thermal drift of the optical setup), the polarization is measured by repeatedly recording $I(\sigma_+)$ and $I(\sigma_-)$, respectively, for short time periods. This is done multiple times and an average polarization value is determined. Intensities are calculated by adding the individual intensities for right and left circularly polarized light.

For polarization analysis of spectral sub domains, short, long or band pass filters are introduced into the optical path.

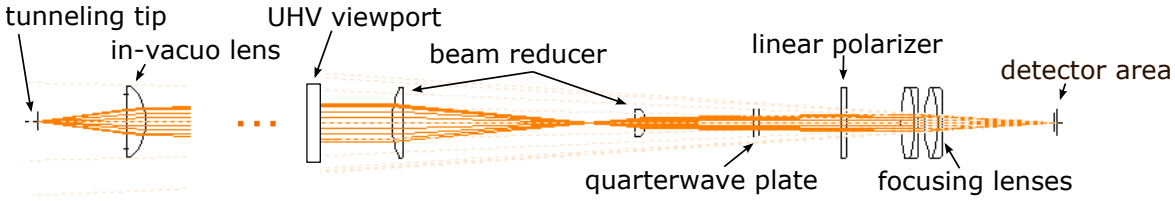

FIGURE 3.2: Optical path for polarization analysis. Adapted from [154].

3.3.3 Typical Detection Efficiencies

Photons emanating from radiative recombination in GaAs experience absorption, refraction and reflectance. These processes define the spatial distribution of intensity in the far field. The detection setup is able to collect light from a limited solid angle of roughly 0.45 sr. In the following, the best-case ratio of detected to created photons is estimated for spectroscopic and polarization measurements.

Due to the high refractive index of GaAs of 3.66 at 850 nm, photons approaching the crystal-vacuum interface at angles greater than 15.9° toward the surface normal undergo total internal reflection. Assuming isotropic propagation within the crystal, this results in an emission probability of only 1.9 %. Taking into account the anisotropic radiation pattern outside the crystal according to Lambert's law and the geometry of the light detection setup, it is found that roughly 15 % of the emitted light reach the in-vacuo lens. This yields an overall rate of ≈ 0.3 % of the created photons that enter the detection setup. As the first lens is not anti-reflection coated, losses in the range of 10 % are expected there. All ex-situ lenses are coated and exhibit reflective losses well below 1 %. Depending on the further detection path, different losses and detection efficiencies must be considered.

For spectroscopic measurements, losses at the interfaces and within the fiber waveguide amount to ≈ 25 %[2]. Fig. 3.3 shows efficiencies for the CCD as well as for two different gratings of the spectrometer (500 nm and 800 nm blaze angle, respectively). Most measurements in this thesis were conducted with the 500 nm blaze grating. At 850 nm, a combined detection efficiency of CCD and grating of roughly 13 % is found. A typical efficiency curve for the avalanche photo diode is also displayed as a dashed line. At 850 nm, it exhibits a detection efficiency of ≈ 50 %[3]. All data shown here are typical detection efficiencies specified by the manufacturers.

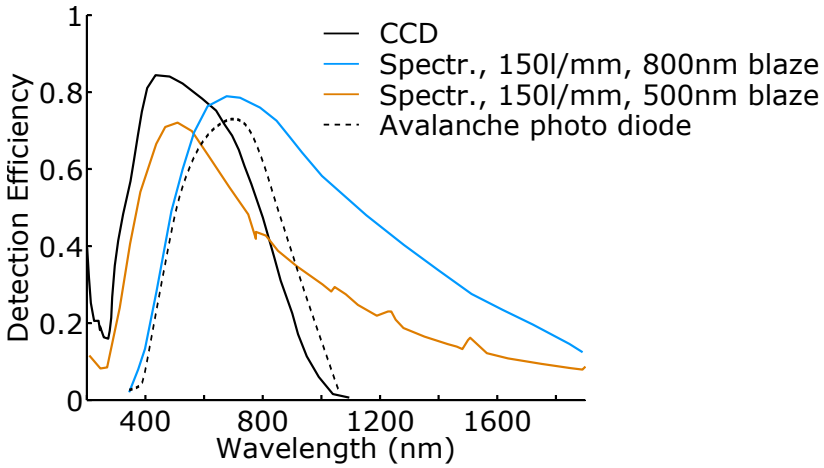

Figure 3.3: Typical detection efficiencies of the CCD camera, two gratings and the avalanche photo diode.

Combining all aforementioned effects, for wavelengths around 850 nm a ratio of detected to created photons of 3×10^{-4} to 1×10^{-3} for the spectroscopic and the polarization setup, respectively, are found. These numbers hold for ideal optical conditions and do not take misalignment and aberrations into account.

[2]Fiber bundle bought from LOT-QuantumDesign GmbH, type LOLLB552, 1m length. Transmittance estimated from manufacturer's data on a 2m fiber bundle.

[3]Typical data provided by manufacturers (Spectrometer and CCD camera: Oxford Instruments plc, formerly Andor Technology plc; Avalanche photodiode: Perkin Elmer, Inc.)

4

Plasmon-induced fluorescence and electroluminescence from porphine molecules

The results presented in this chapter were published in the journal *Applied Physics Letters* [140] in 2012. The co-authors were Natalia L. Schneider[1], Markus Gruyters[1] and Richard Berndt[1]. As the above journal uses a two-column layout, an adaption to a one-column style was made without changing the content.

4.1 Introduction

Surface plasmon polaritons of the tip of a scanning tunneling microscope are used to induce fluorescence from (5,10,15,20)-tetraphenyl-21H,23H-porphine (TPP) molecules on GaAs(110) surfaces at very low coverages. Fluorescence spectra exhibiting vibrationally resolved Q-band transitions show that the luminescence is of molecular origin. The emission is not directly induced by the tunneling current. Rather, radiationless energy transfer from plasmon modes of the tip leads to molecular excitation.

[1]Institut für Experimentelle und Angewandte Physik, Christian-Albrechts-Universität zu Kiel, D-24098 Kiel, Germany

With ongoing miniaturization the need for new ways of ultra-fast data transmission on nanoscopic length scales is unbroken. Plasmonics have been suggested as a promising solution for this challenge [155]. An important aspect of this field is to understand the interaction of photons with nanometer-sized structures. Light emission from the scanning tunneling microscope (STM) [90] enables highly localized plasmon generation along with real-space imaging and electronic characterisation on the atomic scale and appears to be particularly suitable for investigations at the ultimate size limit.

Molecular fluorescence from the STM has been excited by directly injecting electrons to molecules. As significant fluorescence quenching occurs when molecules are adsorbed directly at a metal surface [156–158], these investigation focussed on molecules which were decoupled from the metal substrate by insulator layers or molecular multilayers [128, 129, 131, 132, 137].

Excitation and fluorescence of molecules or semiconductors may also be achieved via plasmons [134, 159–162]. Such an effect has been invoked to interpret STM induced light emission from porphyrine multilayers on graphite [139]. Tips that gave rise to strong light emission from Ag surfaces, so-called "bright tips", also lead to fluorescence from multilayers. However, in the experiments of Ref. 139 direct excitation of molecules with the tunneling current occurs. While plasmons may be involved in exciting molecules an alternative mechanism is that these tips act as antennas to efficiently couple out light from molecules which are excited by the current.

Here we report on STM-induced luminescence (STL) investigated from single TPP molecules adsorbed on a semiconductor surface. The experimental results remove the ambiguity of the role of plasmons of the tip. To avoid direct excitation with the tunneling current the STM tip was placed at nm distances from the closest molecule. Nevertheless, light emission was detected and spectral resolution as well as an analysis of the degree of circular polarization have been achieved. Highly Zn-doped GaAs was selected as a substrate for its efficient electron-photon conversion [14]. Also, no surface plasmon excitations are expected to occur in the relevant wavelength range [141–143], leaving the tunneling tip as the only plasmon source. Owing to its band gap of $\approx 1.5\,\mathrm{eV}$ the luminescence from GaAs is spectrally separated from the known radiative transitions of TPP, which occur at higher energies [48, 129–131, 163]. Ag tips were used for their unique plasmonic properties. The data reveal that plasmons of the tip may be used to excite molecular fluorescence as well as band-edge luminescence of GaAs over nm distances.

4.2 Experimental Setup

The experiments were conducted in a home-made STM operating in ultra-high vacuum (UHV) at a temperature of 5.8 K. Clean and atomically flat GaAs(110) was prepared in UHV at room temperature by cleaving a small piece ($3 \times 8\,\mathrm{mm}^2$, thickness $300\,\mu\mathrm{m}$) from a highly p-doped GaAs(100) single crystal wafer. TPP coverages of a few percent

of a monolayer were deposited by sublimation onto the cold sample. Tips were electrochemically etched from polycrystalline Ag wires (0.25 mm diameter) and cleaned in vacuo by heating and subsequent Argon ion sputtering. Bias voltages always refer to the sample side of the tunneling junction.

Emitted light was collected with a plano-convex lens and directed via a UHV viewport to a grating spectrometer with a thermoelectrically cooled CCD camera optimized for ultra-low light intensities. Alternatively, the degree of circular polarization was measured by successively passing the light through a quarter-wave plate and a linear polarizer onto a high-sensitivity avalanche photodiode. Background signals have been subtracted from all light data shown here. Spectra are not corrected for the detection efficiency of the setup.

4.3 Results and Discussion

Figure 4.1 (a) shows two TPP molecules on atomically flat GaAs. Their characteristic four-lobe pattern is clearly observed, as well as the atomic rows of the (110) surface. Spectra of the light emission were recorded at positive and negative sample voltage, respectively, at a lateral distance of $\approx 4.5\,\mathrm{nm}$ from the closest TPP molecule (Fig. 4.1 (b)). Several prominent structures can be identified, including peaks at 611, 676 and 843 nm, as well as several shoulders. Except for the peak at 843 nm, all features are more distinctive at negative sample bias.

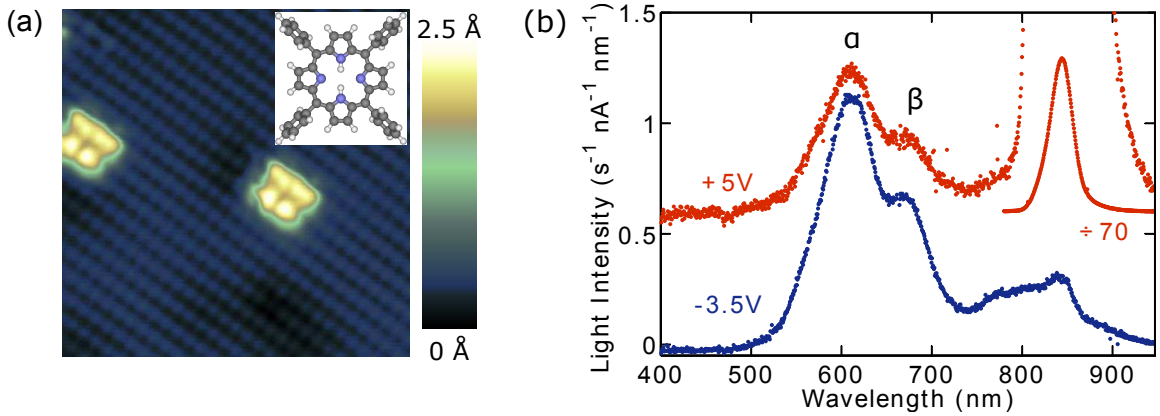

Figure 4.1: (a) Constant current image of single TPP molecules on atomically flat GaAs. Image size: $(11\,\mathrm{nm})^2$. Inset: Structure of TPP. (b) Light emission spectra recorded with a Ag tip at sample voltages $V = 5\,\mathrm{V}$ and $V = -3.5\,\mathrm{V}$ at a tunneling current $I = 5\,\mathrm{nA}$. For clarity, the spectra have been vertically offset by $0.6\,\mathrm{s^{-1}\,nA^{-1}\,nm^{-1}}$.

At positive sample bias, the main spectral feature is a peak at 843 nm due to electroluminescence of GaAs [19, 164]. Electrons from the tip are injected into the conduction band, where they relax, and eventually recombine with holes of the p-doped material. At negative bias, the quantum efficiency for electroluminescence of

p-doped GaAs is orders of magnitude lower and usually not observed at the voltages typically used in STM [165, 166].

In the present data, however, band edge luminescence occurs at negative bias as well, albeit reduced in intensity by a factor of ≈ 50. Given the low quantum efficiency for luminescence upon hole injection into p-type GaAs we suggest an alternative mechanism. Tunneling electrons may excite plasmon resonances of the Ag tip which couple to the sample and thus excite luminescence. Using W instead of Ag as tip material, no luminescence was detected as expected owing to the widely different dielectric function of W[2]. Further evidence for the involvement of plasmons is presented below.

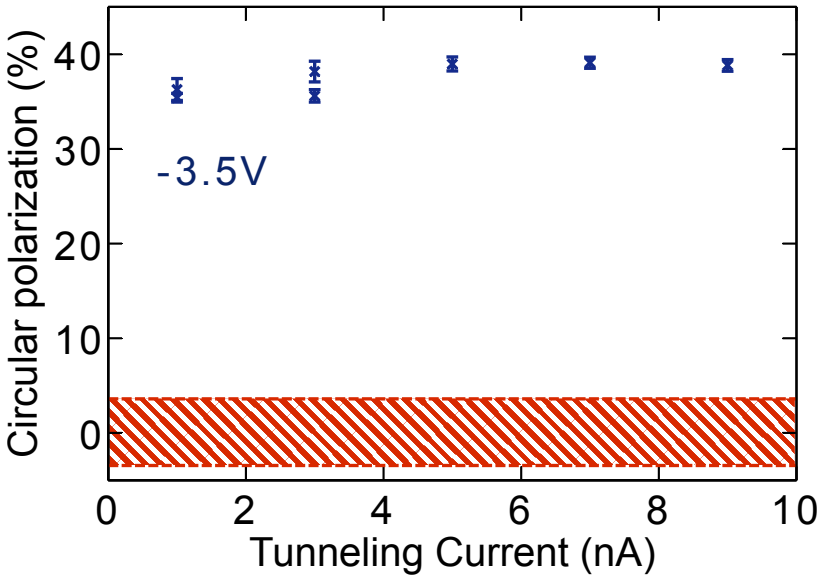

FIGURE 4.2: Degree of circular polarization vs. tunneling current at a bias voltage of -3.5 V and positive voltages between +2 and +5 V. At positive bias, polarizations between -3.2 ± 0.4 % and 3.6 ± 0.2 % were measured as indicated by a hatched stripe.

In addition to the spectral analysis, the circular polarization of the recombination luminescence was determined. For electron injection (positive sample bias), degrees of polarization in the low percent range ($1 - 4$ %) were found. Slight variations were observed with different tips, but the tunneling currents or voltages used (1 to 5 nA, -3.5 to 5 V) had a negligible effect on the polarization. At negative bias, in contrast, the measured circular polarization was of the order of 10 up to 40 % (Fig. 4.2). These high degrees of polarization cannot be attributed to a spin polarized tunneling current, which is difficult to imagine with Ag tips anyways [19]. However, comparable polarizations have been measured and calculated for plasmonic light emission from moderately asymmetric tips [167–169]. We therefore suggest that the band edge luminescence is due to the recombination of excitons created by radiationless energy transfer from

[2]The detection limit of the experiment corresponded to 2 % of the intensity observed with Ag tips.

plasmon polaritons of the tip to the GaAs substrate. To estimate the efficiency of the energy transfer we calculated the radiation pattern of a dipole at nm proximity to a semiconducting halfspace following Ref. 170. We find that well above 90 % of the energy of the electromagnetic field are located in the substrate. This implies that most of the energy is transferred radiationlessly. Our data also indicate that much of the polarization is conserved. As a result, a significant spin imbalance may occur in the GaAs conduction band.

Another conceivable scenario leading to circular polarization of the emitted light might be to assume a specific tip geometry that effectively acts as a polarization filter. This is inconsistent, however, with the experimental results. Operating the same tip alternatingly at positive and negative bias polarities we observed the drastic differences of the degree of polarization reported above.

Hence, we conclude that at positive bias injected electrons induce most of the luminescence, whereas radiationless energy transfer from the tip surface plasmon is relevant at negative bias. Evanescent waves from the tip propagate into the sample and generate spin polarized electron hole pairs, which then recombine radiatively.

Interestingly, the luminescence spectra (Fig. 4.1 (b) reveal additional peaks at 611 and 676 nm, as well as several shoulders which cannot be related to GaAs luminescence. Their positions do not vary significantly with bias. The wavelengths of the shoulder at 576 nm as well as the peaks at 611 nm and 676 nm match intramolecular Q-band transitions of TPP for different vibrational levels [139, 171, 172]. Their energies are approximately equidistant with a mean spacing of 0.16 eV, in accordance with observations in Ref. 128. We therefore conclude that these peaks are due to molecular fluorescence.

An unambiguous assignment of the observed peaks α and β to specific molecular vibronic transitions is not possible, because the influence of the substrate is unknown. Two assignments appear reasonable. Following, *e. g.* , Refs. [130] and [172], the peak denoted α matches the $Q_x(1,0)$ transition, whereas β corresponds to the $Q_x(0,0)$ transition. In photoluminescence experiments, in addition the $Q_x(0,1)$ mode is usually observed. In STL experiments, however, the modes of the exciting plasmon influence the emission strongly [139, 173]. This may lead to the extinction of spectral features, thus explaining the absence of this peak in our data. Another conceivable assignment is that α and β correspond to the $Q_x(0,0)$ and $Q_x(0,1)$ transitions, respectively, as reported for free base porphine in [48].

As the spectra were measured at lateral distances of several nanometers from TPP molecules the fluorescence cannot be induced by direct injection of electrons from the tip into the lowest unoccupied molecular orbital (LUMO). Neither is it induced by hot holes propagating at the surface. In such a scenario electroluminescence from GaAs would be expected to be much more intense than the molecular fluorescence, in contrast to the experimental data [174].

Having excluded the injection of holes as a direct cause for the detected fluorescence, the most natural explanation is again the radiationless transfer of plasmonic energy to the molecule and the semiconductor and the excitation of electron-hole-pairs thereby.

Measurements of the degree of circular polarization of the molecular fluorescence corroborate this interpretation. High degrees of polarization up to ≈ 30 %, which vary significantly from tip to tip, were found, just as for pristine GaAs. The polarization of the light at positive bias, which consists primarily of band edge luminescence, was also analyzed and found to be in the range of a few percent. Therefore polarization filtering by the tip can safely be ruled out.

4.4 Conclusion

In summary, band edge electroluminescence as well as molecular fluorescence have been observed from TPP molecules on GaAs(110) using an STM with Ag tips. No current flow through TPP molecules is required to induce molecular fluorescence. The experimental data are consistent with nonradiative energy transfer from plasmons of the Ag tip to the crystal and the molecules, which leads to the generation of electron-hole pairs and corresponding luminescence. The polarization of the tip plasmon is at least partially conserved in the process. It will be interesting to use Ag tips to further explore their electromagnetic coupling to molecules and the localized generation of spin polarized charge carriers.

We thank Susanne Menzel, Rudolf Rösch, and Peter Unger from the University of Ulm for generously providing custom-made GaAs wafers and Christoph Lienau, University of Oldenburg as well as Moritz Sokolowski, University of Bonn, for discussions. This work was funded by the Deutsche Forschungsgemeinschaft, project GR 1409/5-1.

5

Surface plasmon induced luminescence from GaAs

This chapter constitutes the basis for a publication in the journal *Applied Physics Letters* in 2015 [175]. Coauthors are Markus Gruyters[1] and Richard Berndt[1].

5.1 Introduction

Spintronics denotes the concept of the exploitation of the electron spin as a means of storing and transmitting information, and its integration into modern electronic devices. Over the course of the past decades, it has become a topic of intense research, as it promises to increase device density and efficiency and to allow for new functionalities. With the discovery of the giant magnetoresistance effect (GMR) in 1988 by Peter Grünberg and Albert Fert and co-workers [176, 177], a multitude of new experiments and device designs emerged. By applying the concept of GMR to read heads of hard discs [178–182], data storage densities were increased by two orders of magnitude, rendering the miniaturization of many devices possible.

In order to integrate future spintronic devices into electronic circuits, efficient spin transfer across device interfaces is crucial. Therefore, a fundamental understanding of the underlying principles and the physical limits is needed. Although most of today's prototypic spintronic devices rely on semiconductor heterostructures [117, 183–189], a much simpler model system can give insight into the fundamental process of spin transfer. Spin injection into a single crystal GaAs wafer with a remanently magnetized

[1]Institut für Experimentelle und Angewandte Physik, Christian-Albrechts-Universität zu Kiel, D-24098 Kiel, Germany

STM tip represents one of the most basic spintronic systems conceivable [19, 20]. The superior lateral resolution of STM allows for a local injection of very low currents and excellent verification of surface quality, while the electroluminescence (EL) of GaAs serves as a spin-indicator [18, 21, 22] (see chapter 2.1.3). The tunneling barrier is expected to reduce spin flip processes that occur due to conductance mismatch, increasing spin injection efficiencies by roughly one order of magnitude [190–192].

Another approach in GaAs-based spintronics experiments is based on the optical pumping effect, creating a spin polarized electron population within a semiconductor by the absorption of circularly polarized light (so-called spin pumping). As this circumvents the injection of spin polarized electrons, the characteristics in such experiments can deviate from spintronic systems within ordinary electronic circuits. Spin injection and spin pumping, however, can also occur simultaneously. When metal-semiconductor structures are used for spin-injection, collective electron oscillations at the metallic surface – so-called surface plasmons – arise. Those plasmons exhibit evanescent waves that couple to the adjacent semiconductor where they can excite electron hole pairs [140, 170]. This process can be considered a near-field analog to optical pumping. It can also be spin-selective, thus representing an additional source for spin-polarized electrons in spin injection systems [23, 24, 140]. To date, this process has not attracted much attention in scanning tunneling luminescence (STL) experiments.

We have studied the spin transfer efficiency from a remanently magnetized ferromagnet to p-type GaAs across a tunneling barrier. We find a strong energy dependence of the circular polarization of the recombination luminescence and unexpectedly high maximum values exceeding 50 %. We propose a model of a two-parts light generation process with a plasmon induced excitation dominating at low energies, and a superimposed electron injection luminescence becoming dominant at energies of $\approx$ 100 meV above the conduction band gap edge. The degree of circular polarization above 50 %, seemingly contradictory to the well-known selection rules, is tentatively explained in terms of a dopant induced broadening of the acceptor level and its merging with the valence band.

5.2 Experimental Details

All measurements presented in this chapter were carried out in a home-built low temperature STM operated at 6 K [144] (see section 3.2). The samples were cleaved at room temperature within the vacuum chamber (base pressure better than 1x10^{-9} mbar) from highly Zn-doped (2.1 x 10^{18} to 1.3 x 10^{19} cm^{-3}) 360 μm thick GaAs(100) single crystal wafers. They were then transferred in vacuo to the STM and cooled down. Samples with micrometer-sized atomically flat regions were routinely obtained.

Tips were prepared by electrochemical etching of a 99.9+ % pure polycrystalline Ni wire in a 10 % HCl aqueous solution. They were cleaned in vacuo either by heating through electron bombardment only or by heating and subsequent Argon ion sputtering, yielding comparable tip qualities. Before being mounted in the STM, the tips were

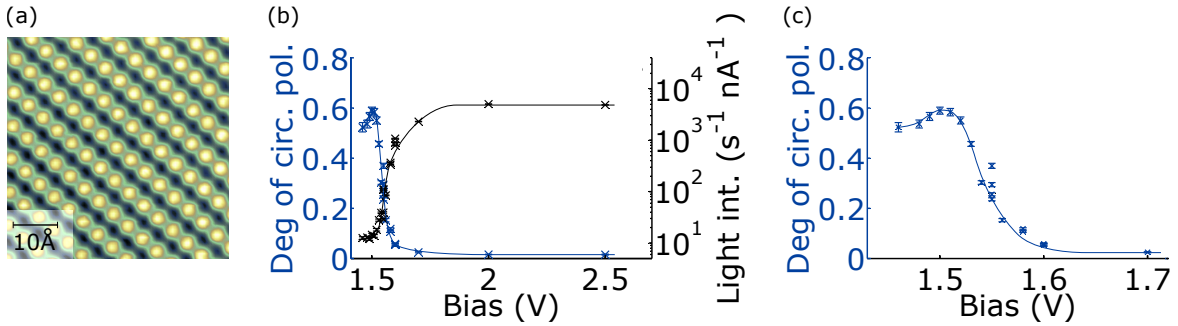

FIGURE 5.1: (a) Topograph of the GaAs(110) surface ($V_T = -2.8$ V, $I_T = 30$ pA). (b) Degree of circular polarization and measured light intensity vs. sample bias. (c) Detail of (b) with only the polarization displayed. Solid lines are guides to the eye.

magnetized with a permanent magnet (samarium cobalt (SmCo), 250 mT). Due to the large shape anisotropy in Ni, the magnetization direction of the tip is preferentially oriented along its long axis [193].

A detailed description of the light collection and processing setup is found in chapter 3.3. To facilitate readability, circular polarization values are always given as absolute values, even though both signs (for left and right circularly polarized light, respectively) have been observed. In principle, by reversing the tip's magnetization, the sign of the polarization should also invert [19]. In practice, however, the exact direction of magnetization of the apex atoms of the tip are hard to control. They depend strongly on the actual geometry of the apex [194–198] and possible contaminants [19] on its surface. In our setup, a remagnetization of the tip always involves a retraction from the sample and a subsequent reapproach. Hereby, in most cases the microscopic shape of the tip will be altered, as assessed by a change in imaging quality. This constraint could be overcome with a setup that allows for remagnetization of the tip by means of an electromagnetic coil while staying close to tunneling contact [19].

5.3 Results and Discussion

Figure 5.1 (a) shows a topograph of the clean GaAs(110) surface. The atomic corrugation is clearly visible. Subimage (b) shows typical polarization and light intensity data retrieved for a range of sample biases. Starting from a voltage of 1.46 V, intensities rise quickly and reach a plateau at $\approx$ 1.7 V. The simultaneously measured circular polarization is 52.3±1.9 % at 1.46 V, rises to 58.9±1.4 % at 1.5 V, and then drops steeply to 5.4±0.6 % at 1.6 V and below for higher biases (see image 5.1 (c) for an enlarged detail). For different tips, the run of the polarization curve is always similar. Their maximum polarizations, however, vary strongly. Values between $\approx$ 10 % and $\approx$ 70 % have been observed. In the following section, several interesting characteristics of the data presented here will be addressed.

5.3.1 Deviation from the selection rules

According to the selection rules and interband transition probabilities for recombination luminescence in GaAs, the maximum attainable circular polarization amounts to 50 %, corresponding to a complete spin polarization of the electrons in the conduction band (see section 2.1.3). In the present experiment, we find values that are significantly higher, rendering an interpretation based on the established transition probabilities impossible.

For quantum well structures and strained surfaces, similar observations have been made [114–117]. They are explained in terms of a lifting of the degeneracy of the heavy and light hole bands, leading to a recombination with light holes only. This changes the recombination probabilities drastically. In the extreme case, a one-to-one relation between electron spin polarization and degree of circular polarization of the recombination luminescence results.

In our case, neither quantum well structures nor strain[2] are present. It is known, however, that the band structure of a semiconductor is altered for heavy doping densities. For p-type GaAs, the acceptor level is supposed to broaden to an acceptor band that eventually merges with the valence band [118–122]. In this case, a narrowing of the band gap is observed.

Evidence for the applicability of the band merging hypothesis comes from scanning tunneling luminescence (STL) spectra taken on the bare GaAs(110) surface. Figure 5.2 shows 4 spectra taken at various biases. Except for a scaling factor due to different total intensities, they are superimposable within experimental uncertainty, as expected for electroluminescence. The main peak is found at ≈ 1.46 eV (corresponding to a wavelength of 849 nm). Interpolating the low-energy edge linearly, the onset of luminescence is found to be at ≈ 1.44 eV. Using the empirical calculation method for 6 K and a doping density of $N_A = 10^{19}/cm^3$ from reference [202], the band gap energy is expected to be ≈ 1.50 eV. Our spectral data, however, show a significantly narrowed band gap of only ≈ 1.44 eV to 1.46 eV. This is consistent with the intensity data shown before, where the onset of luminescence has been observed at 1.46 V. These values are in reasonable agreement with observations from photoluminescence measurements as well as calculations for highly Zn doped GaAs, where reductions of the band gap width of 50 to 80 meV were found [203–205].

Following reference [119], the band merging takes place predominantly between the acceptor and heavy hole states. The degeneracy of the heavy and light hole bands is thus lifted, making the selection rules inapplicable (see schematic in figure 5.3). Considering the high doping density of our samples, it appears likely that this effect is responsible for our observation of degrees of circular polarization above 50 %. As the actual relation between electronic polarization and circular polarization of the

[2]It is known that the topmost layers of the GaAs(110) surface are indeed strained [1, 199]. However, as the mean free path in GaAs at low temperatures is long (several tens to hundreds of nanometers [200, 201]), recombination takes place deep in the bulk material and is not expected to be affected by strain in the surface layers.

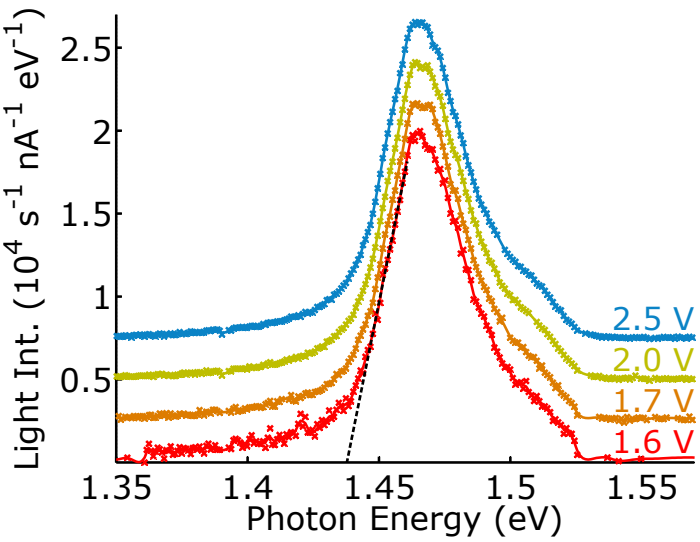

Figure 5.2: Scanning tunneling luminescence spectra taken at different biases and at a current of 500 pA. The spectra at 1.6 V, 1.7 V and 2.0 V have been scaled by factors of 5.7, 2.5 and 1.03 respectively to match the maximum of the spectrum for 2.5 V. Curves have been offset vertically for clarity. The dashed line designates the tangent to the low energy edge of the luminescence peak.

recombination luminescence remains unknown, in the following a one-to-one relation is assumed. Therefore, in the discussion below, no distinction between circular and electronic polarization is made. However, one must bear in mind that the degree of circular polarization yields but a lower limit for the spin polarization of the electrons in the conduction band.

A small additional correction results from the geometry of our setup. As the light is detected under an angle of 60° toward the surface normal, refraction has to be taken into account. Light leaving the crystal at 60° has a propagation angle of 14.8° within the sample. Projected onto the tip's axis, this corresponds to a lowering of the measured polarization by a factor of 1.03. According to the Fresnel equations, refraction itself leads to a decrease of circular polarization by a factor of 1.07 upon emission from the surface, giving a total relation of electronic to measured polarization of 1.10. The absolute maximum of the measured circular polarization in our setup is hence 91 %.

For the sake of completeness it should be noted that the presence of the metallic tunneling tip can also influence the polarization of the emitted light. It was found that the p-polarized part of light emitted close to the tunneling junction is enhanced while the s-polarized part is attenuated [206]. This effect is relevant for light that is created in a shallow region below the surface ($\leq$ 20 nm), and depends on the tip shape as well as on the lateral distance between the tip and the point where the light leaves the surface. In p-GaAs at low temperatures, however, the electron mean free path is expected to be larger than 20 nm [200, 201], rendering an influence of the tip unlikely.

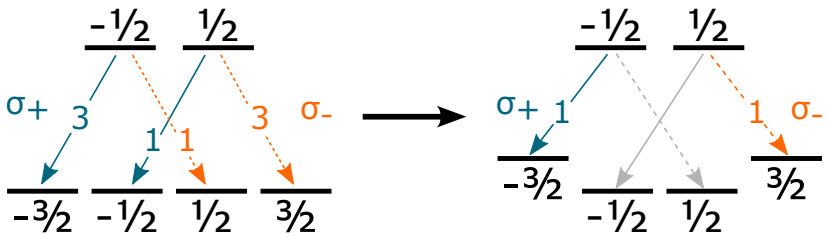

FIGURE 5.3: Schematic of the effect of the lifting of the degeneracy of heavy and light hole bands. The heavy hole band moves up in energy due to a merging with the acceptor band. This leaves holes in the heavy hole band as the dominant recombination partners for electrons from the valence band. Blue solid and orange dashed lines designate transitions leading to the emission of σ_+ and σ_- light, respectively. Numbers denote relative transition probabilities. Not to scale. Adapted from [17].

Furthermore, the enhancement of p- as compared to s-polarized light without any polarization dependent retardance would merely transform circularly polarized light into elliptically polarized light, to the same extent for both handednesses. Considering the detection setup with an intermediate conversion into linearly polarized light this would merely lead to an overall decrease in light intensity, but would not cause a change in the ratio of right to left circularly polarized light.

5.3.2 Steep drop-off of the measured polarization

A striking observation in the polarization versus bias data is the steep drop-off from values around 60 % to a very low value of the order of some percent within an energy range of $\approx$ 100 meV. This means that only at low tunneling bias a significant fraction of the recombining electrons are spin polarized. In principle, there are two possible causes for this observation. Either electrons injected at low energies have a significantly higher spin-polarization at the time of recombination (due to enhanced initial polarization or due to a higher degree of conservation of polarization), or at low bias, light generation processes that are otherwise masked by a high signal become visible. These two possibilities will be evaluated below.

Energy-dependent spin injection and relaxation

It is generally assumed that the spin polarization of electrons crossing a tunneling barrier is largely preserved [207–211]. Once the electrons enter the sample, scattering leads to a decrease of the spin polarization. In GaAs, the spin relaxation mechanisms to be considered are the Elliot-Yafet (EY) process, the D'yakonov-Perel' (DP) process and the Bir-Aronov-Pikus (BAP) process [212]. Which one dominates depends on doping type and concentration, temperature, band gap energy and kinetic energy of

the conduction band electrons. A discussion of the three competing processes is given in appendix B.

For the present case of highly p-doped GaAs and a working temperature of 6 K, we can assume that the BAP process is the primary spin relaxation mechanism for energies below $\approx$ 300 meV [212, 213]. It leads to spin relaxation times of the order of some 10 ns. These times are predicted to decrease with the square root of the kinetic energy of the electrons [213]. For energies below a certain, doping dependent critical energy of the order of 300 meV, however, this variation appears to be small [212–214]. From [213] we estimate that electrons with an excess energy of $\approx$ 100 meV exhibit relaxation times of roughly one order of magnitude less compared to electrons at the Fermi level. Including all aforementioned effects, spin relaxation times in the range of ns appear reasonable for our experimental conditions.

In order to predict the spin polarization at the time of recombination, one must compare the spin relaxation time to the energy relaxation time[3] of the electrons. According to theoretical results [201], energy relaxation times are in the range of a few hundred femtoseconds to picoseconds, much shorter than spin relaxation times. This suggests that the spin is largely preserved until the electrons are in energetic equilibrium. From then on until the time of recombination ($\approx$ 0.3 ns [215]), no further spin relaxation is expected and electrons with initially different kinetic energies should exhibit equal behavior. This is in agreement with photoluminescence and photoemission experiments [214, 216–218]. There, very little depolarization has been observed below $\approx$ 300 meV. This contradicts our measurements, where high degrees of polarization are observed only for very low kinetic energies up to some 10 meV. Therefore, a straightforward interpretation of our data on the basis of spin injection and subsequent relaxation is not feasible.

We must, however, note that the aforementioned experimentally determined time periods trace back to photoluminescence and photoemission measurements. There, excitation is accomplished via irradiation with circularly polarized light. Photons with energies high enough to lift electrons from the heavy and light hole bands as well as from the split-off band ($E > E_g + E_{SO}$ with $E_{SO} = 0.34\ eV$) can, as a matter of principle, not evoke a spin polarized electron population in the conduction band. This must lead to a strong drop of electron spin polarization for higher energies, rendering conclusions about spin relaxation at $E > E_g + E_{SO}$ difficult. For electron injection, this constraint is not applicable, allowing, in principle, for a spin polarized population of the conduction band up to high energies. This, however, is not observed in our experiment, nor in other STM studies [19, 20]. In contrary, we find much lower degrees of polarization already at low excess energies. It appears thus reasonable to assume that the processes known from photoluminescence cannot be readily applied to STM.

[3]Rather than the electron's free lifetime (the time between injection and recombination), its energy relaxation time is considered. This is because spin relaxation in GaAs is expected to happen only during energy relaxation and not while the electron thermalizes to the conduction band minimum from energies below the LO phonon energy [212–214]

To the best of our knowledge, it is unlikely that the specific setup in an STM will influence energy or spin relaxation times of electrons within the sample. However, there are significant differences between STM and photoluminescence experiments that most likely have an effect on the initial electronic conditions. They include vacuum tunneling from a ferromagnetic tip, the crossing of a second tunneling barrier formed by TIBB, and the fact that free carriers are injected at the Γ point, as opposed to the creation of an electron hole plasma within the sample in photoluminescence experiments.

One conceivable scenario is a highly energy-dependent spin polarization of the electrons upon injection. Magnetized ferromagnetic STM tips are routinely used for spin injection purposes [208, 219–225, and references therein]. Due to the large shape anisotropy of a thin nickel wire, the magnetization direction is oriented preferentially along the long axis of the tip [193]. Depending on the exact surface orientation at the apex, however, the electrons at the Fermi level are expected to exhibit different degrees of spin polarization, ranging from –100 % for Ni(110) to < 5 % for various other low-indexed surfaces [194–197]. This fact directly affects the maximum attainable circular polarization of the recombination luminescence. It has indeed been observed during our measurements that modifications of the tip shape can lead to a drastic change of the measured polarization, and even sign reversal.

Furthermore, for the Ni(100) and Ni(111) surfaces, photoelectron spectroscopy experiments have revealed a strong dependence of the spin polarization of the photoelectrons on the energy of the exciting photons [194]. Within a range of $\approx$ 100 meV, variations from $\approx$ –30 % to $\approx$ +30 % have been observed for Ni(100). Although the edge steepness of these data corresponds well with our observations, their absolute values are much lower. Moreover, they exhibit a distinct sign reversal, in opposition to the majority of our measurements.

As STM does not provide a means to determine the exact microscopic structure of the tip, it is impossible for us to link the tip's actual surface orientation to our polarization data. This condition could be partially circumvented in future experiments by employing tips made from single crystalline wire, as reported in reference [20]. For now, we can only note that the tip can have a strong influence both on the magnitude and on the energetic variation of the spin polarization of the injected electrons. However, it appears highly unlikely that a polycrystalline wire, as in our case, will in most cases yield the same apex surface orientation and thereby an always equally steep drop of polarization, as observed. Also, a much more constant value of the maximum polarization value would be expected in this case.

In conclusion, neither the established spin relaxation mechanisms nor the electronic structure of the tunneling tip are able to explain our polarization data satisfactorily. Based on the very low polarization measured at high bias, a low spin injection efficiency is assumed.

In the next section, a model to explain the high polarization measured at low bias will be proposed.

Superposition of plasmonic light generation and electron injection luminescence

As stated in the beginning, at low light intensities, other sources for luminescence could become relevant. In other words, the measured signal could consist of an energy dependent linear combination of two components. For different biases, one or the other would be decisive for the measured signal. Below, we will discuss how the specific geometry in an STM junction can cause spin-selective electron-hole-excitations that are able to dominate the signal at low bias.

It is known that the evanescent waves of surface plasmon polaritons on metallic STM tips or nanoparticles can couple to molecular excitations [130, 140, 159, 170, 226, 227] or to electron hole pairs in semiconductors [24, 140, 162, 228, 229]. When these pairs recombine radiatively, they emit light that cannot be distinguished spectrally from the electroluminescence stemming from injected electrons. This process is comparable to photoluminescence spectroscopy, with evanescent plasmons taking the role of impinging photons.

Nickel, as used in this experiment, has much higher plasmonic losses in the visible spectral range than noble metals, as can be deduced from its dielectric function [230, 231]. It has been reported that plasmonic light intensities from Fe and Ti (as examples of other non-noble metals) are lower by a factor of 20, compared to noble metal surfaces [232]. However, Ni can still be used as a material for plasmonic nanoantennas [233], showing that its plasmonic resonances are non-negligible. For high bias ($|V_T| > 3.5$ V), we have observed distinct plasmonic resonances from the surfaces of Ni as well as Ag tunneling tips. They have been identified by their spectral distribution with resonances above 1.6 eV, making them clearly distinguishable from the GaAs EL at 1.5 eV.

The lower curve in figure 5.4 shows such a spectrum for Ni taken at 3.5 V and 1 nA. A faint and broad signal is observed between 400 nm and 700 nm, while the onset of the electroluminescence is around 800 nm. A spectrum taken with a Ag tip at 5.0 V is shown in the same figure. The plasmonic resonance appears at higher wavelengths and is much narrower than for the Ni tip. However, spectra from many tips would need to be analyzed in order to identify material-dependent characteristics. The light intensities of the two curves are not comparable, as they were measured at different detector temperatures. Wavelength integrated measurements with an avalanche photodiode, however, generally showed that the intensity of the plasmonic luminescence from Ag tips is roughly one order of magnitude higher than for Ni, matching the observations for Fe and Ti mentioned above. As assessed from polarization measurements with a 750 nm short pass filter, this plasmonic luminescence exhibits strongly tip dependent degrees of circular polarization as high as ≈ 35 %. The ratio between the direct plasmonic intensities at high energy and the electroluminescence peak at ≈850 eV is roughly 25[4].

[4]To this end, the areas of the two peaks were calculated (from 490 nm to 780 nm and from 800 nm to 935 nm, respectively) and corrected for CCD and spectrometer sensitivity.

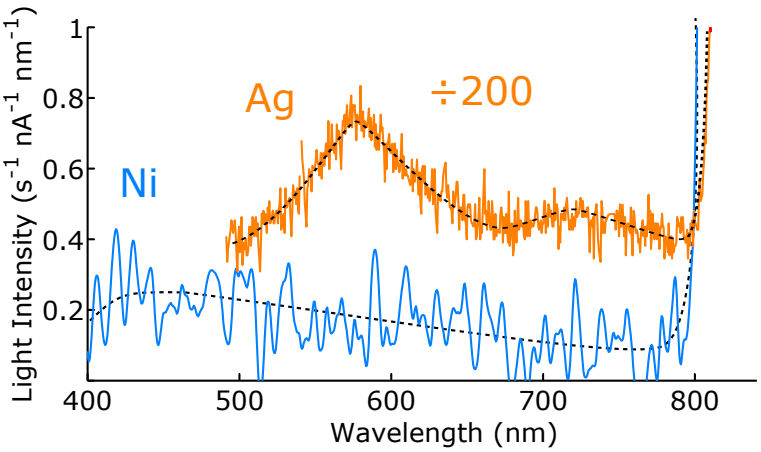

FIGURE 5.4: Light spectra taken on GaAs, vertically offset for clarity. Lower curve: Ni tip, $V_T = 3.5$ V. Upper curve: Ag tip, $V_T = 5.0$ V. Dashed lines serve as guides to the eye. Different noise levels are due to different detector temperatures.

Unfortunately, spectrally resolved measurements of the plasmonic luminescence at low bias are hard to obtain, due to inefficient outcoupling and high plasmonic transfer efficiency to the substrate ($\approx$ 90 % [170]) in an STM geometry. Fig. 5.5 shows three spectra taken at 1.52 V, 1.55 V and 1.7 V, respectively, with the intensity scaled such that maximum peak heights match (see caption for factors). The spectrum obtained at 1.7 V shows the expected electroluminescence peak, as also found in photoluminescence spectra [203]. The spectra at 1.52 V and 1.55 V, however, show intensity at lower energies that cannot be explained with interband recombination. As this observation is only made for some tips, we suppose a plasmonic origin of this luminescence that is detected only for tips with "suitable" directional characteristics.

It has been demonstrated both theoretically and experimentally that the plasmonic luminescence from slightly asymmetric STM tips can exhibit high degrees of circular polarization of up to 80 % [167, 168]. This polarization is also present in the near field and in evanescent waves and can be used for optical orientation in semiconductors [23, 24, 140]. In other words, tunneling tips with a suitable geometry are expected to excite spin-polarized electron-hole pairs in GaAs. When they recombine, the emitted electroluminescence – potentially being highly polarized – can be detected.

If for low sample bias this plasmon induced excitation process is, in terms of light generation, more efficient than injection, the electroluminescence arising from the plasmonic excitation can dominate the intensity as well as the polarization signals. Below, the plausibility of this hypothesis will be discussed.

Neglecting multi-electron effects (due to their drastically reduced efficiency), the energetic onset of the plasmon is identical to the tunneling bias V_T. If eV_T is larger than the band gap energy, a decaying plasmon can lift electrons in the sample to the conduction band, where they relax and eventually recombine. As discussed before,

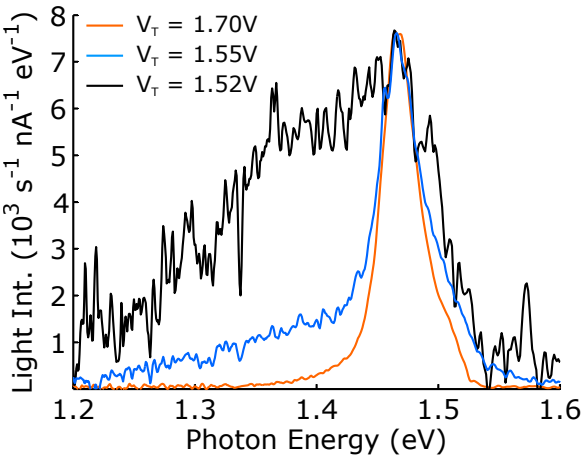

Figure 5.5: Light spectra recorded at different tunneling biases with a Ni tip on GaAs, scaled to matching peak positions (factors of 46.1 and 8.9 for 1.52 V and 1.55 V, respectively). At the low energy side of the spectra for 1.52 V and 1.55 V, a tail is observed.

in photoluminescence experiments no significant spin relaxation is expected for low energies, so that high degrees of circular polarization can be attained. The magnitude of the circular polarization associated with the plasmon depends on the exact geometry of the tip apex [167], which is compatible with our experimental observations of varying maximum polarizations.

Increasing V_T to $\approx$ 100 meV above the band gap energy is not expected to change the efficiency of the plasmonic coupling (or rather its total photon yield, normalized to the tunneling current) strongly. The spectral shape of the plasmonic luminescence will change with the result of slightly higher intensities, but this effect is rather small and linear in energy [102, 109].

On the contrary, close to the band gap the photon yield of the injection process is expected to increase strongly with V_T [47, 234, 235], quickly exceeding the plasmonic emission and therefore dominating the signal henceforward.

In order to evaluate the hypothesis of a plasmon induced process, a simple model is proposed. We assume that the total amount of light $I_{tot}(V_T)$ detected at a bias V_T consists of a share of plasmonically excited EL $I_p(V_T)$ depending linearly on the tunneling bias and exhibiting a constant polarization P_p, and an injection based share $I_{inj}(V_T)$ with constant polarization P_{inj}. We can then write the total circular polarization as an intensity-weighted sum of P_p and P_{inj}:

$$P_{tot}(V_T) = \frac{I_{tot}(V_T) - I_p(V_T)}{I_{tot}(V_T)} P_{inj} + \frac{I_p(V_T)}{I_{tot}(V_T)} P_p \tag{5.1}$$

where the first term represents the polarization contribution of the EL due to injection, and the second term refers to the polarization caused by recombination of plasmonically excited electron-hole pairs. $I_p(V_T) - I_{tot}(V_T)$ is the injection based intensity $I_{inj}(V_T)$.

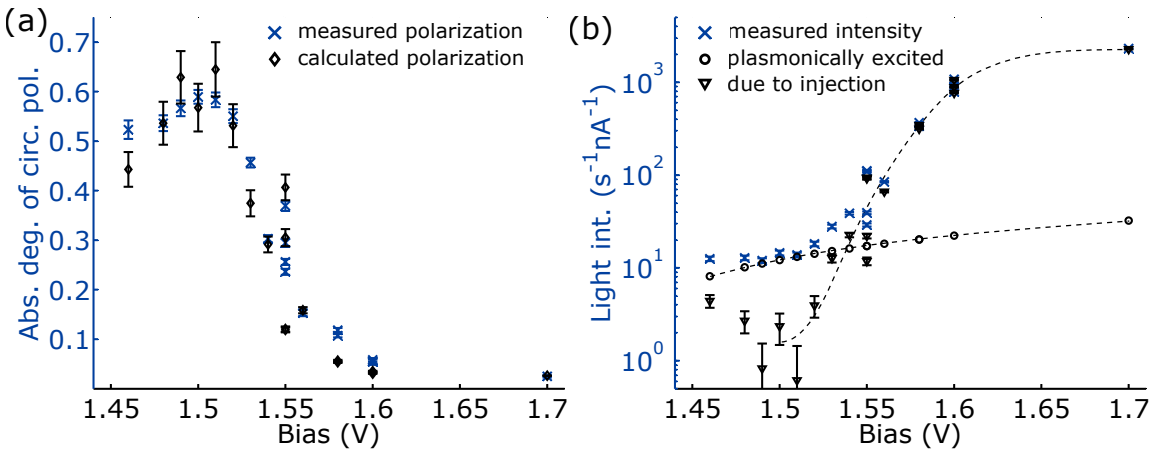

FIGURE 5.6: (a) Measured (×) and calculated (◇) values of polarization vs. bias. (b) Measured bias dependent light intensities (×) and calculated shares of plasmonically excited (○) and injection based (▽) intensities, respectively. Dashed lines serve as guides to the eye.

The parameters are extracted from the bias dependent intensity and polarization data shown in fig. 5.1(c) as follows: As injection based luminescence dominates at high bias, P_{inj} is taken as the mean measured polarization at V≥1.7 V: $P_{inj} \approx 1.7$ %.

$I_p(V_T)$ is approximated as linear in energy [102, 109]:

$$I_p(V_T) = \alpha(eV_T - E_{ph}) \tag{5.2}$$

with alpha being a fit parameter and E_{ph} being the energy of the detected photons. In principle, E_{ph} should be equal to the band gap energy of GaAs. However, as mentioned above, for some tips a low-energy contribution was observed in the spectra, possibly shifting this value toward lower energies. E_{ph} is thus considered another fit parameter that contains information about the strength of the low-energy contribution. In a more realistic approach, a range of photon energies instead of a single energy would have to be considered.

Inserting equation 5.2 into 5.1 yields

$$P_{tot}(V_T) = P_{inj} + (P_p - P_{inj})\frac{\alpha(eV_T - E_{ph})}{I_{tot}(V_T)} \tag{5.3}$$

The parameters α, E_{ph} and P_p are found via a least squares approach, where the match between measured and calculated degrees of circular polarization is optimized.

We find $\alpha = 101\ s^{-1}nA^{-1}eV^{-1}$ and $E_{ph} = 1.38{\pm}0.03$ eV, with a resulting plasmonic polarization $P_p = 61.1 \pm 0.8$ %. Uncertainty analysis was conducted on the basis of the standard deviations of the mean for polarization and intensity.

As mentioned above, E_{ph} contains information about the contribution of low-energy photons. In the model used here, it can be interpreted as an approximate mean energy of the detected photons. For purely interband related electroluminescence, a value around E_g would be expected. Here, however, we find a value that is 60 to 80 meV lower. This matches the observation of a low-energy tail in the spectra shown in figure 5.5.

The result of the calculation is plotted in fig. 5.6. In subimage (b), the total measured intensity (blue crosses) it displayed along the calculated plasmonic and injection based shares. Subimage (a) shows the polarizations, where blue crosses denote measured data, while the black diamonds are results of the calculation. The low degrees of polarization at high bias, the steep rise toward lower bias as well as the maximum at around 1.5 V are in very good agreement with the data.

To further corroborate the hypothesis of a plasmon induced process, measurements with non-ferromagnetic tips were conducted. The results are summarized in fig. 5.7. Subimage (a) shows light intensities measured for different tunneling biases. At positive bias, luminescence onsets around 1.5 eV are found, as expected for interband recombination. Light intensities rise monotonically for all tested tips, although total intensities vary significantly[5].

At negative bias, all tips exhibit an increase in luminescence yield toward higher negative bias. The rise is significantly weaker than for positive bias. This is due to the fundamentally different electroluminescence generation processes. At positive bias, injected electrons in the conduction band can readily recombine with the abundant holes in the valence band. On the contrary, at negative bias, electron hole pairs must first be generated by impact ionization through hot holes, causing a much lower photon yield [166, 236].

Fig. 5.7 (b) shows the degree of circular polarization of the electroluminescence, recorded simultaneously with the intensities. At positive bias, the curves for the nickel tips show a maximum around 1.5 eV and a steep falloff toward higher energies, as described above. For the specific W and Ag tips used here no maximum is found, which may simply be due to a lack of data in the extreme low bias regime. However, also the W and Ag tips show unexpectedly high polarizations of ≈10 to 35 % near the band edge and a steep falloff toward higher energies. This cannot be explained by spin injection, as these tips are non-ferromagnetic. Plasmonic excitation, on the contrary, is able to account for this effect, as the reasons given above for Ni are equally valid for W and Ag tips. Furthermore, the strong tip dependence of the maximum polarization can simply be explained in terms of tip-geometry dependent plasmonic resonances.

At negative bias, moderate to high degrees of circular polarization (≈ 20 to 60 %) are found as well. Again, this cannot be explained by spin polarized tunneling. For all tips, polarization values decrease toward higher negative bias, but at a much slower

[5]The most important factors influencing luminescence yield are the tip shape and the adjustment of the optical setup. At low bias, when plasmonic excitation dominates, the plasmonic efficiency of the material becomes relevant, too.

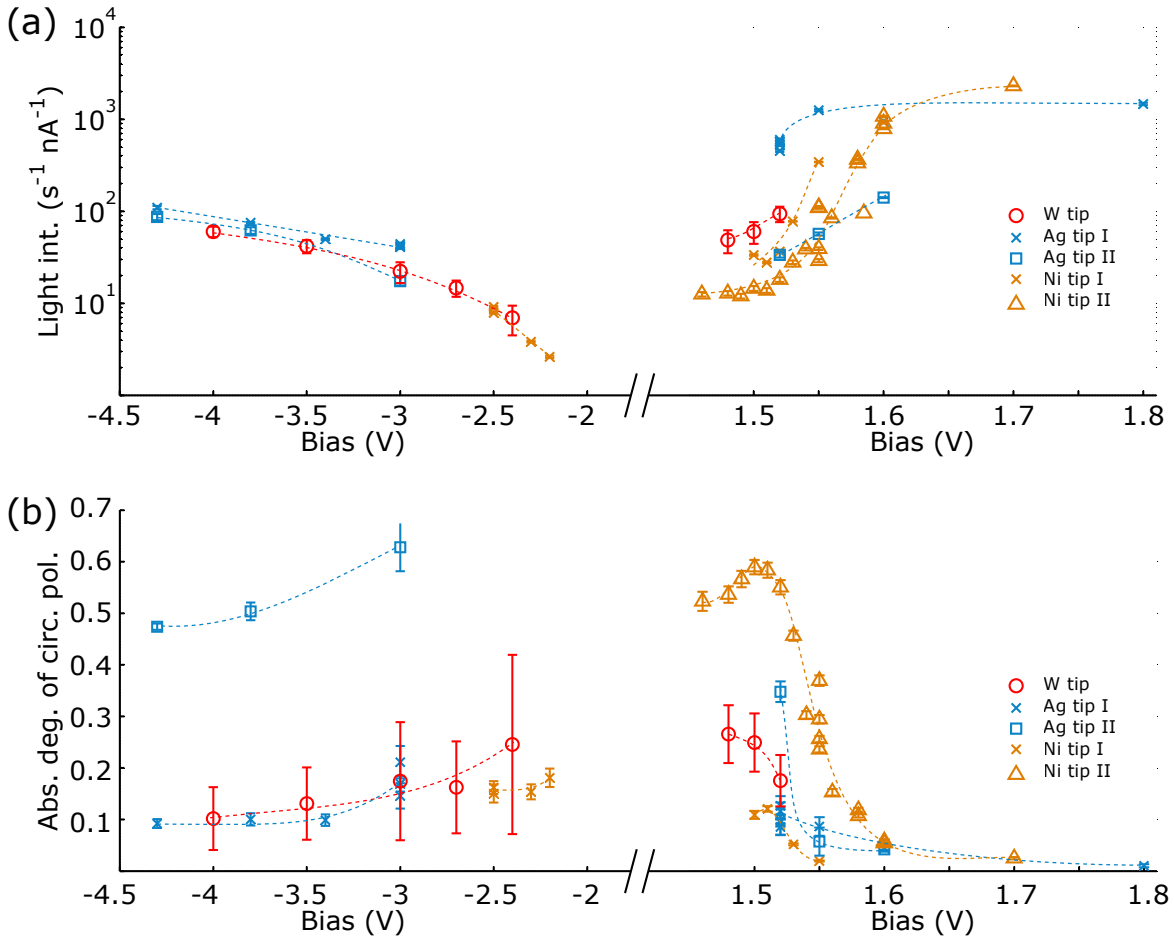

FIGURE 5.7: (a) Light intensity of the electroluminescence vs. bias for tungsten, silver and nickel tips, plotted separately for negative and positive bias with differently scaled voltage axes. For the Ni tip II, no negative bias data were measured. Between the two bias regimes, no light signal was obtained. Dashed lines serve as guides to the eye. (b) Same as (a) for circular polarization of the electroluminescence, measured simultaneously with light intensities.

rate than at positive bias. This indicates that at negative bias, the plasmonic share of the luminescence remains significant over a much wider range, in agreement with the slow increase in photon yield. This makes the evaluation by means of a simple model as described above unfeasible. The assumption of a constant polarization of the plasmonic luminescence over such wide bias range strongly contradicts experimental results, where variations of several ten percentage points have been observed for voltages differing by $\approx$ 1 V [167, 168].

The degree of circular polarization that we measured for biases above $\approx$ 1.6 V agrees reasonably well with other STM experiments [19, 20] and bulk spin LED measurements [184, 237, 238]. On the contrary, in photoluminescence experiments, much higher degrees of circular polarization of $>$ 20 % have been observed [213, 239, 240].

This indicates that the spin injection efficiency from a Ni tip to a GaAs sample is generally low in an STM setup.

5.4 Conclusion

We presented evidence that the recombination luminescence of p-GaAs can exhibit high degrees of circular polarization of > 50 % at low positive tunneling bias, and a steep drop-off to a few percent within ≈ 100 meV.

The apparent violation of the selection rules by circular polarizations above 50 % is explained in terms of a dopant induced broadening of the acceptor band and subsequent merging with the heavy hole valence band.

The established processes based on electron injection from a ferromagnetic tip and subsequent spin relaxation are unable to explain the run of our measured polarization data, specifically the steep drop-off, the strong variations of the maximum circular polarization and the distinct similarities between ferromagnetic and non-ferromagnetic tips.

As an explanation for the high degree of circular polarization measured at low bias, a plasmon induced light generation scheme, similar to photoluminescence, is proposed. We tentatively assign the high polarization to EL from the recombination of electron hole pairs excited by evanescent waves of a surface plasmon on the tip. A simple model is able to reproduce our data very well. Further evidence is provided through electroluminescence spectra and polarization measurements conducted at high bias, showing circularly polarized plasmonic components from Ni and Ag tips in the visible range. This plasmon-based model is applicable to any tip material exhibiting surface plasmon polaritons and can thus also explain the high circular polarizations observed for non-ferromagnetic tips.

The data for voltages above 1.6 V presented here differ strongly from photoluminescence experiments. They suggest that in STM, spin injection from a ferromagnetic tip to GaAs is highly inefficient, in agreement with observations in other STM experiments and bulk spin LEDs.

In conclusion, our data indicate that the tunneling current from ferromagnetic Ni tips is mainly unpolarized when it reaches the bulk semiconductor. However, evidence suggests that surface plasmons can be used to excite highly spin polarized electron populations in bulk GaAs. This mechanism might prove beneficial in efficiently linking plasmonic components and semiconductor-based spintronic devices. Furthermore, our observations show that it is crucial to pay attention to the obfuscating effect that surface plasmons can have in STM experiments.

We thank Susanne Menzel, Rudolf Rösch, and Peter Unger from the University of Ulm for generously providing us with custom-made GaAs wafers. Financial support by the DFG (grant No. GR 1409/5-1) is acknowledged.

6

Charging of single Phthalocyanine molecules on GaAs(110)

6.1 Introduction

Molecular electronics has been a topic of continuous and intense research, in particular since the first proposal of a molecular rectifier in 1974 [241]. With the invention of STM [58–60], a multitude of novel experimental possibilities emerged. Major efforts are currently being made to explore the principles that govern the interaction of individual molecules with conductive surfaces and their electronic characteristics thereon [55, 84, 242–245]. The findings from this constantly growing field of molecular electronics are hoped to pave the way towards the extensive integration of molecular functional blocks into ever new technological devices.

In this respect, the interface between the molecular building blocks and the conventional electronics basis is a matter of particular interest. On metals, the strong interaction between molecules and the metallic electron gas leads to a weakening or an alteration of single-molecule properties [246–248]. Furthermore, many molecules are mobile on metals at room temperature, effectively preventing their exploitation as individual functional parts. Thus, on the one hand, a strong coupling to the substrate is needed so as to prevent diffusion, while on the other hand the key electronic properties of the molecule must be preserved. The balancing of those two requirements continues to be a major challenge in molecular electronics.

One limitation of STM is the restriction to conductive surfaces. Purely metallic substrates, however, often exhibit the aforementioned drawbacks, namely high molecular mobility and strong electronic coupling. Therefore, thin insulating films of oxides

or salt have been used as cover layers [245, 246, 249–251]. These layers allow for tunneling while, at the same time, suppressing strong electronic coupling between the molecule and the electron gas in the metal. The same can be achieved with molecular multilayers [247]. This comes at the cost of single-molecule characteristics, though.

Another approach is the use of inorganic semiconductors. Despite the fact that they often exhibit dangling bonds which make them rather reactive, weak molecule-substrate interaction has been observed on a variety of passivated as well as unpassivated surfaces [248, 252–258]. This ususally causes the formation of ordered molecular structures with reconstructions governed by the orientation and termination of the substrate. As semiconducting materials present the basis for today's electronics devices, they can be considered as preferential candidates for the integration of novel single-molecule functionalities.

In this chapter, evidence is presented that single phthalocyanine molecules on unpassivated GaAs(110) largely preserve their electronic characteristics. The tip of an STM can be used to manipulate the band structure of the substrate, leading to a reversible modification of the charge state of the molecule.

6.2 Experimental Details

Measurements were conducted with the STM described in section 3.2 operated at a temperature of 5 K. Spectra as well as maps of differential conductance were obtained with the lock-in technique [80]. STM tips were prepared by electrochemical etching of a 99.9+ % pure polycristalline Ni wire or by incising and subsequently severing a 99.9 % pure polycrystalline Au wire. The tips were further prepared in vacuo by electron bombardment heating. Samples were cleaved in vacuo from a small piece of a 360 μm thick GaAs(100) wafer, exhibiting a clean (110) surface with large atomically flat areas.

75 % pure Silver Phthalocyanine (AgPC) molecules were purchased from the Sigma-Aldrich Corporation and further purified by cautious degassing in the vacuum chamber. They were then thermally evaporated onto the cold ($\approx$5 K) sample, resulting in the adsorption of individual molecules.

All topographs and maps of differential conductance were recorded in the constant current mode, while spectra of differential conductance were recorded at constant height.

6.3 Results and discussion

Figure 6.1 (a) shows a topograph of an individual AgPC molecule adsorbed on the GaAs(110) surface. Several submolecular features are clearly resolved, indicating a weak electronic coupling of the molecule to the substrate [246, 248, 257]. Molecules

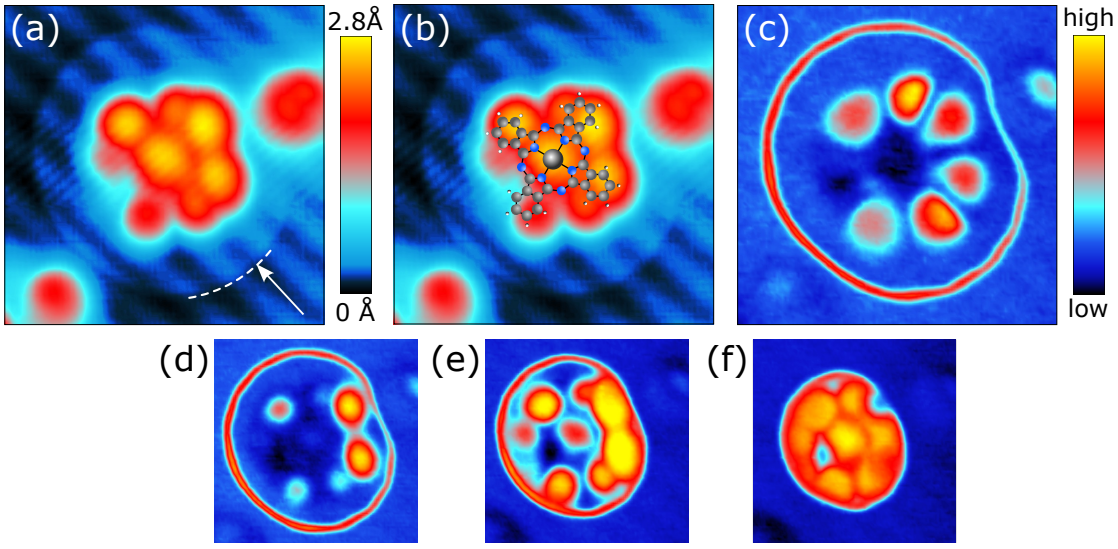

Figure 6.1: (a) Topograph of a single AgPC (cf. chapter 2.3) molecule on GaAs. Size 4 nm x 4 nm, recorded at V_T=–0.8 V and I_T=100 pA. A disc of increased apparent height around the molecule is visible (white arrow and dashed line mark edge). (b) Same as (a) with molecular structure overlaid. (c) Simultaneously recorded map of differential conductance, V_T=–0.8 V. The jump in apparent height in the topograph appears as a bright ring. (d) – (f) Maps of differential conductance of the same molecule at voltages V_T of –0.75 V, –0.6 V and –0.5 V, respectively. Image sizes are 3.5 nm x 3.5 nm.

adsorb at different angles with respect to the substrate and display a variety of appearances. Remarkably, one or several lobes of the molecules can exhibit a drastically reduced apparent height, thereby lowering the symmetry.

The molecule shown in fig. 6.1 (a), chosen as an example due to its clearly visible features, exhibits a substructure with a central protrusion and pairs of protrusions arranged around it. Within each pair, one protrusion appears slightly higher and larger than the other, possibly due to a slight tilting of the outer benzopyrrole groups. The twofold structure indicates a predominance of the a_{1u} molecular orbital in the tunneling current[86, 257, 258]. Secondly, the lower left lobe appears to exhibit only one of the two protrusions, and its height is decreased as compared to the other lobes. Very similar observations were made for H_2Pc and various metal phthalocyanines (Fe, Co, Ni, Cu) adsorbed on graphene on iridium (Ir) (111)[86]. It was explained in terms of a binding of a molecular lobe to the graphene layer, thereby causing this specific lobe to bend down toward the substrate. Based on the aforementioned considerations, the molecular orientation is assumed to be as shown by the overlay in fig. 6.1 (b). The size of the overlay is matched with the topographic scales.

Around the molecule, a circular disc of increased apparent height is visible (white arrow marks edge). Figure 6.1 (c) shows a simultaneously recorded map of differential conductance. Again, submolecular resolution is obtained, and a bright ring around the

molecule coincides with the jump in apparent height in the topograph. The diameter of the ring decreases with increasing bias voltage (see figure 6.1 (d) to (f)). It should be noted that only some molecules show such a ring-shaped feature [1].

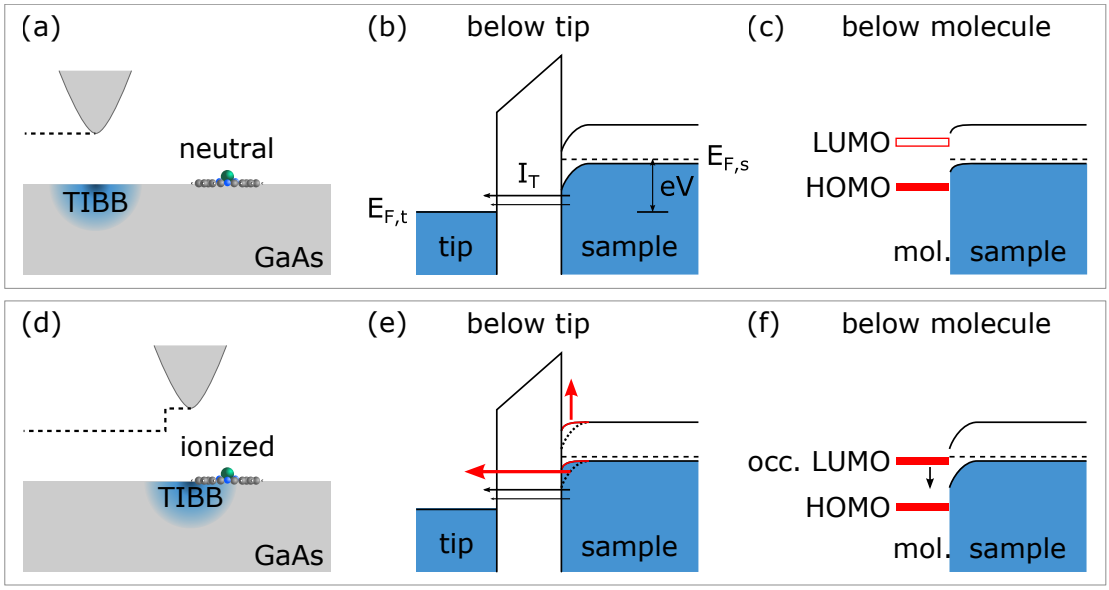

FIGURE 6.2: Schematic of the ionization process due to TIBB. Upper row: neutral molecule, bottom row: ionized molecule. Energy diagrams of the substrate below the tip ((b),(e)) and the molecule ((c),(f)) are shown side by side. For further explanations see text. Not to scale.

Similar ring-shaped features have been observed in STM experiments for individual impurities in semiconductors [259–262], single atoms in molecular monolayers [263, 264] or molecules on oxidized metal surfaces [265]. The circularly symmetrical jump in apparent height is commonly attributed to the ionization of a nanoscopic entity due to the proximity of the biased tunneling tip.

Below, the influence of tip induced band bending (TIBB) on the electronic landscape of a molecule on a semiconducting surface will be discussed. It will be explained under which conditions TIBB is strong enough to pull the lowest unoccupied molecular orbital (LUMO[2]) below the Fermi level and thereby ionize the molecule.

[1] No straightforward connection between molecular appearance and existence of this feature could be made. An in-depth analysis of the adsorption configurations and the electronic structure of AgPc on GaAs is beyond the scope of this thesis.

[2] The notation "LUMO" is used here in the sense of the lowest unoccupied molecular orbital in the AgPC-GaAs system. In the gas phase, for which the LUMO is usually defined, the electronic structure may deviate.

Figure 6.2 illustrates the ionization process for a molecule on a semiconductor at negative sample bias. A schematic of the geometry is shown next to energy diagrams of the tunneling junction and the sample, respectively. A given LUMO of the molecule is sketched in the band gap. In the upper row, the situation of the tip far away from the molecule is depicted. (a) Below the tip, an area of TIBB with a certain lateral extension is induced. In the mode of constant tunneling current I_T, the tip-sample distance will vary little when scanning the bare surface. (b) The bands below the tip are bent downwards (see section 2.1.2). (c) The molecular states as well as the bulk and surface bands of the sample at the molecule's position remain unaffected by the tip's electric field. A slight downward bending of the bands is expected at the surface (see fig. 6.3 for 0 V or references [78, 266, 267]). This slight bending is not strong enough to pull the LUMO below the Fermi level. The molecule thus remains neutral.

The bottom row of figure 6.2 shows a situation where the tip is close enough to the molecule to affect its charge state. (f) The presence of the tip causes a downward band bending, eventually pulling the LUMO below the Fermi level of the sample. This leaves the molecule charged. (e) The coulomb field of the charged molecule causes the downward band bending to diminish (indicated by the vertical red arrow, the dotted line shows the undisturbed bands). Thus, more states are accessible for tunneling, and the conductance (and thus I_T) increases (the horizontal red arrow indicates the additional tunneling current). (d) In order to keep the tunneling current constant, the tip is retracted from the sample. As the onset for the ionization depends only on the radial distance between tip and molecule, a circularly symmetrical disc of increased apparent height appears in the topograph[3].

From fig. 6.2 (c) and (f) it becomes clear that an ionizable molecular state must appear twice in dI/dV spectra: At positive bias, when the tip Fermi level aligns with the unoccupied state, and at negative bias, when electrons from the then-occupied state tunnel into the tip. The position of these two appearances of the same state depend crucially on the TIBB. As its calculation is afflicted with a relatively large uncertainty[4], no exact values can be predicted. An estimation of plausibility, however, is possible and is presented below.

Following references [43, 45], the TIBB for various tunneling biases is calculated. The parameters used are a tip-sample distance of 7 Å, sample and tip work functions of 4.7 eV and 5.3 eV, respectively, a band gap of 1.5 eV and an acceptor density of $5 \times 10^{18} cm^{-3}$. The result is shown in fig. 6.3. The TIBB varies monotonically with V_T. The flat band condition is met at ≈ 0.94 V. This point separates the curve into two regions of different and approximately linear slope.

As mentioned before, for the molecule to be ionized, one of its frontier orbital's states must cross the Fermi level. The energetic position of a state determines whether

[3]Depending on the exact geometry of the tip apex, the shape of the disc can deviate from a circular geometry [259].

[4]For an estimation of the error see appendix C

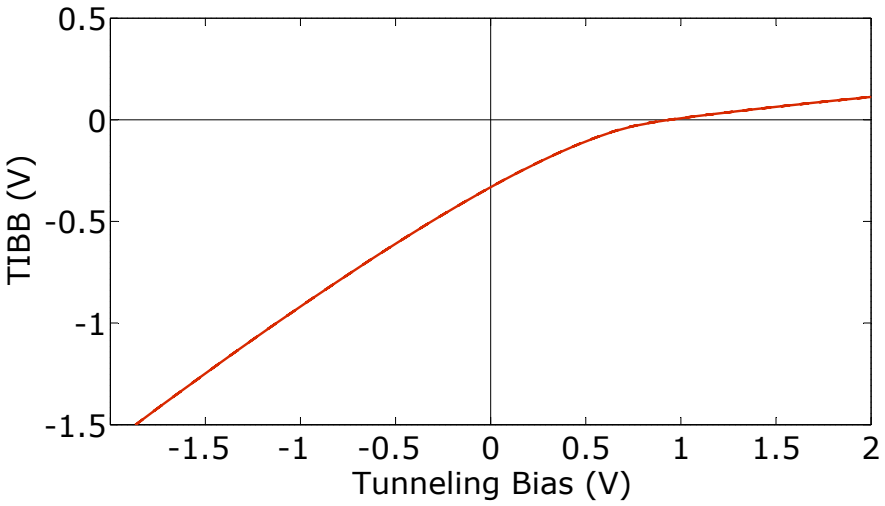

FIGURE 6.3: Calculation of TIBB as a function of tunneling bias. For parameters see text.

or not this will happen for a certain magnitude of TIBB. The TIBB increases with tunneling bias. Thus, even molecular states far from the band edges will eventually cross the Fermi level for sufficiently high bias. In reality, however, tunneling voltages are limited to ≈ -2 V $< V_T <$ ≈ 2 V, so as not to cause desorption or modification of the molecule. The TIBB for these limiting voltages determines the maximum energetic distance between Fermi level and molecular state where a tip induced ionization is still possible. Here, the TIBB is ≈ -1.6 V for $V_T = -2$ V and $\approx +0.1$ V for $V_T = +2$ V. This means that molecular states between -0.1 V and $+1.6$ V come into consideration for the ionization process.

Fig. 6.4 shows two dI/dV spectra. The lower one is measured on the bare substrate, the valence band edge is clearly visible. The upper one is measured on top of a single AgPc molecule that exhibits a ring-shaped feature. Several distinct peaks are observed: At 1.4 V, at 0.9 V (labeled I) and at –0.8 V (labeled II). For different tips the position of peak II varies by up to several hundred meV, most likely due to different TIBB which can shift features at negative bias drastically. Peak I exhibits a shoulder at each side and a region of negative differential conductance (NDC) to the right of it. The spectra were tip dependent insofar as NDC was not always observed, and the shoulders sometimes showed as actual peaks.

A DFT analysis using Gaussian 09 [268] (B3LYP functional [269–271], LanL2DZ [272–274] basis set) was conducted for AgPc in the gas phase for comparison with the energetic positions of the molecular orbitals. The calculation will be discussed in more detail in chapter 7. To summarize the results, two different conformations were found, an energetically favored planar one and a metastable shuttlecock one with the Ag atom protruding $\approx$ 1.0 Å from the plane defined by the four isoindole N atoms and that is higher in energy by $\approx$ 1.4 eV. The energetic positions of the orbitals vary for these

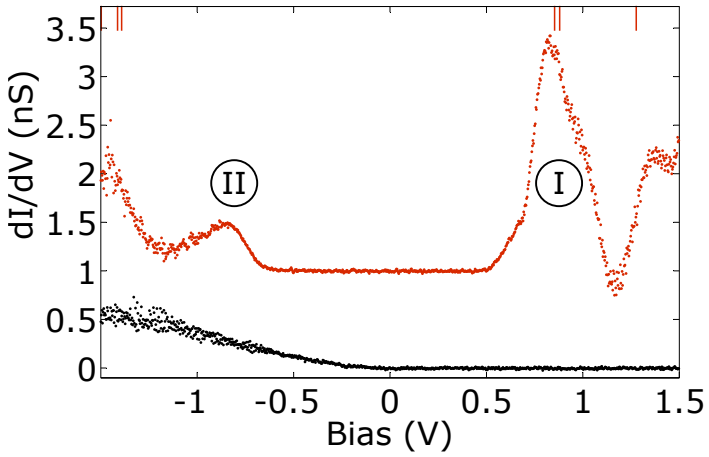

Figure 6.4: Constant height spectra of differential conductance. Upper curve: taken on AgPc with a ring feature. Lower curve: taken on bare substrate. Vertical red lines indicate positions of calculated molecular orbitals for planar AgPc. Spectra have been vertically offset for clarity.

two conformations. As no indication for a shuttlecock structure is found in the topographs and additionally the shuttlecock conformation is energetically unfavorable[5], AgPc is assumed to be present in its planar form. The position of peak I is taken as the LUMO of the molecule to fix the energy scale of the calculation. Due to band bending energetic positions must be regarded with care, especially at negative bias where TIBB shifts peaks toward higher negative energies. Furthermore, although molecule-substrate interaction is assumed to be weak, the proximity of a surface can influence the molecular conformation as well as the orbital energies (as seen, e.g., by the lack of a fourfold symmetry of AgPc in fig. 6.1). The vertical red lines at the top of fig. 6.4 indicate the calculated orbital energies for the planar conformation. They are found at 1.27 eV, 0.87 eV, 0.85 eV, –1.39 eV, –1.41 eV and –1.50 eV and agree well with the observed peaks, except for peak II which does not show up in the calculation. This is in accordance with the assumption that this peak originates from the charging of the molecule[6], as will be explained in the following

Peak I is located within the band gap and inside the range of -0.1 V to $+1.6$ V given above. It is therefore supposed that this state will have an "echo" on the negative bias side (called "charging peak" henceforward), as described above. Based on the calculated TIBB, the position of the charging peak can be estimated.

[5]This refers to the gas-phase molecules. For a complete evaluation of the AgPc-GaAs system, calculations including the surface are required.

[6]This implies that in the bias range below peak II the calculated orbital energies are not readily applicable, as the charging likely leads to a change in the energetic positions of the orbitals.

The procedure of mapping the occupied to the unoccupied variant of a molecular state will be elucidated below. Fig. 6.5 shows a schematic of the band structure for the cases of (a): tunneling into and (b): out of the same molecular state (depicted as open / filled red boxes), respectively. At positive bias $V = V_+$ (peak I), the band gap energy can be expressed through the TIBB at this voltage, the binding energy E_B of the molecule to the substrate with respect to the conduction band, the electron energy eV_+ and the acceptor level with respect to the valence band E_{Acc} (24 meV for Zn) like

$$E_g = |TIBB(V_+)| + E_B + eV_+ + E_{Acc} \tag{6.1}$$

with E_B the binding energy of the molecule to the substrate with respect to the conduction band, and E_{Acc} the acceptor level with respect to the valence band (24 meV for Zn). At negative bias $V = V_-$ (peak II), the band gap energy E_g can be written as

$$E_g = |TIBB(V_-)| + E_B + E_{Acc} \tag{6.2}$$

Equalizing equations 6.1 and 6.2 yields

$$|TIBB(V_+)| + eV_+ = |TIBB(V_-)| \tag{6.3}$$

The fact that the band bending is a strictly monotonic function of bias enables a one-to-one mapping of the voltages V_- and V_+ to their corresponding sides of equation 6.3. This results in a bidirectional transformation between V_- and V_+. The result is shown in fig. 6.6. The light blue lines labeled I and II denote the position of peaks I and II from fig. 6.4, respectively.

Although it must be pointed out that due to rather large and inevitable uncertainties in the calculation of the TIBB the present examination must be considered an estimation of plausibility only, the calculated mapping is in good agreement with the observed peak positions.

Within this context, it appears reasonable to assign the two observed peaks to one and the same molecular state. In the presence of TIBB, it is shifted across the Fermi level, leaving the molecule ionized. This leads to the emergence of a circular area of increased apparent height in the topograph.

It should be emphasized that while the LUMO state is crucial for the emergence of the circular feature, other states may determine the physical appearance of the molecules in the topographs. At the point of ionization (when LUMO and sample Fermi level align), the tip is still at a lateral distance from the molecule. Upon approaching, TIBB gets stronger and shifts the molecular states further down. Once the tip is directly above the molecule, other states may thus be closer to the sample Fermi level, therefore dominating tunneling current and thus the apparent molecular geometry[7].

[7]The LUMO could - in principle - be visualized in a map of differential conductance. As it resides within the band gap, however, it would have to be recorded at a voltage where GaAs is not conductive. In this case, a map of differential conductance is only feasible in the constant height mode, which was

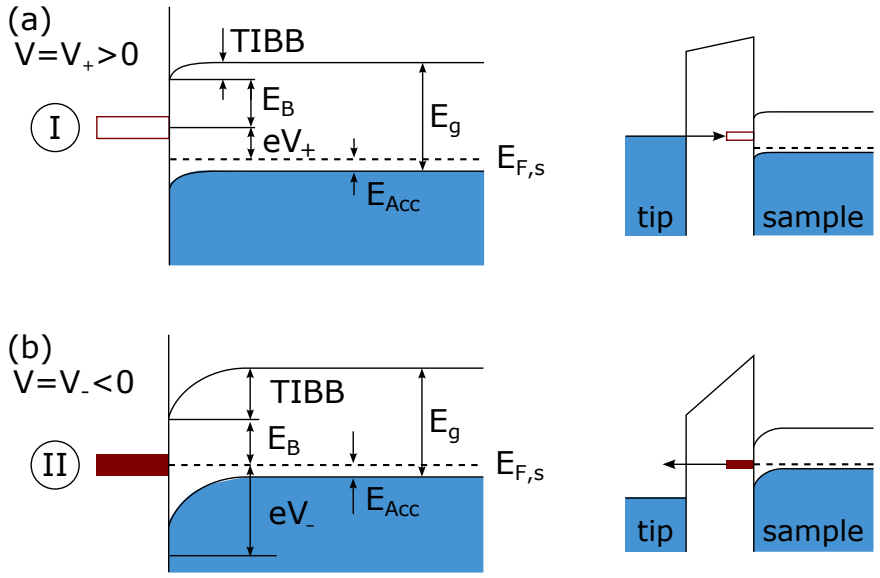

Figure 6.5: Schematic of the tunneling process (a) into the unoccupied molecular state and (b) out of the occupied molecular state. The left side shows a magnified view of the energetic landscape of the molecular LUMO at the band gap, while the right side shows the general tunneling conditions. TIBB denotes the tip induced band bending at the corresponding voltage, E_B is the energy of the state with respect to the conduction band minimum, E_{Acc} is the acceptor energy with respect to the valence band maximum, V_- and V_+ are the tunneling voltages at negative and positive bias, respectively, and E_g is the band gap energy.

6.4 Conclusion

Single AgPC molecules have been deposited on GaAs(110). At low temperatures, STM topographs show distinct submolecular features, indicating weak molecule-substrate interaction. Under suitable tunneling conditions, a circular disc of increased apparent height is found around the molecule and attributed to a tip-induced charging. Further evidence comes from STS, where in-gap peaks from AgPC states are found. A simple estimation predicts a charging peak of the LUMO on the occupied states side, in good agreement with the data. DFT calculations show no states at the position of the supposed charging peak, further corroborating this hypothesis

Similar observations for individual molecules have only been made on insulating layers on metals [265]. Here, no decoupling layer is needed. Instead, the preparation is rather straightforward. By charging the molecule, its conductance is tuned. This allows for the investigation of single-electron processes, and may prove useful in the design of future molecular functional building blocks.

beyond experimental means.

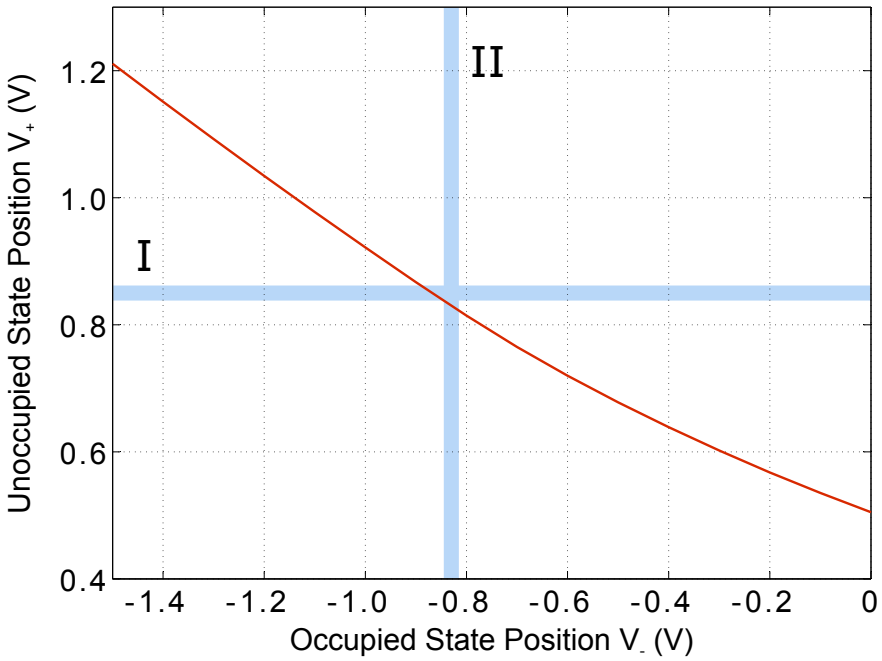

FIGURE 6.6: Calculated transformation between the occupied and the unoccupied variant of a molecular state. The light blue lines mark the position of states I and II from fig. 6.4.

7 Phthalocyanine islands on GaAs

7.1 Introduction

Phthalocyanines (Pc) have been a topic of intense research for almost a century. After being discovered rather accidentally their high chemical as well as thermal stability was quickly recognized [275]. In combination with the fact that they exhibited exceptionally intense colors that are tunable through the incorporated metal centers rapidly led to a patenting and a widespread use as dyes and pigments [53, 275, 276]. Due to the simpleness of their production and the similarity to the physiologically important porphyrins they are popular model systems for the study of charge transport in biological systems [275, 277].

Phthalocyanines were among the first reported organic semiconductors [278–280]. Their unique optical and electronic properties have rendered a utilization in a variety of organic electronic devices possible, including photodetectors, solar cells, field effect and thin film transistors, and light emitting diodes [30, 275, 281–283]. Thin phthalocyanine films are of particular interest as they allow for the development of flexible, low cost devices.

Many of the technologically relevant properties of phthalocyanines are based upon their π-conjugated nature. π-π interaction leads to ordered stacking and, under suitable environmental and growth conditions, ultimately to the formation of single crystals [54, 284–286]. It is known that conductivities in ordered films can be orders of magnitude higher than in polycrystalline films [29, 30, 287, 288].

It was found that copper Pc (CuPc) grown on Si at elevated temperatures exhibits very large mobilities of up to 0.02 $cm^2\ V^{-1}\ s^{-1}$ [28]. A clear relation between the grain sizes of the crystallites and the mobility was found. At optimum growth temperatures where highest mobilities were observed, crystallites exhibited lengths of $\approx$ 500 nm. At

lower temperatures they were smaller, while at higher temperatures gaps between the single crystallites became too large to yield high mobilities. Later, similar results were obtained for other metalated phthalocyanines [289, 290]. The finite crystallite sizes and the arbitrary growth directions of different crystallites appear to impose a limit on mobility. It is thus highly desirable to find ways to self-assemble molecules in regular patterns, in order to increase mobility while at the same time keeping production complexity low.

This chapter discusses the room temperature growth of iron (FePc) and silver phthalocyanines (AgPc) on GaAs(110). FePc was chosen because of its well-known growth and electronic structure. In order to elucidate the role of the central metal atom, AgPc was examined. Among the phthalocyanines these two exhibit a large degree of diversity: Firstly, FePc is planar while AgPc exhibits a non-planar conformation with the Ag atom protruding from the molecular plane, and secondly, FePc shows ferromagnetic interaction, while AgPc is non-magnetic. For both species, unidirectionally growing islands with very high long-range order are found, and their electronic as well as structural properties are examined. For AgPc, irreversible switching between different molecular appearances is observed and attributed to a transition between a non-planar and a planar conformation.

7.2 Experimental Details

Measurements were conducted with the STM described in section 3.2 operated at a temperature of 5 K. Spectra as well as maps of differential conductance were obtained with the lock-in technique [80]. STM tips were prepared by electrochemical etching of a 99.995 % pure polycrystalline Ag or a 99.9+ % pure Ni wire. The tips were further prepared in vacuo by electron bombardment heating. Samples were cleaved in vacuo from a small piece of a 360 μm thick GaAs(100) wafer, exhibiting a clean (110) surface with micrometer sized atomically flat areas.

75 % pure metalated phthalocyanine molecules with silver as well as iron centers were purchased from the Sigma-Aldrich Corporation and further purified by cautious degassing in the vacuum chamber. They were then thermally evaporated onto the sample held at room temperature using a button heater and a heating current between 1.40 A and 1.55 A.

All topographs and maps of differential conductance were taken in the constant current mode, while spectra of differential conductance were recorded at a constant tip-sample distance (constant height mode).

7.3 Results and Discussion

7.3.1 Growth and electronic structure of ultra-long FePc islands

The topograph in figure 7.1 (a) shows a section of a self-assembled FePc single-layer island on GaAs. It runs in a zigzag manner along the crystallographic [001] direction. The island exhibits two geometrically different domains, labeled A and B. They alternately run along either of two directions standing at an angle of 120°±2° toward each other (the two directions are oriented at 60°±1° toward $[1\bar{1}0]$ and will be referred to as "domain directions" of A and B, respectively, below). The domain boundaries run along the $[1\bar{1}0]$ direction. Neither of the two domains dominates over the other with respect to their frequency of occurrence or area. The two domains are mirror symmetrical with respect to $[1\bar{1}0]$, within experimental uncertainty.

FePc islands on GaAs(110) have a remarkable unidirectionality and length, often traversing the whole scan range (615 nm × 720 nm) linearly. This implies lengths of at least several hundred nanometers, most likely even in the micrometer range[1]. Intersecting step edges or adsorbates disrupt their growth[2], but at smooth and clean surfaces island ends are rarely observed. Due to the overall island growth along the [001] direction, neighboring islands do not intersect. At the coverages used here (≈ 10 % of a monolayer) distances of one hundred to several hundred nanometers between them were commonly observed. It should be noted that in preliminary measurements conducted at room temperature similar, but smaller and less regular islands were observed. These data are not shown here as they do not contribute additional information on island growth, except for the fact that islands are stable enough to be imaged at room temperature.

Subimage 7.1 (b) shows a magnified view of an island. A regular double-row pattern of circular protrusions is resolved. The two chains of protrusions within each double row exhibit slightly different apparent heights. The island width varies with the amount of molecules evaporated. Here, it is of the order of 10 nm (measured perpendicular to the direction of the chains of protrusions). It is virtually constant within one island.

The number of protrusions along the island width is always even. Along the growth direction, domains with even as well as odd numbers of protrusions are observed, suggesting that one bright and its neighboring faint protrusion represent exactly one molecule. This seemingly contradicts the molecular fourfold symmetry, where one would expect to image four protrusions arranged in a 2 by 2 manner per molecule for a flat-lying adsorption geometry. This is indeed the case for individual molecules

[1] Due to the exceedance of the scan range for many islands, their total lengths remain unknown. However, as island ends are rarely observed it is assumed that they are markedly longer than the maximum imaged length.

[2] The occasional step edges observed here are running at an angle of ≈ 7° with respect to the island direction, so that intersections are rare. On well cleaved samples, no step edges are observed over micrometer lengths.

on GaAs, where cloverleaf shaped structures are observed (see white dashed circles in fig. 7.1 (a)). Similar fourfold structures have been reported for phthalocyanines on other semiconductors [291–293] and on metal surfaces [294–297]. In contrast to the present work, on metals (e.g. on the (111) surfaces of copper and gold) at low coverages mostly single molecules are found, while in the high coverage regime self-assembled square-like patterns are observed.

These findings lead to the conclusion that here, the molecules do not lie flat on the surface but rather stand at an upright angle. In this way, the top orbitals appear in the topographs while the bottom ones are concealed underneath. Exemplary molecular units are indicated by the overlaid models in fig. 7.1 (b). The grouping of the protrusions to pairs and thus the assignment to molecular units is unambiguous due to geometric constraints at the island and domain boundaries. A possible molecular orientation along the island growth direction (i.e. along the chains of bright and faint protrusions, respectively) can be excluded because of the spacing of the protrusions of 5.6Å in this direction and thus a resulting 11.2Å space per molecular unit, being to small for the 13Å wide FePc to fit in. Furthermore, the same arrangement with one bright and one less bright protrusion per upright standing molecule was observed for metal phthalocyanines on Si [293, 298].

It is known that phthalocyanines – being conjugated molecules – show π-π stacking with their macrocycles facing each other [54, 284–286]. On metals and on most semiconductors this stacking usually happens in the out-of-plane direction due to strong electrostatic molecule-substrate interaction [54, 299]. On some semiconductors, however, growth modes with an in-plane orientation of the π orbitals – similar to the present case – have been observed [286, 293, 298, 300–305]. On the deactivated Si(111)-B $\sqrt{3} \times \sqrt{3}$ R30° surface, zinc Pc (ZnPc) and CuPc stand upright and form parallel islands that grow perpendicular to step edges [293, 298, 304, 305]. They strongly resemble the islands found in the present work, although their length is limited by the Si step edge distances. It was concluded that this growth mode is due to a weak molecule-substrate interaction. This also allows for high diffusivity, promoting the growth of islands. In references [293, 298, 304, 305] as well as in this work, however, the interaction is still strong enough to force a stable long-range order within the island, as evidenced by the growth along a crystallographic symmetry axis. The fact that two orbitals of different apparent height are observed for each molecule indicates a slight rotation around the normal of their plane. This asymmetry has also been observed for CuPc on Si [286].

In-plane stacking of phthalocyanines has also been obtained by deposition on an insulating layer, thereby diminishing the influence of the substrate [302, 303]. But while weak interaction has been observed on various passivated and unpassivated semiconducting substrates [248, 252–258, 306], in-plane stacking remains an exception. The stacking mode appears to depend sensitively on the interplay between the properties of the substrate and the molecule and is yet not fully understood.

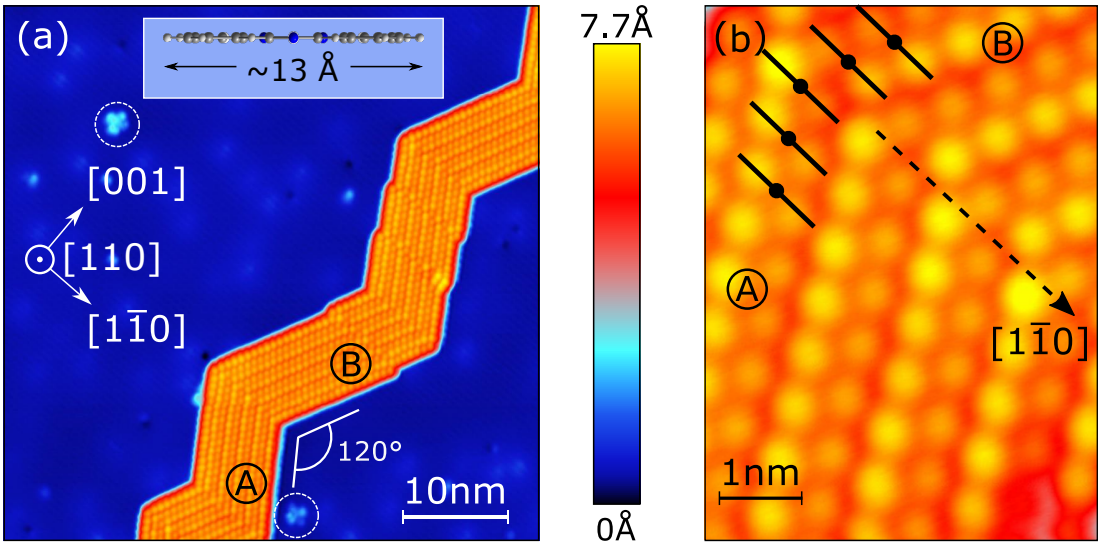

Figure 7.1: (a) Topograph of an FePc island on GaAs(110), I_T=30 pA, V_T=-0.8 V. GaAs lattice directions are indicated. Overall island growth is along the [001] direction. The two coexisting domains are labeled A and B. White dashed circles indicate the positions of two individual, flat-lying molecules. The inset shows a side view of an FePc structural model. (b) Magnified view of the FePc island. Several individual molecules are highlighted by overlaid molecular schematics where black circles and straight lines denote metal center and molecular plane, respectively. The color scale between (a) and (b) applies to both subimages.

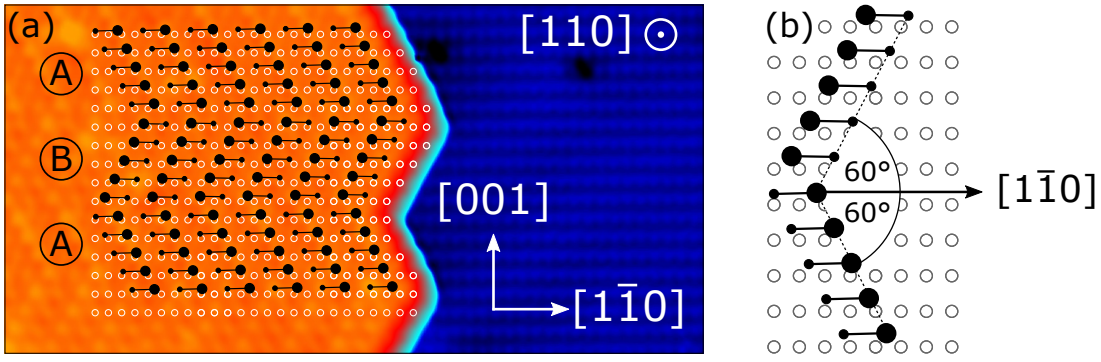

Figure 7.2: (a) Topograph of an FePc island on GaAs(110), rotated with respect to fig. 7.1. I_T=100 pA, V_T=-2.5 V. Molecules are indicated by pairs of filled circles (large and small circles represent higher and lower apparent height, respectively). Open white circles denote the positions of surface As atoms. (b) Magnified depiction of the molecular orientations in the two domains with respective orientation toward [1$\bar{1}$0]. Open gray circles mark positions of surface As atoms. Same color scale as in fig. 7.1.

In the following, the arrangement of FePc with respect to the underlying substrate will be elucidated. In figure 7.2 (a), the positions of individual molecules are indicated by pairs of large and small black circles while the As atoms of the substrate surface are represented by open white circles. For both domain types, nearly commensurate growth is observed along the domain direction, with the brighter part of the molecules preferentially resting in between the atomic rows[3]. Along the $[1\bar{1}0]$ direction no preferred positioning is observed. The angle between the domain directions and $[1\bar{1}0]$ is $60°\pm1°$(see figure 7.2(b)).

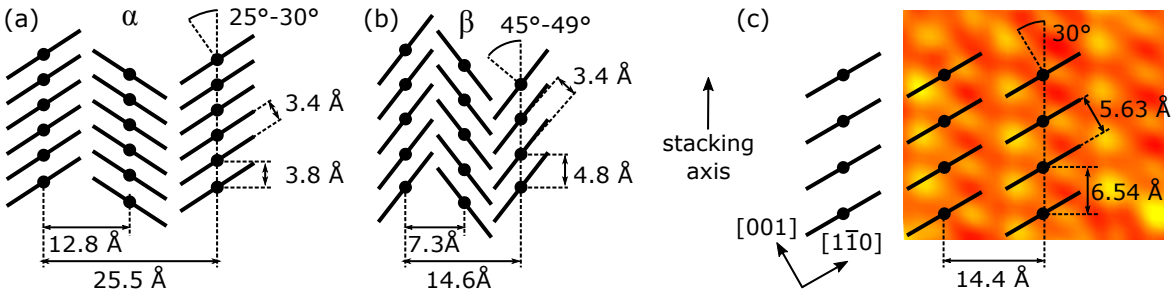

FIGURE 7.3: (a),(b) Schematic representation of the α and β polymorphs of FePc. Characteristic dimensions are indicated. Adapted from [307]. (c) Schematic of the assumed arrangement of FePc on GaAs with dimensions indicated. A possible molecular inclination toward [110] is not considered. Lattice directions of GaAs are shown in lower left corner.

In order to understand the arrangement of FePc within the islands, it is compared to the two common polymorphs of bulk FePc, namely α and β FePc. They are both characterized by a monoclinic structure with a "herringbone like" stacking of the molecules, thereby minimizing steric repulsion. The angle between stacking axis and molecular planes is 25° to 30° and 45° to 49° for the α and β forms, respectively [275, 282, 307–310][4].

Figure 7.3 (a) shows a projection of the bulk crystal structure of the α polymorph of FePc [307, 310, 311]. Two alternating kinds of molecular columns exist. They differ by the direction of their tilting, while the magnitude of the tilt angles is equal. This results in the aforementioned herringbone like packing of the molecules.

[3]This, of course, refers to the apparent position of the molecule, as only the upper orbitals can be imaged by STM. If the molecular plane is inclined towards the surface normal, the bottom orbitals reside at a different lattice position. Such an inclination can neither be deduced nor refuted from topographs.

[4]In contrast to the other references given, ref. [53] describes the α polymorph as not exhibiting the herringbone like stacking.

The FePc β polymorph is very similar to α FePc, but has a larger tilt angle (see fig.7.3 (b)). This allows for a much denser packing with column spacings of just 7.3 Å, as compared to 12.8 Å in α FePc. It is usually considered the more stable compound in large bulk crystals [275, 282, 309]. For small crystals and films grown at room temperature, or for vacuum deposited films on weakly interacting samples, however, the α polymorph appears to be favored [282, 308, 309]. It can be transformed into the β polymorph by heating [312, 313].

Subimage 7.3 (c) shows a schematic of the arrangement of single FePc molecules as found in the islands here, in part superimposed on a topograph for reference. The image is rotated such that the molecular stacking axis is vertical. Typical distances and angles are specified. In the [001] direction, intermolecular distances are (5.63 ± 0.07) Å. This is attributed to the interatomic[5] spacing of 5.65 Å along [001] in GaAs(110) [39]. Along the stacking axis, intermolecular distances are (6.54 ± 0.15) Å. Assuming the molecules to stand perfectly upright on the surface, this implies an angle of 30° between the molecular plane normal and the stacking axis, matching the stacking angle of the α crystal polymorph. If additionally molecules are inclined toward the surface, the angle will be larger accordingly. Within the extent of accuracy that the topographs permit, such an inclination can neither be deduced nor denied, as steep island edges and molecular defect sites usually appear slightly smeared, and asymmetries are introduced by non rotationally-symmetric tips.

The main difference between the growth on GaAs and bulk α and β FePc is the lack of a herringbone packing and the larger apparent intermolecular distances. These two effects are most likely due to molecule-substrate interaction. It is clearly strong enough to force the single molecules into specific positions and orientations, as evidenced by the highly commensurate growth along [001] and the fact that all molecules, with no exceptions found, have their planes oriented along $[1\bar{1}0]$. This indicates that the energetic cost of positioning a molecule at a different angle is higher than the energetic gain resulting from the bulk-optimized crystalline structure as in α and β FePc. Similar observations have been reported for Pc growth on Si(111), where the herringbone stacking is also absent [298].

Despite the larger apparent intermolecular distances, the upright π-π stacking appears to still be favored over a planar arrangement on the substrate. It must be noted that the minimum distances between molecular planes are unknown due to a possible inclination of the molecules toward the surface. For instance, if they were inclined at an angle of $\approx 44°$ toward [110], intermolecular distances would correspond to the α and β FePc bulk value of 3.4 Å.

The molecular islands have also been examined spectroscopically. Figure 7.4 shows spectra of the differential conductance taken on the substrate (black dashed line) and on an FePc molecule within an island (red solid line). The band gap of GaAs is clearly visible. The molecular spectrum is representative of spectra taken on different

[5] "Interatomic" refers to As-As and Ga-Ga spacing. Ga-As spacing is smaller, see section 2.1 for details.

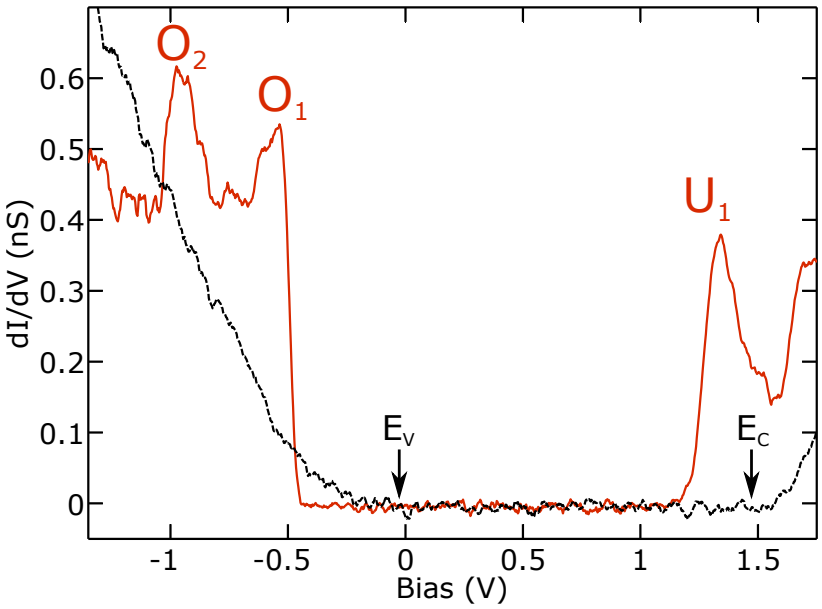

FIGURE 7.4: Representative spectra of the differential conductance taken on FePc island (red solid) and on the substrate (black dashed). Features in the FePc spectrum are labeled as O_2, O_1 and U_1. The actual valence and conduction band edges of GaAs (not considering TIBB) are labeled E_V and E_C, respectively, and are marked with arrows. The feedback loop was opened at -1.4 V and 0.3 nA. A sliding average over ≈ 30 meV was applied to both data sets for smoothing.

positions in both regions of the island. Minor shifts of the peak positions were observed for different tips, but no significant variations were found between island regions A / B or bright / faint molecular protrusion. The spectrum exhibits distinct peaks at -0.93 V, -0.54 V and 1.33 V, labeled O_2, O_1 and U_1, respectively. The valence and conduction band edges of GaAs without consideration of TIBB are marked by arrows and labeled E_V and E_C, respectively. The position of the Fermi level indicates that FePc on GaAs is a p-type semiconductor.

The gap between the highest detected occupied state O_1 and the lowest detected unoccupied state U_1 in the FePc spectrum in figure 7.4 amounts to 1.87 eV. Averaging over 13 measurements, a gap of (1.97±0.09) eV is found, with O_1 at (-0.71±0.12) eV and U_1 at (1.25±0.05) eV. Calculations [277, 314] and measurements [286, 315] of the HOMO-LUMO (highest occupied molecular orbital / lowest unoccupied molecular orbital) gap for FePc bulk crystals, multilayers and gas-phase molecules have found slightly lower energies of 1.38 eV to 1.85 eV.

Below, several possible reasons for a deviation between the gap width measured here and the HOMO-LUMO gaps found elsewhere in literature will be discussed. The most apparent one may be the arrangement of the molecules, as they stand upright.

The relative orientation of molecule and tip determines which orbitals are predominantly contributing to the tunneling current. Their energetic position is decisive for the measured apparent gap. Other orbitals that are potentially residing within this gap might be inaccessible to tunneling due to their spatial orientation. For FePc in general, the HOMO is expected to be located primarily at the central metal atom. Due to the fact that the molecules stand upright, orbitals related to the central atom might not be able to contribute significantly to the tunneling current. Therefore, the measured energy gap may have to be compared to the energy gap of the Pc ring[6] which is around 0.3 eV wider in energy [277].

Another possible reason for a broadening of the energy gap is charge transfer between the molecule and the substrate. For $[FePc]^+$ and $[FePc]^-$, HOMO-LUMO gaps of 1.95 eV and 1.72 eV, respectively, have been calculated [277]. Such a charging can have a drastic effect on the conductance of molecular crystals, as is reported for electron doped FePc [316]. Furthermore, due to the finite resistance of FePc, a non-negligible amount of voltage could drop over the molecular layer [286]. This effect is analogous to tip-induced band bending (TIBB) on semiconductors (see chapter 2.1.2) and would lead to an apparent broadening of the energy gap. Such an effect could be elucidated by recording spectra of the differential conductance at different tip-molecule distances, as the effect of band bending decreases with increasing distance. To the same extent, obviously, the GaAs-related TIBB can alter the voltage scale.

The appearance of distinct structures in the spectra indicate that molecule-substrate interaction is weak, so that the molecular electronic structure is preserved to a large extent. This is in agreement with the observations from topographs described above. Considering the various possible reasons for a broadening of the HOMO-LUMO gap, an assignment of the measured features O_2, O_1 and U_1 to HOMO-1, HOMO and LUMO of FePc appears possible.

Conclusion

FePc self-assembles in a highly ordered fashion on GaAs(110). The exact orientation with respect to the surface cannot be deduced from topographs, but it is apparent that the herringbone like growth known from bulk FePc is not present. Rather, FePc forms parallel molecular chains that grow in a zig-zag manner along the [001] direction.

Measurements of the differential conductance show a pronounced HOMO-LUMO gap that is slightly larger than reported for FePc bulk crystals, multilayers and gas-phase molecules. Several possible explanations for an actual or an apparent broadening of the gap are discussed.

[6] This is the energetic distance between the occupied a_{1u} and the unoccupied $2e_g$ states that are located predominantly at the PC ring and that correspond to HOMO-2 and LUMO, respectively, of the complete molecule [277].

For similar systems of π-π coupled molecules, large charge carrier mobilities perpendicular to the molecular plane have been observed [29, 288, 317], further increasing with the degree of order [29, 281, 287, 289, 303, 318–320]. Considering the well-defined growth and the long-range order of FePc on GaAs, it appears possible that these islands can be used as molecular nanowires or nanoribbons. Similar structures have successfully been fabricated with phthalocyanines before [28, 317, 321–323]. However, the level of order obtained here – both within the islands as well as with respect to the substrate – is exceptional. Compared to CuPc islands on Si, where very high mobilities were observed [28], FePc islands on GaAs are much longer, and neighboring islands run in a parallel manner. Due to the fact that greater order usually yields increased mobility, the islands found here may show highly efficient transport properties.

7.3.2 Growth, electronic structure, and switching of thin AgPc islands

AgPc growth was studied at coverages of $\approx$ 10 %. Island formation resembles that of FePc insofar as it also exhibits upright standing molecules and a unidirectional preferential growth. Figure 7.5 (a) shows a topograph with sections of two parallel islands consisting of a double row of protrusions. In analogy to the discussion for FePc, two neighboring protrusions are assumed to represent one molecule. In the inset, the positions of exemplary molecular units are indicated by black lines.

Thin AgPc islands grow along [001] with few dislocations. They are rather short (some 10 nanometers), and in their surroundings a considerable amount of single molecules (marked with white dashed circles in fig. 7.5 (a)) is observed, suggesting a reduced diffusivity as compared to FePc. It has indeed recently been shown that the central metal atom in phthalocyanines has a noticeable influence on molecular diffusivity and thus on island growth [293].

It is apparent that molecules are predominantly lined up without discernible lateral displacement, yielding virtually one-dimensional in-plane growth. The intermolecular spacing of $\approx$ 5.8 Å matches the projected distance of the underlying As atoms on the growth direction, and each molecule is imaged on top of one As atomic row[7] (see white dotted lines in fig. 7.5). Laterally, their position varies with respect to the substrate atoms. Both orbitals of one molecule appear at the same height, but heights vary between molecules[8]. Possible reasons for these height differences will be discussed later.

[7] This, of course, refers to the apparent position of the molecule, as only the upper orbitals can be imaged by STM. If the molecular plane is inclined towards the surface normal, the bottom orbitals reside at a different lattice position. Such an inclination can neither be deduced nor refuted from topographs.

[8] Similar coverage dependent growth was also observed in preliminary measurements with ZnPc that are not shown here. Thin ZnPc islands, however, did not show the height variations observed for AgPc.

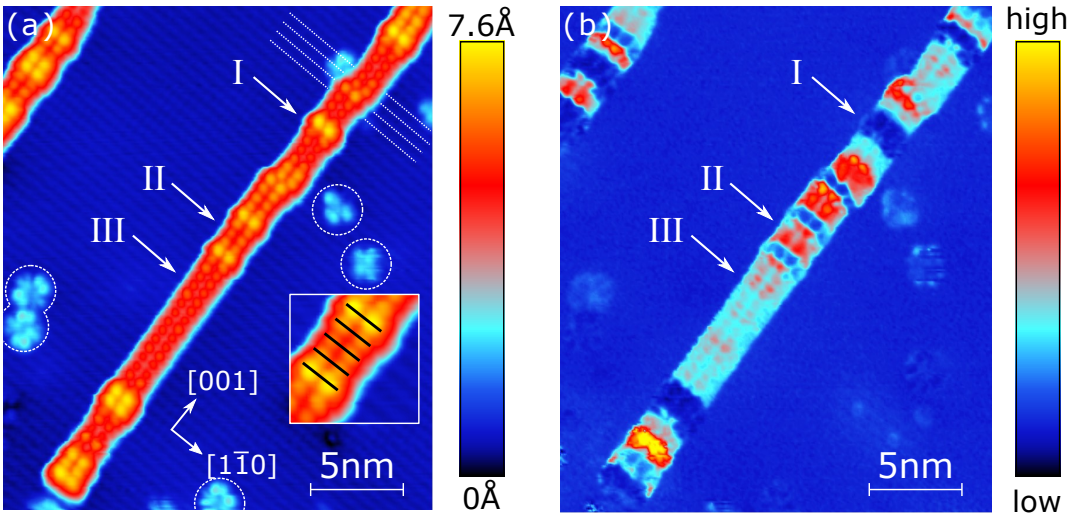

Figure 7.5: (a) Topograph of AgPc islands on GaAs(110), I_T=100 pA, V_T=–1.5 V. The labels I, II and III refer to different regions that are discussed in the text. Dashed white circles indicate individual AgPc molecules. Dotted white lines indicate atomic rows of the substrate. In the inset, the positions of single molecules within the islands are schematically indicated by black lines of 13 Å length. (b) Simultaneously recorded map of the differential conductance for –1.5 V.

At higher coverages, AgPc islands deviate from the monomolecular width and show FePc-like growth as described in the previous section. The height differences as observed within thin islands are not evidenced in broader islands. In the following, only thin AgPc islands with a monomolecular width are discussed.

The gas-phase structure of AgPc was calculated with density functional theory using Gaussian 09 [268] with the B3LYP functional [269–271] and LanL2DZ [272–274] basis set. The calculation is sensitive to the starting coordinates of the central Ag atom. For planar or near-planar starting geometries, the resulting geometry is also planar, while for Ag displacements of $\approx$ 1 Å or more, a shuttlecock structure as shown in fig. 7.6 (b) with the central Ag atom protruding 1.0 Å from the plane defined by the four isoindole nitrogen atoms is obtained. It is thus conceivable that a planar as well as a non-planar geometry exist. The planar geometry has a total energy that is lower by 1.43 eV as compared to the shuttlecock structure. The vicinity to a surface or neighboring molecules (not included in the calculations) may alter the total energies and thus determine the actual conformation of the AgPc molecule in that specific system. It was, e.g., shown that magnesium phthalocyanine (MgPc) – although planar in the gas phase – is non-planar in the bulk crystal. The proximity to the isoindole nitrogen atoms of neighboring molecules causes the central magnesium atom to protrude $\approx$ 0.5Å (varying with temperature) from the molecular plane [324, 325]. This effect may also play a role in the AgPc islands observed here.

One-dimensional growth is usually not observed in phthalocyanine crystals. They predominantly exhibit substantial molecular displacement along the direction of their plane, as they crystallize in monoclinic and triclinic forms [290, 303, 311, 326–331]. For lead phthalocyanine (PbPc), however, a crystal form with one-dimensional stacking has been observed [331–333].

AgPc in its non-planar conformation is similar to PbPc insofar as the latter is also non-planar with the central atom protruding slightly from the phthalocyanine plane [334, 335] (0.9 Å and 1.3 Å have been reported for PbPc in monoclinic and triclinic bulk crystals, respectively [331], and 0.4 Å in one-dimensional columns [332]). It is thus conceivable that AgPc also exhibits a one-dimensional stacking[9] that governs growth in islands of monomolecular width. In literature on AgPc, however, to the best of our knowledge only structural data for a triclinic form have been published [290]. There, a herringbone-like growth is described. It is shown schematically in fig. 7.6 (a) and was already described for FePc in section 7.3.1. A possible molecular arrangement of AgPc on GaAs(110) will be discussed in detail later in this chapter.

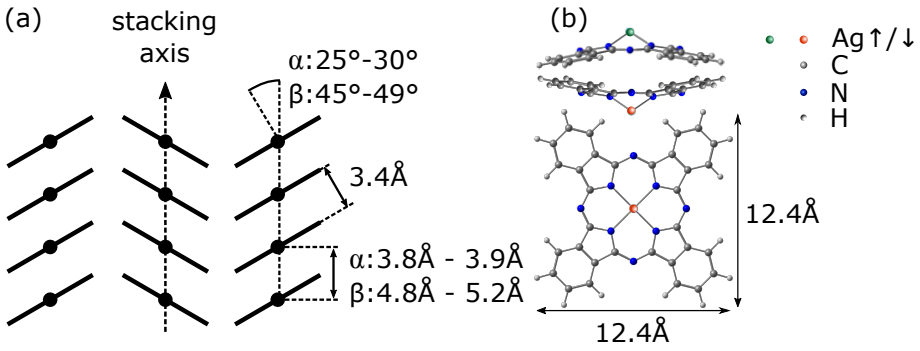

FIGURE 7.6: (a) General stacking of phthalocyanines in the α and β forms in a triclinic crystal. Different intermolecular distances along the stacking axis are related to the different stacking angles. (b) Structure of AgPc in the non-planar ↑ and ↓ conformations, side and top views, as calculated with DFT (see text for calculational details).

Non-planar phthalocyanines on surfaces are expected to exhibit two different conformations, with the central atom at one or the other side (see simplified molecular structure in fig. 7.6 (b)). This has indeed been observed in STM experiments with AgPc [335], PbPc [336] and tin phthalocyanine[10](SnPc) [247], where switching between the two conformations has been reported.

[9]Here, stacking means the lining-up of AgPc parallel to the surface (horizontal/in-plane growth).
[10]Sn atom protruding 1.11 Å from the plane [330].

In the following, the electronic properties of thin AgPc islands will be discussed. Subimage 7.5 (b) shows a map of differential conductance recorded simultaneously with the aforementioned topograph. Three well distinguishable apparent heights are observed within the island and are labeled I (dark blue), II (red to yellow) and III (light blue to reddish). They relate to three different apparent island heights in the topograph: I - high, II - intermediate, III - low. Magnified versions of these regions are shown in figure 7.7, with topographs in the top row (figs. 7.7 (a) to (c)) and maps of differential conductance in the bottom row (figs. 7.7 (d) to (f)). Molecules with lower apparent height also appear a little narrower. The apparent heights of the regions vary strongly with applied bias. For biases between –2.3 V and +1.6 V, region I heights vary between 6.3 Å and 9.2 Å, while region II heights are 5.4 Å to 6.6 Å and region III heights are 5.2 Å to 6.3 Å. For most biases, regions II and III are not distinguishable.

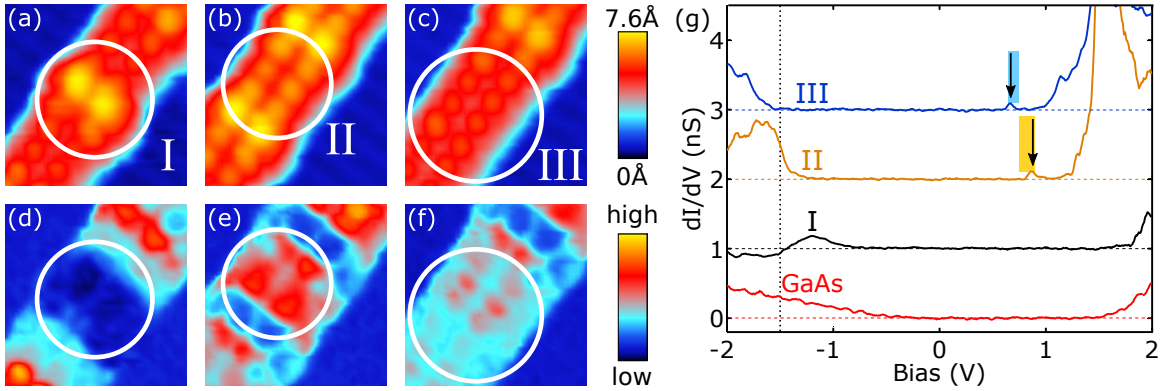

Figure 7.7: Magnified topographs (a)-(c) and maps of differential conductance (d)-(f) at positions I-III of fig. 7.5, I_T=100 pA, V_T=–1.5 V. White circles indicate identical regions in topograph and corresponding map of differential conductance. Image sizes are 4 nm × 4 nm. (g) Spectra of differential conductance taken on regions I, II and III and on the bare GaAs substrate for reference. Arrows indicate lowest energy features within the band gap. Their variation between measurements on different molecules of the same region is indicated by the colored rectangles. Spectra have been slightly smoothed and vertically offset for clarity. The vertical dotted line indicates the voltage where maps of the differential conductance (figs. 7.5, this figure (d) to (f) and 7.8) were taken.

Figure 7.7 (g) shows graphs of differential conductance taken on regions I, II and III[11]. While ≈ 87 % of the spectra taken on region I are featureless between 0 and 1.0 V, peaks in this range are observed in regions II and III. Roughly 75 % of the spectra taken on region II exhibit a peak between 0.75 V and 0.90 V, and ≈ 60 % of the spectra taken on region III show a peak between 0.65 V and 0.75 V (in fig. 7.7(g), yellow and blue colored boxes, respectively, mark these ranges). Further pronounced

[11] A more detailed discussion of the spectra of differential conductance can be found in appendix D for reference.

peaks or shoulders are observed between 1.0 V and 1.5 V in > 80 % of the spectra measured on regions II and III. In region I, only 30 % of the spectra exhibit structures in this interval, and these are mostly weak. As GaAs(110) does not feature any states between 0 and 1.5 V, the observed structures in this bias range are attributed to AgPc and could stem from the molecular LUMO. In general, for the spectra in region I the onset of a strong peak is found at biases above 1.5 V while for regions II and III this occurs between 1.0 V and 1.5 V.

Further small peaks that vary between different tips are observed, e.g. at 1.1 V and –1.8 V in the region III spectrum shown in fig. 7.7(g) or at –1.6 V in the region II spectrum shown. The variation of peak positions and magnitudes renders an interpretation of the observed structures very difficult. Especially at negative bias where band bending is particularly strong, peak positions must always be taken very cautiously. We have thus conducted a statistical analysis of the features found in the spectra of the three regions in order to find recurring structures. It turned out that molecules could be assigned to either of the three regions in a reliable manner by analyzing the peaks found in the spectra of differential conductance. The spectral features were thus used as "fingerprints".

The same applies to the maps of differential conductance. The features in the map are influenced by both topographic and electronic properties of the system. A straightforward interpretation of the apparent heights in the map of differential conductance is not feasible as long as both factors are unknown. For flat systems a normalization scheme has been proposed [89, 337, 338]: Based on a measurement of apparent height as well as constant current differential conductance, the effect induced by the z-dependence of the transmission function is eliminated and a map of differential conductance corresponding to a measurement at constant height is calculated. This method works well for the identification of electronic features on flat surfaces, e.g. standing electronic waves [89]. In the case of AgPc on GaAs, however, topographic features of several Å height and apparent height differences within the island of ≈ 0.7 Å are present. These height differences will easily dominate constant height maps of differential conductance. In fact, when applied to the data shown in fig. 7.5, the calculated constant height map of differential conductance (not shown here) merely reproduces the topographic features of the islands.

Disregarding the reproducible faint peaks in the spectra of differential conductance between 0.65 V and 0.90 V discussed above, the gap width of both region II and III spectra is approximately 2.4 V. With the peaks considered it is ≈ 2.1 V. Spectra in these two regions resemble each other strongly, and only appear to be shifted by ≈ 200 mV against each other. The strong contrast between regions II and III in maps of differential conductance may thus be misleading, as the local density of states (LDOS) at a single voltage is decisive for image contrast. A slight shift of otherwise similar spectra can, for sufficiently steep structures, lead to large deviations in the LDOS at this voltage. The vertical dotted line in fig. 7.7 (g) denotes the voltage where the aforementioned maps of differential conductance were taken. At this voltage, the differential conductance in region II rises steeply while in region III this happens at a

slightly higher negative voltage. This may explain the observed strong contrast between regions II and III[12].

However, great care must be taken when relating maps and spectra of differential conductance, as TIBB can severely alter voltage scales, especially at negative bias (for p-type GaAs, compare section 2.1.2). Due to a relatively low conductance of the molecules at –1.5 V and the fact that maps of differential conductance are taken at a constant current (100 pA), the tip is probably very close to the molecules upon map recording. In contrast, spectra of differential conductance are taken at constant height, with the loop opened at ≈ –2.5 V and a current of 500 pA. At –1.5 V, the current is ≈ 40 pA for spectra of region II and below 1 pA for spectra taken on region III (current data recorded simultaneously with the differential conductance is not shown here). This means that the tip-molecule separation is much larger for spectra than for maps of differential conductance. As mentioned above, this has a strong and position dependent influence on the voltage scale.

Furthermore, it must be noted that the negative bias side of region I spectra exhibits distinct variations between measurements, with strongly differing conduction onsets between ≈ -0.3 V and –1.5 V. For some spectra, negative differential conductance was observed (including the region I spectrum in fig. 7.7 (g)), as reported before for molecules on thin insulating films [339] and on semiconductors [340]. No correlation between topographic variations within region I, exact tip position during the measurements, and spectra could be found. Again, the clear contrast to region II and III spectra is that the conduction onset at positive bias in region I spectra appears at higher energies, and that the majority of these spectra show no or very faint in-gap states at positive bias. The spectroscopic resemblance of molecules in regions II and III indicates that they are electronically similar while molecules in region I exhibit different characteristics.

While initially all three regions coexist, it is possible to induce transitions from types II and III to type I. This is done by applying short (≈ 5 ms) voltage pulses to the corresponding sites. During the pulses, the feedback loop is opened to keep the tip-sample distance constant. Therefore, each voltage pulse is accompanied by a current pulse[13]. Depending on the magnitude of the voltage, switching can be restricted to the molecule directly below the tip, or it can affect a nm sized region, including molecules in neighboring islands. The results of such series of pulses are presented in figure 7.8. Topographs are shown in the top row, simultaneously recorded maps of differential conductance in the bottom row. At the positions indicated by white arrows, voltage pulses were applied as follows: the tip was first moved to the respective position, then the feedback loop was opened at the current $I_{T,0}$ given below each image. Subsequently,

[12]Topographs and maps of differential conductance taken at –1.0 V or below –2.0 V (not shown here) exhibit mainly two different apparent heights within the islands as the contrast between regions II and III diminishes.

[13]Unfortunately, due to limitations of the measurement software the magnitude of the current pulse remains unknown for the data presented here.

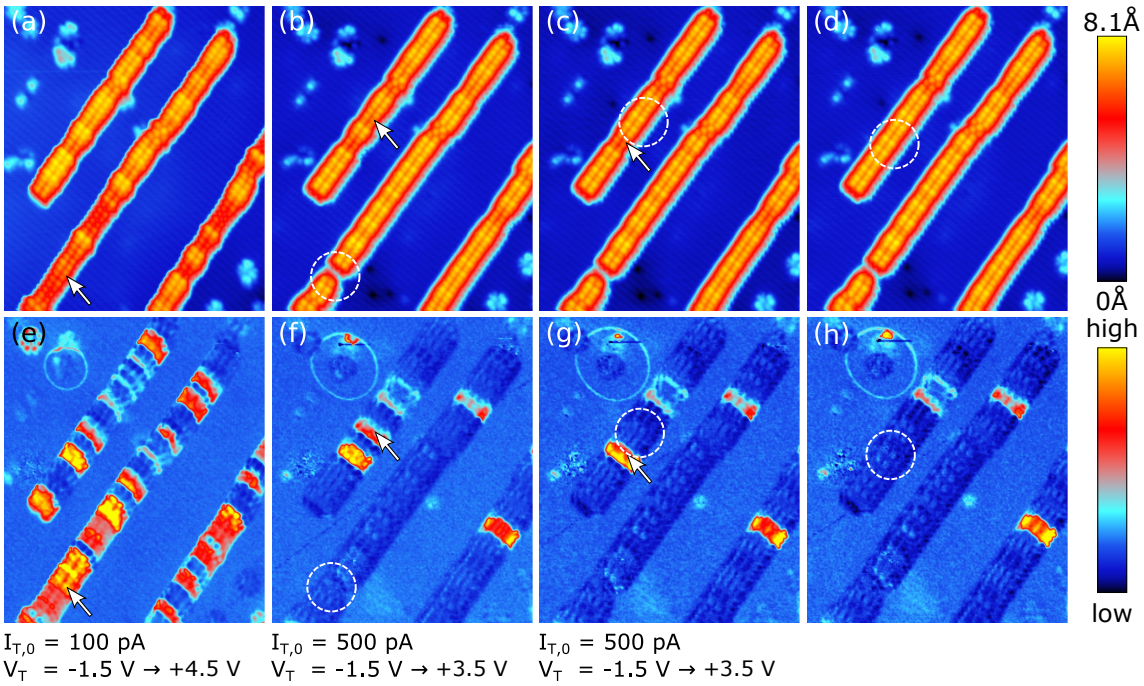

FIGURE 7.8: Voltage induced switching events. Topographs (a)-(d) and maps of differential conductance (e)-(h) are shown. White arrows indicate the positions where voltage pulses are about to be applied, white circles show region of previous pulse. The bright circular feature in the top left corner is attributed to a tip induced charging process, see chapter 6 for a discussion. Image sizes are 24.3 nm × 28.5 nm. $V_T = -1.5$ V, $I_T = 100$ pA. For details on the switching process see text.

the voltage was switched for ≈ 5 ms from the first to the second bias value indicated. Finally, the feedback loop was closed again.

Applying a pulse of +4.5 V (between first and second image) leads to considerable structural as well as electronic modifications. As subimage (b) shows, the pulse causes a local disintegration of the island at the position of its application. Comparing the corresponding maps of differential conductance (e) and (f), additionally a strong non-local effect on regions of type II and III (red to yellow here) is observed. After the pulse, their number is drastically reduced, in favor of regions of type I. This switching will be called *forward switching* below.

Subsequently, pulses with a lower final voltage around +3.5 V are applied to some of the remaining type II and III regions. In this manner, individual regions can be switched without affecting their surroundings. Forward switching was also observed for pulses of opposite polarity. Thresholds were around 3 V for positive bias and –4.5 V at negative bias. While the change evidenced by the measurement of differential conductance is appreciable, the topograph varies only slightly. In particular, no lateral movement of the molecules is observed.

While the switching from type II and III to type I was highly reproducible, the reverse process (switching of type I to II or III, called *reverse switching*) could not be triggered controllably by voltage pulses or high current. Reverse switching was sporadically observed after applying very high voltage pulses above ±4.5 V. In some cases, tunneling at high currents of ≈ 10 nA at moderate voltages also led to the emergence of type II or III regions. Reverse switching may be a statistical process due to a local heating of the molecular environment, as type II and III molecules apparently result naturally during deposition at room temperature.

Several possible explanations for the controlled forward switching will be discussed in the following: tip-induced charging, dehydrogenation, demetalation, a change of the molecular conformation, and the modification of molecule-surface and intermolecular bonds. Some of these possibilities can quickly be discarded. As initially all three regions coexist, a charging of AgPc due to the presence of the tunneling tip appears unlikely. Additionally, no increase in the apparent height around the AgPc – as expected for charged molecules – is observed (compare chapter 6). The initial coexistence of all regions contradicts the idea of a tip-induced dehydrogenation of the outer ligands [335, 341, 342].

Demetalation has been observed in non-planar phthalocyanines before. It was reported that the Pb ion in PbPc can be transferred to the tip of an STM [343]. This is achieved by approaching the tunneling tip toward the Pb ion at the energy of the LUMO until the current drops abruptly, indicating the transition of the Pb atom to the tip. This was only achieved at positive bias (and thus with a negatively charged tip). In consideration of the fact that the central Pb ion in PbPc is positively charged, the orientation of the electrical field at positive sample bias is assumed to support a transition of the Pb ion to the tip.

In our case, although the central Ag ion in AgPc is also positively charged [334] and the orientation of the electrical field is the same as in the report cited above, no transition of a Ag atom to the tip is evidenced in topographs. Furthermore, at high bias extensive non-local effects are observed, and it is hardly imaginable that atoms from several remote molecules can be transferred to the tip at the same time. This leaves a field-induced transition of the metal ion into the surface as the only possible way of demetalation. Beside the electric field being opposed to this process, other objections arise. Firstly, a part of the phthalocyanines on freshly prepared samples is already in the supposedly demetalated state, as evidenced from topographs prior to any manipulation. If thermal energies at room temperature are high enough to initiate this process, however, the existence of the other two regions is unexpected. Secondly, no evidence for an incorporation of the metal ion into the surface is found in topographs. Although the process of a demetalation with subsequent transition into the substrate cannot be unequivocally discarded, the apparent inconsistencies cast it into doubt.

Another explanation is a change in the molecular conformation. For non-planar phthalocyanines, this can be a transition of the protruding central metal atom from one to the other side of the molecular plane (namely AgPc↑ to AgPc↓ or vice versa), or a transition between a planar and a non-planar conformation. It has indeed been shown

for SnPc that resonant tunneling into molecular states can push the central tin atom through the Pc ring [247]. When adsorbed directly on a metal surface this process is irreversible while on a decoupling monolayer of SnPc reversible switching is observed. This difference is explained in terms of the weaker electronic coupling of the second layer molecules to the substrate and a resulting longer lifetime of electronic excitations [246, 344]. The reversible switching is achieved by tunneling into the LUMO+1, thereby stimulating vibronic excitations. The tunneling current begins to fluctuate between two levels at a time scale of seconds, and the desired final state can be settled by selectively reducing the voltage while at one or the other level.

Gas-phase DFT calculations indicate that AgPc exhibits a non-planar configuration with the central metal atom protruding ≈ 1.0 Å from the molecular plane, and AgPc↑ to AgPc↓ switching on Ag(111) has been observed [335]. In addition, a planar configuration that is energetically favorable (lower by 1.43 eV) is found. Although the actual molecular arrangement and conformation cannot be deduced from topographic images, a possible mechanism for a conformational switching in agreement with experimental observations will be proposed below.

One possible arrangement is illustrated schematically in figure 7.9. Subimage (a) shows at the right side the topograph from fig. 7.5 (a), and at the left side a detail where some molecules of different regions are (partially) shown. Subimage 7.9 (b) shows a side view with the suggested arrangement of AgPc molecules. The rippled geometry of the (110) surface [36, 39] is depicted by black and gray filled circles (As and Ga atoms, respectively). The phthalocyanines are stacked along [001] and exhibit three geometric conformations (planar, AgPc↓, AgPc↑). According to their relative heights they are assigned to the three different regions: planar – region I, AgPc↓ – region II and AgPc↑ – region III. The fact that reverse switching of region I molecules cannot be triggered controllably indicates that they are the most stable species. This is in line with the calculated energies of planar and non-planar molecules in the gas phase, where the planar ones exhibit the lowest total energy. It must be noted, however, that the presence of the substrate may alter the electronic states and the geometrical conformations of AgPc. The above assignment should thus be considered a presumption based on the available data. DFT analysis including the substrate and neighboring molecules could perhaps help to elucidate the actual structure.

The actual heights and thus the angles between the molecules and the substrate cannot be deduced from the topograph due to intermixing with electronic effects. We therefore assume that the molecules roughly arrange in a bulk-like manner such that the central Ag atom of each molecule is placed on top of the isoindole nitrogen atom of its neighbor[14] (strictly speaking, this is valid only for molecules of equal conformations). As the molecular spacing along the stacking axis corresponds to the substrate periodicity, the stacking angle (meaning the angle between the molecular plane and the surface normal) can be calculated, and amounts to 37° for shuttlecock AgPc and 36° for planar AgPc.

[14] "On top" refers to a projection onto the molecular plane.

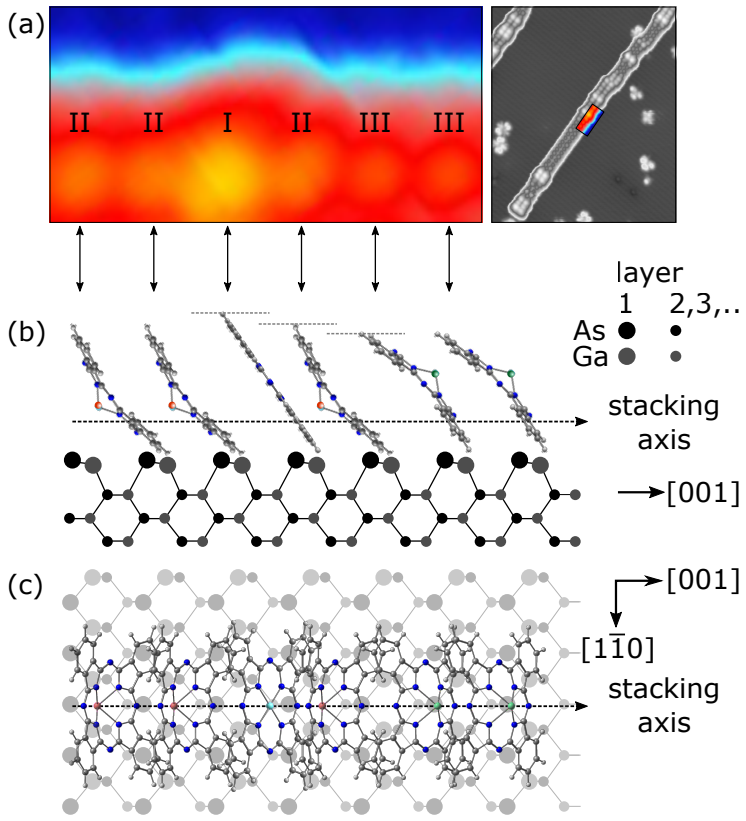

Figure 7.9: (a) Left: detail of fig. 7.5 (a) showing only half of each molecule, with assignment to different regions. Right: position of detail in the topograph (shown in gray scale to enhance visibility, brightness does not represent apparent heights). (b) Assumed arrangement of AgPc on GaAs(110), side view, with relation to topograph. Stacking axis as in fig. 7.6 (a). Dashed horizontal lines indicate heights of molecules in the different regions to illustrate height differences. (c) Same as (b), but top view. Atomic background is shown grayed to enhance visibility of molecules. GaAs substrate representation after [39].

The real arrangement may deviate from this model, as the intermolecular spacing here is much larger than in bulk Pc crystals (4.5 Å vs. 3.4 Å). The molecules might therefore adopt a flatter arrangement in order to establish a reasonable compromise between intermolecular distances and proximity of Ag and isoindole N atoms. Furthermore, AgPc↑ and AgPc↓ may adopt slightly different inclinations due to variations in their molecule-substrate interactions. One possible explanation for the observed difference in apparent height of roughly 0.7 Å between regions II and III is that one molecular species could exhibit a slightly different inclination. This could, e.g., be due to a different interaction with the substrate, as for AgPc↓ the central Ag atom is much closer to the surface than for AgPc↑ (3.7 Å and 6.1 Å, respectively). In fig. 7.9, AgPc↑ molecules are shown at an inclination of 42° to illustrate the effect. However, as the

apparent heights of regions II and III are roughly equal for V < –2 V, this apparent height difference may also originate from slightly deviating electronic configurations.

Within the model proposed above, a transition from type II or III to type I requires a geometrical change from the (meta-)stable non-planar to the energetically favored planar conformation. To initiate the switching process, a certain energy barrier must be overcome. In the gas phase, total molecular energies have been calculated for the stable shuttlecock conformation as well as for slightly distorted conformations[15]. When plotting the total energies (measured relative to the total energy of the optimized planar structure) versus this displacement (see fig. 7.10), a pronounced minimum is found at 0 Å displacement, corresponding to the planar structure. A second, much weaker minimum is found at 1 Å displacement, corresponding to the displacement found in the shuttlecock geometry. Starting from the planar configuration the energy rises monotonically with increasing displacement. Around 1Å displacement, a step and subsequent fluctuation to a value lower by 0.16 eV is observed before the energy starts rising again. These gas-phase data do not explain the rather high threshold needed for switching within the islands. Assuming the model with three different conformations to be correct, the molecular environment must thus have a substantial effect on the energetic and/or geometric structure of AgPc that stabilizes the shuttlecock conformation.

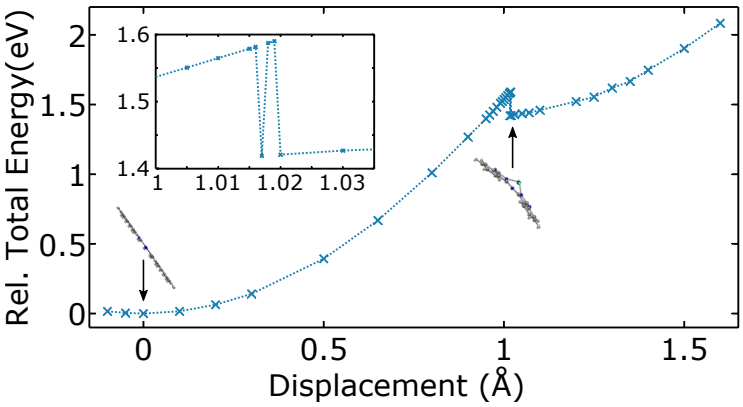

FIGURE 7.10: Relative total energy versus displacement of Ag atom from isoindole N plane for gas-phase AgPc, as calculated with DFT (B3LYP functional, LanL2DZ basis set). Inset shows an enlarged view of the region around 1Å displacement.

Local switching is most likely achieved by means of vibrational excitations. For SnPc, the energetic threshold for SnPc↑ ↔ SnPc↓-switching was found to be between 1.5 eV and 2.5 eV, depending on whether the molecule was adsorbed directly on a silver substrate or on an insulating molecular layer [247]. A combined experimental and

[15]The Ag atom was placed at different distances from the plane defined by the 4 isoindole N atoms, and these 5 atoms were fixed while the rest of the molecule was allowed to relax.

theoretical study found that molecular excitations already occur at energies around 0.9 eV [345], but conformational switching was not examined. For PbPc, demetalation [343] was observed at energies around 2 eV while non-local switching is reported to occur below 2 eV [336][16]. Switching of AgPc adsorbed directly on Ag(111) was achieved at energies of $\approx$ 3 eV [335]. The threshold of $\approx$ 3 eV observed here is in reasonable agreement with these reports. The fact that region I molecules usually do not display in-gap states may lead to a reduced lifetime of electronic excitations within these molecules, effectively preventing local reverse switching.

Non-local switching may be explained in terms of a field-induced process, similar to observations made for tin naphthalocyanine (SnNc) [346]. Due to the nonplanarity of SnNc (and AgPc↑ / AgPc↓) with a protruding, positively charged metal ion, a dipole moment perpendicular to the molecular plane is present. Inverting the field direction may thus exert a force on the central metal ion and invoke vibrational excitations within the molecule. For planar AgPc this process should be reduced due to the lack of an out-of-plane dipole moment, possibly preventing reverse switching.

Conclusion

Upon room-temperature deposition of low coverages of AgPc onto GaAs(110), quasi-one-dimensional islands with the molecules standing at an upright angle toward the surface are formed. Three molecular appearances with different apparent heights are distinguished and attributed to the position of the central metal atom either within, above or below the molecular plane (planar, AgPc↑, AgPc↓) and to different angles between AgPc and the surface normal. Switching to the most stable conformation – presumably the planar one – is achieved locally as well as non-locally in a highly controlled fashion through the application of voltage pulse. The reverse process could not be triggered reliably.

DFT calculations of gas-phase AgPc show two different conformations, an energetically favored planar one and a non-planar one with the central Ag atom protruding $\approx$ 1 Å which is higher in energy by $\approx$ 1.4 eV. Theoretical examination of AgPc including the interaction with GaAs and the intermolecular coupling are required to further understand the arrangement and the electronic properties of AgPc on GaAs(110) and to corroborate the proposed switching model.

The different molecular appearances and the switching are only observed for islands of monomolecular width and only for AgPc. The planar ZnPc forms comparable islands, but does not exhibit different molecular appearances. To the best of our knowledge, similar observations have not been reported so far and further experimental and theoretical examination promises deeper insight into molecular self-assembly on semiconductors.

[16] The threshold value for switching is not given in the reference, and 2 V is mentioned as the upper limit in the experiment.

8 Summary

This thesis reports on scanning tunneling microscopy, spectroscopy and luminescence experiments conducted on GaAs(110). It contributes to the understanding of the interplay of semiconducting surfaces with organic molecules and metallic nanoscale structures.

Porphine molecules adsorbed directly on GaAs(110) were excited by the surface plasmon on a scanning tunneling microscope tip, as evidenced by the detection of molecular fluorescence. Direct excitation by the tunneling current was excluded as the tip resided at nm distance to the closest molecules during luminescence detection. The observation is explained in terms of a radiationless energy transfer from surface plasmons on the tunneling tip to nearby molecules through evanescent waves.

It was further shown that the same process can excite electron-hole pairs in GaAs, as proven by the detection of recombination luminescence with high degrees of circular polarization. These high degrees of circular polarization are due to a spin-imbalance in the GaAs conduction band. It is created by the transfer of spin angular momentum from surface plasmons on suitably shaped tunneling tips, similar to spin-pumping with circularly polarized light. Furthermore, evidence for a low spin injection efficiency from nickel tips to GaAs was provided.

The reversible, tip-induced charging of individual silver phthalocyanine molecules directly adsorbed on GaAs was demonstrated. It was achieved by approaching the tunneling tip to a molecule at sufficiently high voltage. This causes a bending of the GaAs bands, eventually pulling the molecular LUMO below the Fermi level of the sample. Upon charging, a steep increase in conductivity results in a tip retraction so as to maintain a constant current. This leads to a circularly symmetric feature around the molecule which was observed both in topographs and maps of differential conductance.

When evaporated at room temperature, phthalocyanine molecules self-assemble on GaAs. Island growth was found to depend on molecular diffusivity which is strongly influenced by the central metal atom, and on molecular coverage. FePc forms highly ordered and extraordinarily long unidirectional islands that grow in a zigzag manner along the [001] direction. AgPc assembles into shorter islands of monomolecular width, and three different molecular appearances were found within the islands and tentatively attributed to planar and non-planar conformations. Irreversible switching to a stable – presumably the planar – conformation is achieved locally as well as non-locally in a highly controlled fashion through the application of voltage pulse.

9 Outlook

Although this thesis – like so many before – strives to find answers, it inevitably raises many new questions. Hoping that some of these will be addressed in the future, I list possible follow-up work below, without the least claim to completeness.

Concerning the plasmon-induced fluorescence of porphine molecules described in chapter 4, it would be interesting to investigate the distance dependence of the molecular excitation. To this end, single molecules or molecules confined to a well-defined spatial area (e.g. in an island) are needed. Luminescence could then be detected for different tip-molecule separations, ideally in different directions to minimize the effect of an asymmetric tip. The major obstacle is the low light emission efficiency of single molecules. Therefore, an effort should be made to optimize this efficiency. On metals, one way of doing this is to select molecular species with self-decoupling structures [138, 347, 348] or by electronically decoupling them from the substrate by means of insulating layers (e.g. salts [131, 132, 137] or molecular layers [128, 130, 139, 171]), thereby preventing luminescence quenching [123, 125, 126, 349]. Insulating layers often suffer from the disadvantage of covering the whole surface, rendering on-site tip-preparation difficult.

While electronic decoupling is known to enhance luminescence yield on metallic substrates, on semiconductors other effects have to be considered. Photons with energies larger than the band gap will be absorbed by the substrate, leading to decreased emission. In order to prevent this, either semiconducting substrates with larger band gaps (CdS, ZnO, TiO_2, among others) or molecules fluorescing at longer wavelengths may be employed. Furthermore, when the fluorescence can be excited at energies below the band gap and tunneling biases can be chosen accordingly, electron-hole pair

creation and the resulting (unwanted) creation of electroluminescence can be circumvented. Electroluminescence yield can also be greatly reduced by employing indirect band gap semiconductors [113].

In order to further investigate plasmon-induced excitations of spin-polarized electron-hole pairs in GaAs as presented in chapter 5, some variations in the experimental setup should be considered. Firstly, spectrally resolved measurements of the circular polarization of the electroluminescence would be highly desirable. Due to the very low light intensities, however, a setup with an optimized detection efficiency around 850 nm is needed[1]. Secondly, it would be interesting to elucidate the role of the tip shape in the excitation process. Experimentally, one could modify the shape of the tip apex by dropping single atoms or small clusters. The actual shape, however, would remain unknown, rendering the establishment of a clear relationship between tip shape and spin pumping efficiency difficult. Theoretical studies would be appreciable to gain clarity in this respect.

In order to disentangle the effect of plasmon-induced and injection-based electroluminescence, the latter should be minimized. To this end, n-type instead of p-type GaAs could be employed. At low temperatures and sufficiently weak doping, few electrons populate the conduction band (compared to the high hole population in the valence band in p-type GaAs as employed here). When tunneling at negative sample bias, electrons are extracted from the valence band, leaving holes as recombination partners for unpolarized electrons in the conduction band. The lower the electron density there, the lower is the efficiency of this process, allowing for the plasmon-induced excitation to exceed the hole-injection based luminescence. As discussed in chapter 5, plasmonically excited electroluminescence can exhibit high degrees of circular polarizations. For p-type GaAs, this is observable only in a narrow bias range above the conduction band edge, because (mainly unpolarized) injection based luminescence quickly exceeds plasmonically excited luminescence. In n-type GaAs, this bias range could be wider due to the lower light emission efficiency for hole-injection. A similar effect could also be evoked by employing low p-type doping or intrinsic GaAs so as to reduce electroluminescence generation yield.

Chapter 6 focuses on the charging of single phthalocyanine molecules on GaAs(110). So far, no relation was established between disposedness to charging and molecular adsorption position and conformation. AgPc is observed in a variety of appearances that are all stable (in the sense of imeagable by STM) at low temperatures. A systematical study that links the adsorption geometry to spectral signatures and the observation of charge rings would contribute to the understanding of the requirements that need to be met for a molecule to be charged. In order to elucidate the different appearances of AgPc on GaAs and the interaction with the substrate, further theoretical examinations including molecule-substrate interactions could prove helpful.

[1]This refers particularly to a spectrometer and a CCD camera with higher sensitivities at this wavelength. Other optical elements like fibers and lenses can be purchased with near infrared optimized coatings to reduce reflectivity. A minimization of optical path lengths will improve overall performance.

Chapter 7 discusses the formation of phthalocyanine islands on GaAs(110). The adsorption geometry of FePc and AgPc within the islands cannot be deduced from topographs, and the premises for the two different island growth modes remain inexplicit. Theoretical work including the intermolecular as well as the molecule-substrate interactions could elucidate the processes that underlie island formation and could also help to predict carrier mobilities within the islands. Experimentally, island growth could be studied at different coverages and substrate temperatures. Heating, however, must be done very carefully as GaAs(110) quickly develops high defect densities in the surface layer at elevated temperatures. Furthermore, switching within thin AgPc islands should be examined in more detail. Exact thresholds for local and non-local switching are still unknown, and a possible conformational switching of individual, flat-lying AgPc molecules (AgPc↑ / AgPc↓ / planar AgPc) was not studied. As comparably thin islands with very uniform molecular units were observed for the planar ZnPc, further non-planar phthalocyanines like PbPc or SnPc could be employed to elucidate the role of planarity and to corroborate the proposal of a conformational switching.

10
List of Publications

- Svenja Mühlenberend[1], Natalia L. Schneider[1], Markus Gruyters[1] and Richard Berndt[1] *Plasmon-induced fluorescence and electroluminescence from porphine molecules on GaAs(110) in a scanning tunneling microscope.* Applied Physics Letters **101**, 203107 (2012)

- Svenja Mühlenberend[1], Markus Gruyters[1] and Richard Berndt[1] *Fe impurity-induced electronic states at the GaAs(110) surface.* Physical Review B **88**, 115301 (2013)

- Thiruvancheril G. Gopakumar[1], Matthias Bernien[2], Holger Naggert[3], Francesca Matino[1], Christian F. Hermanns[2], Alexander Bannwarth[3], Svenja Mühlenberend[1], Alex Krüger[2], Dennis Krüger[2], Fabian Nickel[2], Waldemar Walter[2], Richard Berndt[1,4], Wolfgang Kuch[2,4] and Felix Tuczek[3,4] *Spin-Crossover Complex on Au(111): Structural and Electronic Differences Between Mono- and Multilayers.* Chemistry - A European Journal **19**, 15702 (2013)

- Svenja Mühlenberend[1], Markus Gruyters[1] and Richard Berndt[1] *Plasmon-mediated circularly polarized luminescence of GaAs in a scanning tunneling microscope.* Applied Physics Letters **107**, 241110 (2015)

[1]Institut für Experimentelle und Angewandte Physik, Christian-Albrechts-Universität zu Kiel, D-24098 Kiel, Germany

[2]Institut für Experimentalphysik, Freie Universität Berlin, D-14195 Berlin, Germany

[3]Institut für Anorganische Chemie, Christian-Albrechts-Universität zu Kiel, D-24098 Kiel, Germany

[4]These authors contributed equally to this work.

11
Acknowledgements

I would never have got to the point of submitting this thesis without the help of many people. I would like to express my sincere gratitude to

Prof. Dr. Richard Berndt, for giving me the chance to work in his group. I genuinely appreciated the excellent working conditions and the freedom to follow my own ideas. I could always be sure of him lending me an ear when I encountered problems, and his ideas were consistently helpful. I learned a great deal from him about how to think well, write clearly and give good presentations.

Priv. Doz. Dr. Markus Gruyters for never giving up on our project, and for letting me profit a lot from his expertise on semiconductors and organic molecules.

Prof. Dr. Peter Unger, Susanne Menzel and Rudolf Rösch from the University of Ulm for generously providing us with custom-made GaAs wafers.

The people who have introduced me to and joined me in the 5K lab: Dr. Natalia Schneider, Dr.Francesca Matino, Dr. Thiruvancheril "Gopa" Gopakumar, Dr. Simon Altenburg, Peter-Jan Peters, Michael Mohr and all the others. It has been a great pleasure to work with you, and I sincerely hope to see the 5K up and running in 10 years time from now.

Dr. Thomas Jürgens, for knowing the RT lab and the 5K lab in unmatched detail and always patiently sharing his ample knowledge on electronics, vacuum systems and "lab magic" in general.

The fine mechanics workshop, in particular the team of Frank Brach. They showed me the fabulous world of fine mechanics and never handed me any part that was less than excellent. Special thanks go to my next-door technician René Woltmann who had the admirable patience to discuss even the most unusual ideas that occurred to me, and who always turned them into something that worked in the end.

Jörg Naubauer and Achim Neumann as well as the electronics workshop around Ali Talmat and Horst Schlüter, who helped me whenever an electrical device discontinued cooperation or when my lack of electronics skills stood between me and the experiment. Further thanks go to Dr. Jürgen Rathlev who would fix any computer-related problem in no time, even those that originated in the eighties, and Joost Jakobs for keeping the vacuum pumps running.

My office mates over the years, especially Peter-Jan Peters, Dr. Nadine Hauptmann and Dr. Natalia Schneider. Whether the discussion revolved around quantum mechanical questions or chocolate cake, it was always delightful!

Monika Seeger, for saving me from bureaucracy and for being such a cheerful person.

All my other colleagues who made my time in this group truly enjoyable and who gave me good reasons to put on a smile when I got to work: Kristof Buchmann, Andreas Burtzlaff, Dr. Manuel Gruber, Dr. Christian Hamann, Torben Jasper-Tönnies, Dr. Sujoy Karan, Thomas Knaak, Prof. Dr. Jörg Kröger, Dr. Lars Mühlenberend, Dr. Nicolas Néel, Neda Noei, Andreas Petersen, Abhishek Rai, Katharina Scheil, Johannes Schöneberg, Dr. Alexander Sperl, Dr. Tomoki Sueyoshi, Dr. Marta Wasniowska, Dr. Alexander Weismann, Dr. Hao Zheng and many more.

Special thanks go to Dr. Nadine Hauptmann, Priv. Doz. Dr. Markus Gruyters, Dr. Alexander Weismann, Peter-Jan Peters and Torben Jasper-Tönnies for proofreading this manuscript, and to Dr. Tomoki Sueyoshi for introducing me to DFT calculations with Gaussian.

Frank-Peter Hohmann for providing me with scientific literature, Jürgen Holz for building custom lab furniture, and Kai Hansen for helping me fight the problems inherent to an old building without ever being annoyed by my constant requests.

The Deutsche Forschungsgemeinschaft, Project GR 1409/5-1 for funding.

The Sonderforschungsbereich 677 for funding

My parents and the rest of my family, for always believing in me and supporting me throughout the years. Special thanks go to Michael for the love and support.

A

Fe impurity-induced electronic states at the GaAs(110) surface

The data presented in this appendix have been published in the journal *Physical Review B* 88, 115301 in 2013 [350]. The coauthors are Markus Gruyters[1] and Richard Berndt[1]. I conducted measurements and processed data, while Markus Gruyters was responsible for data analysis, presentation and writing, in collaboration with Richard Berndt. As the above journal uses a two-column layout, an adaption to a one-column style was made without changing the content.

Abstract

The electronic properties of single Fe atoms in the surface of p-type GaAs(110) are investigated by scanning tunneling microscopy (STM) and spectroscopy. In STM images, Fe atoms show a characteristic structure with an orientation that matches the GaAs substrate lattice. Fe is assumed to occupy substitutional sites in the surface. Spectra of the differential conductance on Fe reveal several distinct peaks. They are discussed in the context of electronic states that originate from hybridization between d orbitals of the Fe atom and p-like orbitals of neighboring As atoms.

[1]Institut für Experimentelle und Angewandte Physik, Christian-Albrechts-Universität zu Kiel, D-24098 Kiel, Germany

Introduction

Transition-metal impurities in semiconductors are of great interest for both fundamental research and technological applications [351, 352]. In diluted magnetic semiconductors, magnetic properties are induced in the nonmagnetic host material by impurities. In view of technological applications, one of the primary goals has been to develop diluted semiconductors with magnetic ordering temperatures above room temperature. Structural properties such as the location and distribution of impurities in the host material play a major role in this context. Since the early 1990s, intense work has been devoted to $3d$ transition-metal dopants such as Mn, Fe, and Co in group III-V and II-VI semiconductor compounds such as GaAs and ZnO [351, 352].

Concerning fundamental research, a scanning tunneling microscope provides a ready means to investigate the structural and electronic properties of impurities in the near-surface region of semiconductors. In recent years, detailed information has been gained particularly on Mn impurities in the group III-V semiconductor GaAs [353–356]. Constant-current scanning tunneling microscopy (STM) images show characteristic features which can be attributed to Mn atoms in the surface and several layers below it [355, 356]. Mn atoms are usually incorporated into the host material by substituting Ga atoms. STM images can be simulated by tight-binding calculations [354, 356, 357].

For Ga substitution by a transition-metal atom, electronic properties are usually determined by p-d hybridization between d orbitals of the transition-metal atom and p-like orbitals of neighboring As atoms [351]. More precisely, the electronic structure may be explained by hybridization between As dangling bonds created by the Ga vacancy and the crystal-field and exchange-split d orbitals of the transition-metal atom located at the vacant site [358]. In the corresponding theoretical approach, a pair of electronic states with t_2 symmetry is obtained from p-d hybridization. One is localized primarily on the transition-metal atom, and the other primarily on the neighboring As atoms. The latter has an energy close to the valence band maximum of the host semiconductor. Because this model applies to the bulk, it is not fully consistent with Ga substitution by a transition-metal atom in the near-surface region. Still, it may be adapted to interpret the electronic states that are related to peaks measured by scanning tunneling spectroscopy (STS) in the vicinity of transition-metal atoms in the GaAs(110) surface [359].

Using STS, distinct impurity-induced peaks in the band gap and close to the conduction band edge of GaAs have been observed for several transition-metal atoms such as Mn [354, 356, 359, 360], Fe [359], Co [359], and Zn [361, 362]. For Fe in the GaAs(110) surface, in particular, two impurity-induced peaks have been found by Richardella et al. for positive sample voltages which mainly corresponds to unoccupied states [359]. For negative sample voltages, mainly corresponding to occupied states, STS has not been reported. In a recent study on GaAs(110) by Bocquel et al., the electronic properties of Fe impurities in the surface, near the surface, and deep below the surface have been investigated by voltage-dependent STM imaging [363]. However, no STS data

showing impurity-induced peaks have been reported. For Fe on InAs(110), four states have been found, two each corresponding to occupied and unoccupied states [364].

In this article, we report on the electronic properties of Fe impurity atoms in the surface of GaAs(110). In contrast to earlier reports from transition-metal impurities, we observe intense Fe-induced features below the valence band maximum, *i. e.*, for occupied states, in addition to the two states in the GaAs band gap observed before. In analyzing the spectroscopic data, in particular from occupied states, it is important to take into account tip-induced band bending. Our detailed experimental results for at least five states will be useful in honing calculations for magnetic impurities in GaAs.

Experimental Details

Experiments were performed in an ultrahigh vacuum apparatus providing a base pressure in the low 10^{-11} mbar range. A home-built STM was operated at a temperature of 5.8 K. Clean and atomically flat GaAs(110) surfaces were prepared *in situ* at room temperature by cleaving small pieces ($8 \times 3 \times 0.3$ mm^3) from a GaAs(100) single crystal wafer. STM images were recorded in constant current mode with the sample voltage V applied between the GaAs substrate (p-type, Zn-doped, $\sim$1–2 $\times 10^{19}$ cm^{-3}) and the tunneling tip. For spectroscopy of the differential conductance, the feedback loop of the STM was disabled and the derivative of the current I with respect to V (dI/dV) was measured by a lock-in amplifier. Electrochemically etched Ni tips were cleaned *in situ* by Ar ion sputtering and annealing. Iron coverages of a few percent of a monolayer were deposited onto the cold substrate in the STM position by sublimation from a wire (99.998 % purity) wrapped around a heated tungsten filament. There is a minor uncertainty in the exact deposition temperature because the temperature sensor was in 2 cm distance from the sample. Due to radiation from the evaporation source, the deposition temperature was therefore slightly above the base temperature of about 5 K but below 10 K.

STM Images and Tunneling Spectroscopy

STM images of Fe atoms deposited on GaAs(110) are shown in Fig. A.1. The color scale is chosen such that the clean and defect-free GaAs surface appears mainly in black to light blue, impurity-induced structures mainly in light green to yellow. The GaAs(110) surface consists of Ga-As zig-zag rows along the $[1\bar{1}0]$ direction with an outward shift of the As relative to the Ga atoms [365, and references therein] [Fig. A.2(a)]. Corresponding STM studies can be found in Refs. [6, 41, 164, 266]. For negative sample voltages, electron tunneling mainly originates from As atoms. The light parallel rows separated by ≈ 5.7 Å in Fig. A.1 are due to As atoms in the Ga-As zig-zag rows along the $[1\bar{1}0]$ direction.

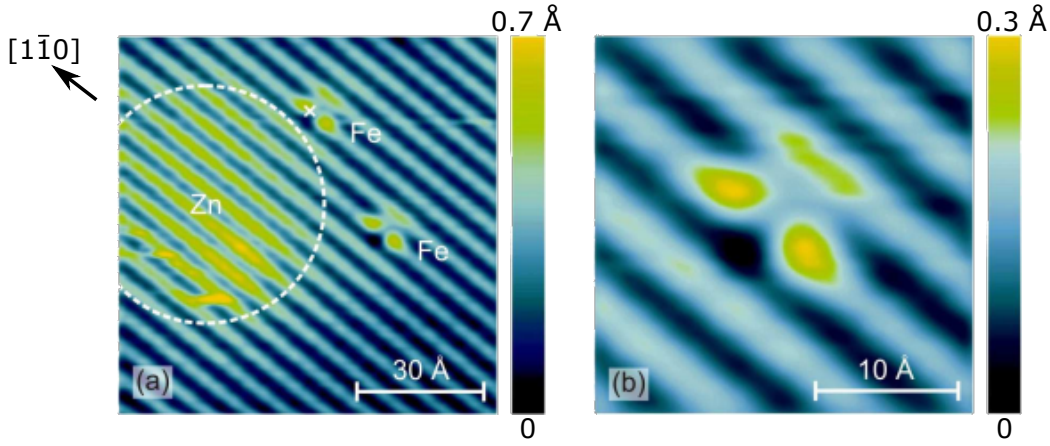

Figure A.1: STM image of Fe- and Zn-induced structures on GaAs(110) for $V = -1.5$ V and $I = 0.1$ nA at $T = 5.8$ K [(b) is a detail of (a)]. The Zn-induced structure extends approximately over the area enclosed by the dashed white circle in (a). At the position marked by the white cross sign in (a), differential conductance has been measured.

The increase in apparent height on the middle left of Fig. A.1(a) extending over a large area of more than 50 Å in diameter is due to a Zn dopant located below the surface [366, 367]. Two additional structures are present, positioned at the right of the Zn dopant. Each results from single Fe atoms. The Fe atom-induced feature is limited to an area of ≈ 13 Å in diameter. It exists of two droplet-shaped protrusions along an As row, a decrease in apparent height in the trench next to it, and an increase in apparent height of elongated shape along a neighboring As row [Fig. A.1(b)]. The whole structure possesses a mirror plane along the [001]-direction.

Almost the same structure has been observed in STM images for Ga substitution by Fe [359] and Mn [354, 359] atoms, respectively. In these studies, the transition-metal

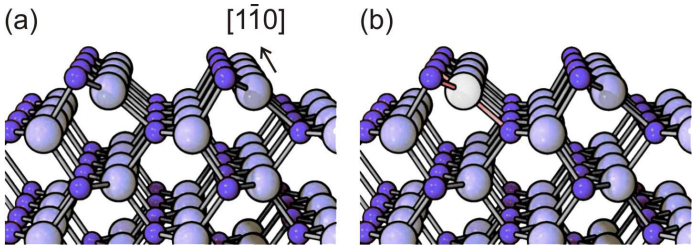

Figure A.2: (a) Schematic side view of the atomic structure of GaAs(110). (b) same as (a) with Ga substitution by an Fe atom in the first Ga layer. As atoms are shown as dark blue spheres, Ga atoms as light blue spheres. Fe atom is shown as white sphere. Figure adapted from Ref. [368].

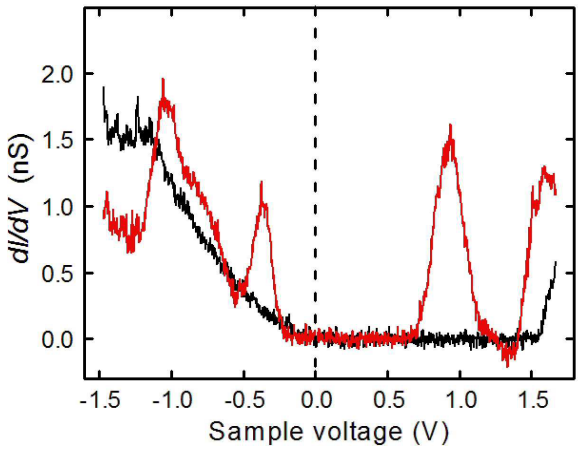

FIGURE A.3: Spectra of dI/dV as a function of sample voltage on the clean GaAs(110) surface (black curve) and on the Fe atom-induced structure (red curve) at $T = 5.8$ K. dI/dV at the Fe atom-induced structure has been measured at the position marked by the white cross sign in Fig. A.1(a) [modulation voltage: 10 mV rms].

atoms have been incorporated in the first Ga layer of the GaAs(110) surface by STM manipulation. In the case of Mn, the assignment of this substitutional site has been confirmed by tight-binding calculations of the STM image [354]. Due to the similarity of the experimental STM images in our and previous works[354, 359], we assume that the Fe atoms shown in Fig. A.1 are located at the same substitutional site as illustrated by the ball-and-stick model in Fig. A.2(b). It should be emphasized that, in contrast to Refs. [354] and [359], no STM manipulation has been used to insert the Fe atom into the surface. In our experiment, manipulation was unnecessary, presumably owing to the known reactivity of semiconductor surfaces towards transition-metal atoms. The substitution of Ga by Fe (or Mn) in the surface of GaAs has been suggested by results from experiments [369, 370] and theory [357, 371–373]. We also attempted STM manipulation of the embedded Fe atoms and have achieved pushing of Fe deeper into the crystal by applying a voltage larger than +1.5 V and a current of 1 nA, similar to recent results on ZnO surfaces [374].

In order to gain information on the electronic properties, tunneling spectroscopy has been performed on the Fe atom-induced structure and on the clean GaAs(110) surface (Fig. A.3). On the bare surface, the differential conductance $\mathrm{d}I/\mathrm{d}V$ is zero for sample voltages between 0 and 1.5 V which is consistent with the energy width of the GaAs band gap. For V < 0 V and V > 1.5 V, $\mathrm{d}I/\mathrm{d}V$ continuously increases reflecting the increase in electronic density of states with increasing energy distance from the valence and conduction band edges.

The simple shape of the dI/dV signal of the clean GaAs surface allows for a straightforward identification of peaks related to Fe. Several distinct peaks are observed in the dI/dV spectrum on an Fe atom: Superimposed peaks at sample voltages of -1.2 V $<$ V $<$ -0.6 V and single peaks at -0.37 V, +0.93 V, and +1.58 V.

In a recent study of tunneling spectroscopy on Fe atoms in the GaAs(110) surface, two impurity-induced peaks at similar values have been found for positive sample voltages [359]. For negative sample voltages, dI/dV has not been reported. Distinct impurity-induced peaks in the band gap and close to the conduction band edge of GaAs have also been observed for other atoms such as Mn [354, 356, 359, 360], Co [359], Zn [361, 362], and Si [375]. In all corresponding dI/dV spectra for negative sample voltages, impurity-induced features do not appear as distinct peaks but rather as shoulders superimposed on a continuously varying background signal of the substrate.

However, the question arises how the peaks induced by the Fe atom (in Fig. A.3) for both V $<$ 0 and V $>$ 0 can be explained by the electronic binding of the impurity within the semiconductor host. Occupied and unoccupied electronic states are obviously involved. For the determination of the corresponding energies, the energy of the tunneling electrons and therefore the sample voltage is decisive. Before discussing the above question in detail, it is necessary to consider electrostatic effects resulting from the interaction of the metallic tip and the semiconducting surface.

Tip-Induced Band Bending

For semiconductors, the potential difference between the tip and the sample surface may substantially deviate from the applied sample voltage because a part of the voltage drops within the interior of the sample due to tip-induced band bending (TIBB) [43]. The amount of TIBB depends on parameters of the semiconductor and the tip such as band gap width, electron affinity, doping concentration, electron effective mass, tip work function, and tip-sample separation.

We numerically determined band bending effects by the method proposed by Feenstra using the program SEMITIP [45]. In this approach, band bending is evaluated by a three-dimensional finite-element method [43] and the tunneling current is computed for a one-dimensional geometry [44]. The parameters used for the GaAs substrate and the Ni tip are as follows: a band gap of 1.52 eV, an electron affinity of 4.1 eV, a Zn doping concentration of 2×10^{19} cm^{-3}, an acceptor binding energy of 0.031 eV, effective masses (in units of the free-electron mass) of 0.0635 for the conduction band, 0.084, 0.643, and 0.172 for the light, heavy, and split off valence bands, a tip-sample separation of 0.7 nm, and a sample temperature of 5.8 K.

For a metallic tip at the GaAs surface, the tip-induced band bending as a function of sample voltage is shown in Fig. A.4 for different values of the tip work function. First, the results for a tip work function of 4.5 eV are discussed. Starting with negative

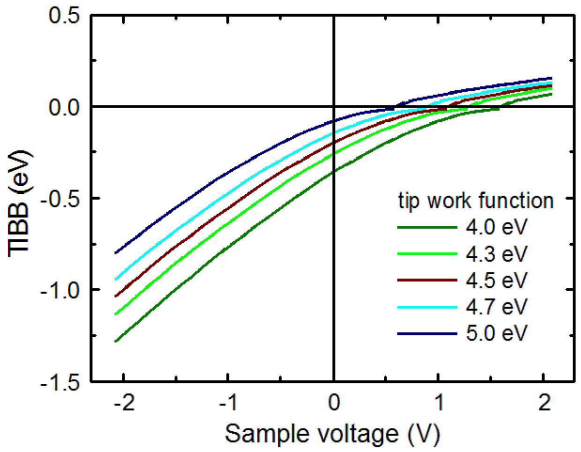

FIGURE A.4: Tip-induced band bending as a function of sample voltage for a metallic tip at the GaAs surface (Zn doping concentration 2 $\times 10^{19}$ cm^{-3}) for five different values of the tip work function, numerically determined on the basis of the program SEMITIP [45]. For further details on the computing parameters, see text.

sample voltage, the absolute value of TIBB decreases with increasing voltage up to $\approx +1.1$ V where flat band condition is reached. With further increasing sample voltage, TIBB increases again but with decreasing slope. TIBB is strongest for negative sample voltages with an almost proportional dependence for $V < -0.9$ V.

The effects of TIBB on the energy diagram of the tunneling junction between the p-type GaAs sample and the metallic tip are illustrated in Fig. A.5 for typical STM imaging voltages of $V = -1.5$ V and $V = +2.0$ V. The Fermi energy is located close to the valence band maximum for p-type GaAs at low temperatures. For $V = -1.5$ V, the sample voltage exceeds the amount of TIBB, which is relatively large. Electrons are tunneling from the valence band of the surface and the bulk of the semiconductor to the tip. The sample is in depletion conditions. For $V = +2.0$ V, the sample voltage overcomes the GaAs band gap. Electrons are tunneling from the tip to unoccupied states in the valence and conduction band. TIBB is small. The sample is in accumulation conditions.

With increasing tip work function from 4.0 eV to 5.0 eV, TIBB changes in a characteristic way (Fig. A.4). The corresponding curve in dependence on sample voltage shows a horizontal and a vertical shift. With increasing tip work function the sample voltage for flat band condition decreases. Additionally, the slope slightly changes. However, the overall shape remains the same. A similar behavior of the TIBB in dependence on sample voltage has been reported for p-type GaAs(110) by Loth et al. [267] apart from the difference of a lower Zn doping of 5×10^{18} cm^{-3}.

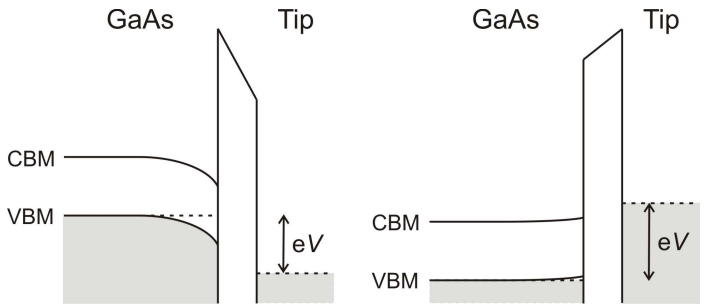

Figure A.5: Schematic energy diagrams of the tunneling junction between the p-type GaAs substrate and the metallic tip for a tip work function of 4.5 eV, in correspondence with the tip-induced band bending shown in Fig. A.4. Two different sample voltages of $V = -1.5$ V (left) and $V = +2.0$ V (right) are chosen. VBM and CBM are the valence band maximum and conduction band minimum, respectively. The Fermi energy within the semiconductor is indicated by the dashed line.

To check the correspondence between the model simulations on the basis of the program SEMITIP and the experiment, the differential conductance density dj/dV has been calculated as a function of sample voltage. For different values of the tip work function, the dj/dV curves are shown together with the experimental dI/dV curve of the bare GaAs(110) surface in Fig. A.6. The scaling between the dj/dV curves and the dI/dV curve is chosen such that an optimum agreement between the calculated and the experimental curve is obtained for negative sample voltages with respect to shape, slope, and voltage dependence. The best agreement is obtained for a tip work function of 4.5 eV. To provide a better comparison, all other dj/dV curves are scaled along the ordinate axis so that they are superimposed on each other for positive sample voltages. An alternative approach is the following (not shown here): The agreement between calculated and the experimental curve is reasonable on both sides of the band gap, *i. e.*, for positive and negative sample voltages, by choosing a tip work function of 4.3 eV. However, in this case, the onset and slope for negative sample voltages is not as well reproduced as for 4.5 eV. Altogether, these results show that our parameters used for the calculation of the differential conductance and therefore of the TIBB are appropriate.

Impurity-Induced Electronic States

Rescaling of the sample voltage with respect to TIBB leads to the dI/dV spectra of the clean GaAs(110) surface and the Fe atom-induced structure shown in Fig. A.7(a). The peak energies obtained from curve fitting after substraction of a background [Fig. A.7(b)] are -0.48 eV (1), -0.35 eV (2), -0.25 eV (3), -0.05 eV (4), $+0.94$ eV (5), and $+1.51$ eV (6). These values provide an appropriate approximation of the energies

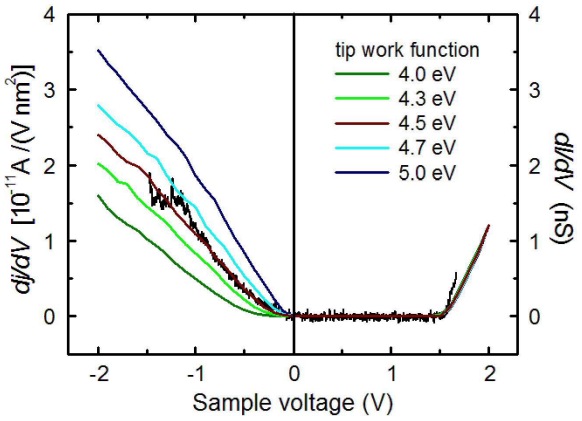

FIGURE A.6: Differential conductance density dj/dV as a function of sample voltage for a metallic tip at the GaAs surface (Zn doping concentration 2 $\times 10^{19}$ cm^{-3}) for five different values of the tip work function, numerically determined on the basis of the program SEMITIP [45] with the same parameters as used for Fig. A.4. For further details, see text. The experimental dI/dV spectrum of the bare GaAs(110) surface from Fig. A.3 is shown in black.

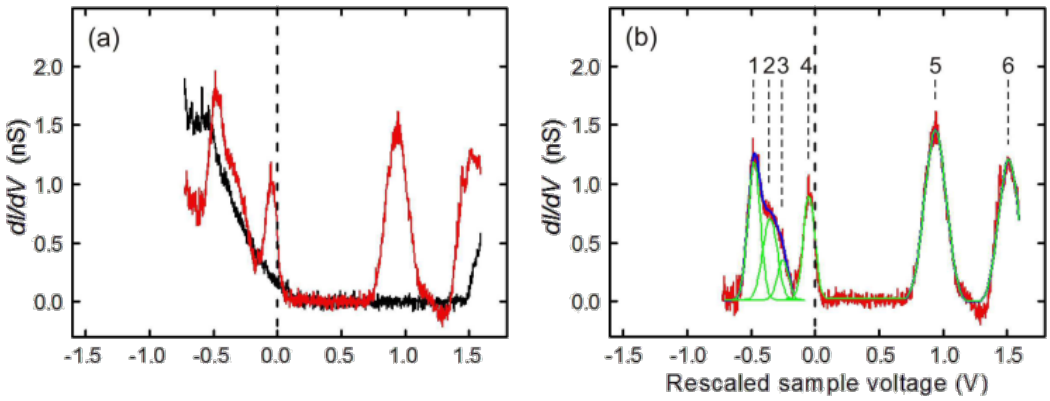

FIGURE A.7: (a) Same as Fig. A.3 with the sample voltage being rescaled by the voltage dependent amount of TIBB given by the calculated curve shown in Fig. A.4 for a tip work function of 4.5 eV. (b) Same as (a) with curve fitting after substraction of a background. Peaks are numbered from 1 to 6 beginning with the lowest sample voltage.

of Fe atom-induced occupied and unoccupied electronic states in the vicinity of the valence band maximum. While the effect of rescaling is small at positive sample bias, which justifies its neglect in previous work [359], significant shifts occur for negative voltages. For example, the single peak at −0.37 V in Fig. A.3 shifts by 0.32 V to −0.05 V and becomes sharper in Fig. A.7. It should be mentioned that peak 3 in Fig. A.7(b) is obtained under the constraint that all occupied states exhibit similar widths. Without this constraint peaks 2 and 3 may be replaced by a single broad peak but with twice the width of peaks 1 or 4. It should also be mentioned that, in this analysis, a single peak is assumed to correspond to a single electronic state. While this is likely the case, it remains possible that more than one state could be hidden within the given widths of the STS peaks.

It should be emphasized that the deduced peak energies vary with the choice of the tip work function, especially in the case of the occupied states, which are strongly affected by TIBB. As discussed at the end of Section IV, the most reasonable agreement between the calculated and experimental properties is obtained for tip work functions between 4.3 and 4.5 eV, with a tendency to 4.5 eV. Higher or lower values lead to major deviations between simulation and experiment. Figure A.4 provides information on how the deduced peak energies change when the tip work function is modified. For a work function of 4.3 eV instead of 4.5 eV, the absolute values of the TIBB increase for negative sample voltages, which results in a further shift of the corresponding peaks towards the valence band maximum in the rescaled presentation of the data. More precisely, for peaks 1–6, the relative shifts amount to +0.08 eV, +0.08 eV, +0.07 eV, +0.07 eV, +0.04 eV, and +0.02 eV, respectively. These values provide a measure for the uncertainty in our analysis of the peak energies, which is non-negligible considering the absolute energy values. Furthermore, our approach is simplified in the sense that uncertainties in the TIBB resulting from, *e. g.*, the shape dependence of the tip work function are neglected.

It should also be discussed that, for semiconductors, one occupied electronic state may lead to two peaks or two features in the dI/dV curve. One may occur if the Fermi energy of the tip crosses the energy of the state, the other, if the energy of the state crosses the Fermi energy of the sample due to TIBB. Such an effect has been observed, *e. g.*, for Mn in GaAs as a shift of the dI/dV curve at negative sample voltages and a relatively broad feature in the dI/dV curve for positive sample voltages above flat band conditions [353]. For the energy levels of Fe in GaAs deduced from the dI/dV curve in Fig. A.7, the state just below the Fermi energy at ≈ -0.05 V has to be considered in this context. Tunneling into this state could be possible for positive sample voltages exceeding flat band conditions, which is, according to the calculated TIBB for tip work functions below 4.5 eV (Fig. A.4), somewhat above ≈ +1.1 V. This voltage is at variance with the two peaks at positive voltages in the dI/dV curve in Fig. A.3. Assuming that the calculated TIBB is appropriate, these peaks appear not to originate from the possibility that the energy of an occupied state crosses the Fermi energy of the sample with increasing positive sample voltage.

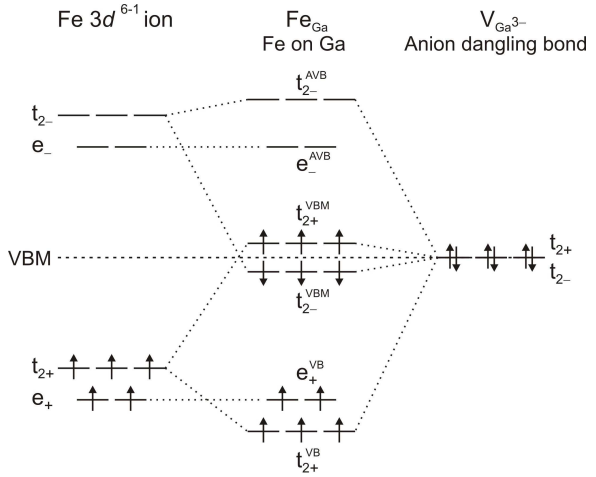

FIGURE A.8: Schematic energy diagram for the crystal-field and exchange-split split electron energy levels of the $3d$ transition-metal atom Fe (left panel), the levels of the As dangling bonds (right panel), and the levels after hybridization between them (middle panel). Fe $3d^{6-1}$ ion means that one d electron and two s electrons of Fe are necessary to complete the As dangling bond state to $t_2(p)^6$, leaving 5 d electrons at the transition-metal atom. The occupation of the energy levels is indicated by up ($\uparrow$) and down ($\downarrow$) arrows according to the spin orientation. Figure adapted from Ref. [358].

We now discuss the origin of the Fe atom-induced electronic properties. As mentioned in the introduction, electronic states induced by a transition-metal atom substituted into bulk GaAs are usually explained by hybridization between $3d$ orbitals of the metal atom and p-like orbitals of the host atoms [351, and references therein]. Here, we adopt conclusions from first-principles electronic structure calculations by Mahadevan and Zunger [358]. In this approach, the electronic structure is interpreted by hybridization between As dangling bonds created by the Ga vacancy ($V_{Ga}{}^{3-}$) and the crystal-field and exchange-split d orbitals of the transition-metal ion located at the vacant site. The energy levels of the Fe $3d$ ion are schematically illustrated in the left panel of Fig. A.8. They comprise four levels of e and t_2 symmetry due to crystal-field splitting and of spin-up ($+$) and spin-down ($-$) character due to exchange splitting. The p-like levels of the As dangling bonds which also possess t_2 symmetry are shown in the right panel of Fig. A.8. They are located close to the valence band maximum (VBM) of GaAs. The energy levels arising from hybridization between $t_{2+}(d)/t_{2-}(d)$ Fe orbitals and $t_{2+}(p)/t_{2-}(p)$ As dangling bond orbitals are shown in the middle panel. In total, six levels exist: Two levels below (t_{2+}^{VB}, e_{+}^{VB}), two levels close to (t_{2-}^{VBM}, t_{2+}^{VBM}), and two levels above the valence band maximum (e_{-}^{AVB}, t_{2-}^{AVB}).

At first sight, it is tempting to assign the six peaks in Fig. A.7(b) to the six energy levels in the middle panel of Fig. A.8. However, the corresponding density functional theory (DFT) calculations of the density of states show that the t_{2+}^{VB} and e_{+}^{VB} levels are located between -3.5 and -4.5 eV below the VBM (Fig. A.1 in Ref. [358]) which is

too far from the lowest energy resulting from the dI/dV spectrum. On the other hand, the t_{2-}^{VBM} and t_{2+}^{VBM} levels are located within 2 eV below the VBM, and, the e_{-}^{AVB} and t_{2-}^{AVB} levels within 1.5 eV above the VBM. These energy ranges are comparable to our experimental results. Considering the energy values, the experimentally determined electronic states below and above the valence band maximum (Fig. A.7) may therefore be assigned to the $t_{2-}^{VBM}/t_{2+}^{VBM}$ and e_{-}^{AVB}/t_{2-}^{AVB} levels (Fig. A.8), respectively. It should be mentioned that the level scheme of the model is based on Ga substitution by Fe in bulk GaAs. As discussed in detail by Richardella et al. [359], the presence of the surface and surface reconstruction lowers the symmetry and therefore may modify the energy level scheme.

Summary

Topographic STM images of single Fe atoms on GaAs(110) show a characteristic structure which is attributed to occupation of a substitutional site in the first Ga layer of the surface. Below and above the valence band maximum, several (more than three) distinct peaks occur in the spectra of the differential conductance on the Fe atom, which, to the best of our knowledge, has not been observed before for any other transition-metal atom in GaAs. One single peak lies close to the valence band edge, and two single peaks occur in the band gap region. Taking into account tip-induced band bending, which is particularly important for the occupied states, the energies of the corresponding electronic states are deduced. Our experimental results support the idea that strong electronic interaction leads to the formation of occupied hybrid states in close vicinity of the valence band maximum.

Acknowledgments

We thank S. Menzel, R. Rösch, and P. Unger from the University of Ulm for generously providing custom-made GaAs wafers. Financial support by the Deutsche Forschungsgemeinschaft through project GR 1409/5-1 is acknowledged.

B

Discussion of the relevant spin relaxation processes in GaAs

As discussed in chapter 5, spin polarized electrons in a semiconductor undergo multiple relaxation processes. Which one is most effective is determined mainly by doping type and density, temperature and kinetic energy of the electrons. Below, the three relevant spin relaxation mechanisms for GaAs – the Elliot-Yafet (EY) process, the D'yakonov-Perel (DP) process and the Bir-Aronov-Pikus (BAP) process – will be discussed and their effectiveness in highly p-doped GaAs at low temperatures will be evaluated.

The EY process is based upon the fact that in the presence of spin orbit coupling, the spin state is not a pure eigenstate but a superposition [376, 377]. Therefore, a spin flip can occur during scattering events. The EY process is relevant for n-type semiconductors at low temperatures and becomes more important for smaller band gap energies [378, 379]. In our case of highly p-doped GaAs, it is negligible.

The DP process originates from a spin splitting of the conduction band for $k \neq 0$, causing two electrons with the same k but different spin to have different energies [380, 381]. This splitting can be described as a k-dependent effective magnetic field, around which the spins precess between scattering events. As scattering is a statistical process, this leads to a spreading of the electrons spin orientations. DP spin relaxation is dominant in n-type semiconductors at temperatures above a few K. In p-type material it is relevant at low doping concentrations. For p-GaAs at 6 K, it is the primary spin relaxation mechanism below a doping density of $\approx 10^{15}\ cm^{-3}$[378, 379], which is much lower than in the present experiment. For strongly doped samples, it becomes important for electron kinetic energies above $\approx$ 300 meV, as the DP relaxation rate increases with the cube of the energy [213, 380].

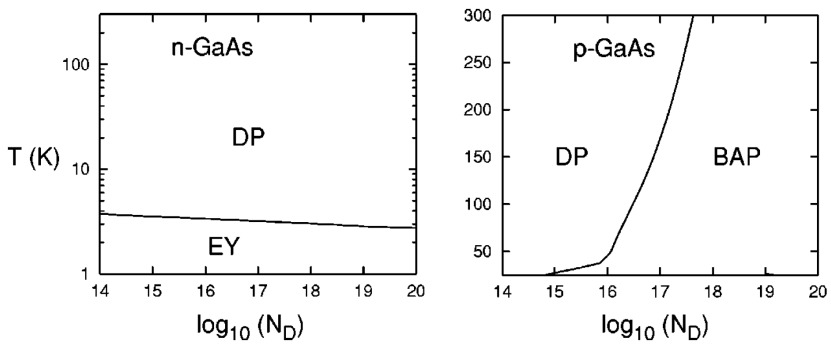

FIGURE B.1: Calculated spin relaxation regimes for n- and p-type GaAs as a function of dopant density and lattice temperature, taken from [378].

The BAP process stems from electron-hole exchange interaction and is important in p-doped material [382]. At 5 K and for low injection energies, it is the dominant relaxation mechanism starting from a doping concentration of $\approx 10^{15}\,cm^{-3}$. Above $\approx 10^{18}\,cm^{-3}$, it even prevails up to room temperature [378, 379]. Working at 6 K with highly p-doped GaAs, we can assume that BAP is the primary spin relaxation mechanism in our system for energies below ≈ 300 meV [212, 213]. Relaxation times depend strongly on the exact doping concentration and temperature. For $N_A = 10^{19}\,cm^{-3}$ and temperatures in the range of 25 to 60 K, values in the ns range have been reported by theory [378, 379]. For temperatures around 5 K, these times are expected to augment by roughly an order of magnitude [379].

C

Error estimate for the TIBB calculation

In chapter 6, the TIBB is estimated by means of the program "Semitip" by Randall M. Feenstra [43, 45]. The system to be simulated is described via the specification of multiple physical parameters. They include the tip sample distance z, the contact potential difference between tip and sample E_{cp}, the doping density p, the temperature T and the band gap energy E_g. These parameters exhibit non-negligible uncertainties that lead to significant deviations in the calculation of the TIBB. In this appendix, reasonable ranges for the parameters will be given and the effect on the calculated TIBB will be examined. Table C.1 summarizes the parameters with their considered range of values and specifies the value selected for the calculation in chapter 6.

The absolute tip sample distance z is generally unknown in STM experiments. However, measurements of the conductance vs. z allow for an estimation. For typical tunneling conditions, a value of $\approx$7 Å is considered reasonable [67]. On semiconductor surfaces, some peculiarities arise. For voltages close to the band gap, the tip sample distance will vary in a disproportionate manner, as conductivity changes steeply [266]. For spectra of differential conductance, it is thus important at which starting voltage the feedback loop is opened, as this fixes the z position. For an exact estimation of the z variation in the band gap region, spectra of z vs. V_T, recorded at constant current, would be needed. Unfortunately, the present setup does not allow for this measurement mode. Therefore, a rather broad z range of 5 Å – 10 Å is considered for the error estimate.

The contact potential is calculated as described in reference [44] as $E_{cp} = \Phi_t - \Phi_s$ with Φ_t, Φ_s the work functions of tip and sample, respectively. Φ_s is the energy from the sample Fermi level to the vacuum, and can also be written as $\Phi_s = \chi - (E_C - E_F)$ with χ the electron affinity of the sample, and E_C and E_F its conduction band energy and its Fermi energy, respectively. The work functions are afflicted with relatively

large uncertainties[44, 383–387], and for the STM tip strong variations with the apex geometry are observed [267]. Therefore, a rather wide range of -0.84 eV to -1.45 eV was considered for the calculation.

The doping density p of a semiconductor single crystal boule may vary considerably between its tail and its seed end. In the present case, the specification given by the manufacturer (Wafer Technology Ltd.) covers a range of 2.1×10^{18} cm^{-3} to 1.3×10^{19} cm^{-3}.

The temperature of the sample during measurement cannot be determined exactly, as the temperature diode is mounted at the side of the STM. The sample may be slightly warmer due to radiative heat transfer from nearby components that are not at liquid helium temperature. The temperature range is estimated to be 5.0 K to 8.0 K, based on experimental observations made during sample transfers.

The band gap E_g depends slightly on doping density and temperature [122, 202]. As those two parameters vary, the band gap, too, does. For the given ranges of p and T an energy gap between 1.46 eV and 1.50 eV is calculated.

Parameter	Range	Selection	References
z	5 Å – 10 Å	7 Å	[67]
E_{cp}	-0.84 eV – -1.45 eV	-0.94 eV	[44, 383–387]
p	2.1×10^{18} cm^{-3} – 1.3×10^{19} cm^{-3}	5×10^{18} cm^{-3}	wafer specification
T	5.0 K – 8.0 K	5.0 K	exp. observation
E_g	1.46 eV – 1.50 eV	1.49 eV	[122, 202]

TABLE C.1: Considered uncertainty ranges for the varied parameters.

Figure C.1 (a) shows the calculation of TIBB vs. bias as discussed in chapter 6. The red line shows the calculation for the selected parameters, while the other lines result from variations of single parameters. Calculations were conducted for the extreme values of each range. Dashed lines mark results from lower boundary values, while solid lines represent calculations using the upper boundaries.

The black lines represent the results for a variation of the z-value. It is seen that the TIBB becomes more pronounced for decreasing tip-sample distances. As the band bending is caused by the electrostatic potential of the tip, this behavior is expected.

The green lines result from calculations with varying contact potentials. The higher the work function difference is, the larger the band bending. For the upper boundary, the flat band condition is significantly shifted, compared to all other variants. This rather strong influence of the work functions on the TIBB has been reported in the literature [267]. As the tip work function depends on parameters such as surface roughness, possible adsorbates and apex shape, the TIBB measured with different tips can vary strongly. The purple lines shows the influence of the acceptor density. For higher dopant concentrations, the TIBB is less pronounced. This is due to a more efficient screening of the electric field of the tip when more free carriers are available.

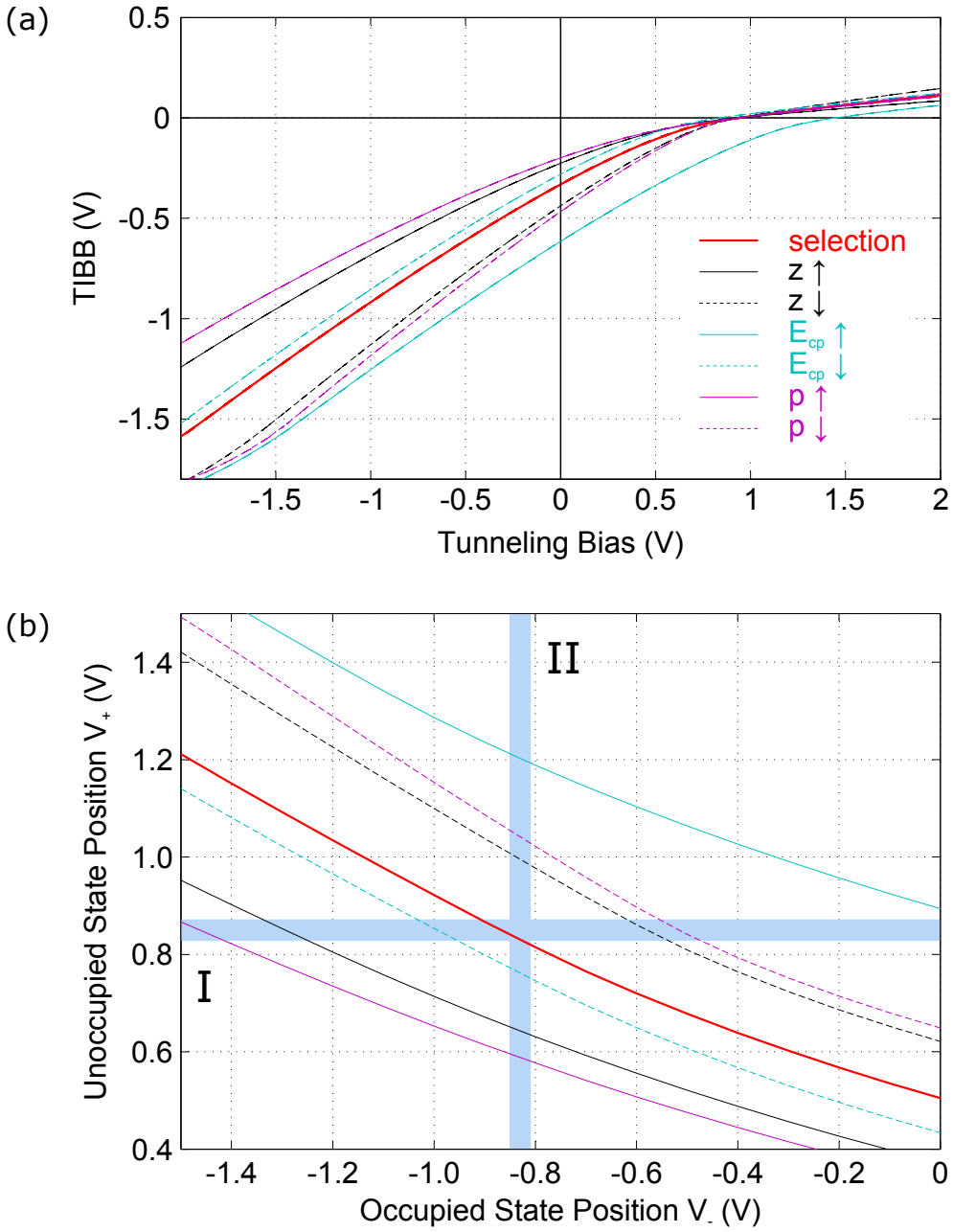

FIGURE C.1: Calculations of (a) TIBB and (b) transformation from occupied to unoccupied state position as discussed in chapter 6 including additional results with single parameters varied. The legend applies to both subimages. Solid and dashed lines mark calculation for maximum (↑) and minimum (↓) values of the considered ranges for each parameter, respectively. The light blue lines in (b) represent the peak positions I and II (unoccupied and occupied LUMO) as found in the spectrum of differential conductance shown in fig.6.4.

The variation of T and E_g in the given ranges has negligible influence on the TIBB. Thus, in fig. C.1 no results for those parameters are shown.

Figure C.1 (b) shows the relation between the energetic positions of the occupied and the unoccupied variant of the LUMO (compare fig.6.6) for the selected parameters (red line) as well as with single parameters varied. Again, the minimum and maximum values of each range have been used. As for the TIBB, varying the temperature and the band gap has a negligible effect. However, it is evident that the variation of the other parameters within reasonable ranges can lead to a strong disagreement between observation and calculation.

In conclusion, calculations of the TIBB must be considered with precaution, as the uncertainty of the underlying parameters is clearly noticed in the results. Predictions based on these calculations, like the estimation of the shifting of a LUMO due to TIBB, are also afflicted with large uncertainties.

D

Spectra of differential conductance on AgPc islands

In fig. 7.7 (g) of section 7.3.2 (p.71), representative spectra of differential conductance taken on the different regions (I, II and III) of AgPc islands on GaAs as well as on the substrate are shown. For further reference, fig. D.1 depicts a more extensive selection of spectra. For each region, spectra taken with at least two different tips are shown. Before the measurements on AgPc, a spectrum on the bare GaAs was taken for each tip and only those tips that showed a clean band gap were used. The tunneling conditions under which the feedback loop was opened are annotated at the left side (color-coded according to the data) and are similar for most of the spectra. Some strong features of region II spectra are clipped due to an exceedance of the lock-in amplifier range.

As described in section 7.3.2, the different regions are assigned to different conformations of AgPc: I – planar AgPc, II – shuttlecock AgPc↓, and III – shuttlecock AgPc↑. In fig. D.1, calculated energies for gas-phase AgPc in the shuttlecock (regions II and III) and planar (region I) conformations are displayed as red and black vertical lines for reference. Red lines indicate that the orbitals are (at least partly) located at the outer ligands and are therefore directly accessible to the tunneling current, while black lines mark those states that are predominantly located at the metal center and the inner part of the macrocycle and do not extend to the ligands. As the calculation was done for the gas phase, the absolute energetic positions of the orbitals with respect to the energy scale of the measured spectra must be assessed. This was done by shifting the LUMO of the calculated orbitals to the first observed peak at positive bias in regions III and I for the shuttlecock and the planar geometry, respectively (slight shifts in peak position within the regions and between regions III and II are not considered,

as otherwise many sets of calculated energy positions would have to be shown which would strongly impair clarity).

In regions II and III, spectra of dI/dV show a small peak between 0.65 V and 0.9 V and a multitude of features of different magnitude starting at a voltage of $\approx$ 1 V. All spectra of regions II and III show a pronounced peak between $\approx$ 1.5 V and 2 V. In addition, smaller shoulders or peaks at varying positions are observed in all spectra. At negative bias, regions II and III show features below -0.4 V and -0.5 V, respectively, with a rather pronounced peak at $\approx$ -0.7 V. Only one spectrum of region III deviates strongly and shows a broad feature between -0.6 V and -1.4 V, possibly due to different tunneling conditions (see data to the left of the graph).

For region I spectra only one strong peak at $\approx$ 1.9 V with shoulders toward lower energies is detected within the probed positive bias range. At negative bias, broad features are observed below $\approx$ -0.9 V. Two of the spectra show negative differential conductance.

In general, features occurring at negative bias are subject to strong TIBB which shifts them toward higher negative bias and makes an assignment of calculated to measured energy positions unreliable. However, also for positive bias it is apparent that the positions of the calculated states do not reproduce the measured structures satisfactorily, neither for the assumed planar nor for the shuttlecock geometry. This indicates that the simple theoretical examination of gas-phase AgPc is not suitable to describe the present rather complex system. In contrast, the spectra of differential conductance of flat-lying AgPc molecules (shown in fig. 6.4 in section 6.3, p.55) are in good agreement with results from gas-phase DFT. This suggests that molecule-substrate interaction may be weak, while molecule-molecule interactions within islands play an important role. Including the latter into the calculation could thus be a first step to improve the theoretical description of the system.

It should, for the sake of completeness, be noted that the measured dI/dV spectra of upright standing and flat lying molecules cannot readily be compared with each other. The main reasons for this are firstly the different accessibility of molecular states: in the case of a tilted AgPc, orbitals located on the central Ag atom or the inner part of the macrocycle may be "covered" by the outer ligands of a neighboring molecule. Secondly, the delocalized π electrons in the polar AgPc are affected by the electric field in the tunneling junction [388]. Depending on the relative orientation of molecule and electric field this will lead to different redistributions of the electrons. Finally, upright standing molecules are only found in islands. They are thus per se different from the flat-lying species as intermolecular interactions will likely alter their electronic properties.

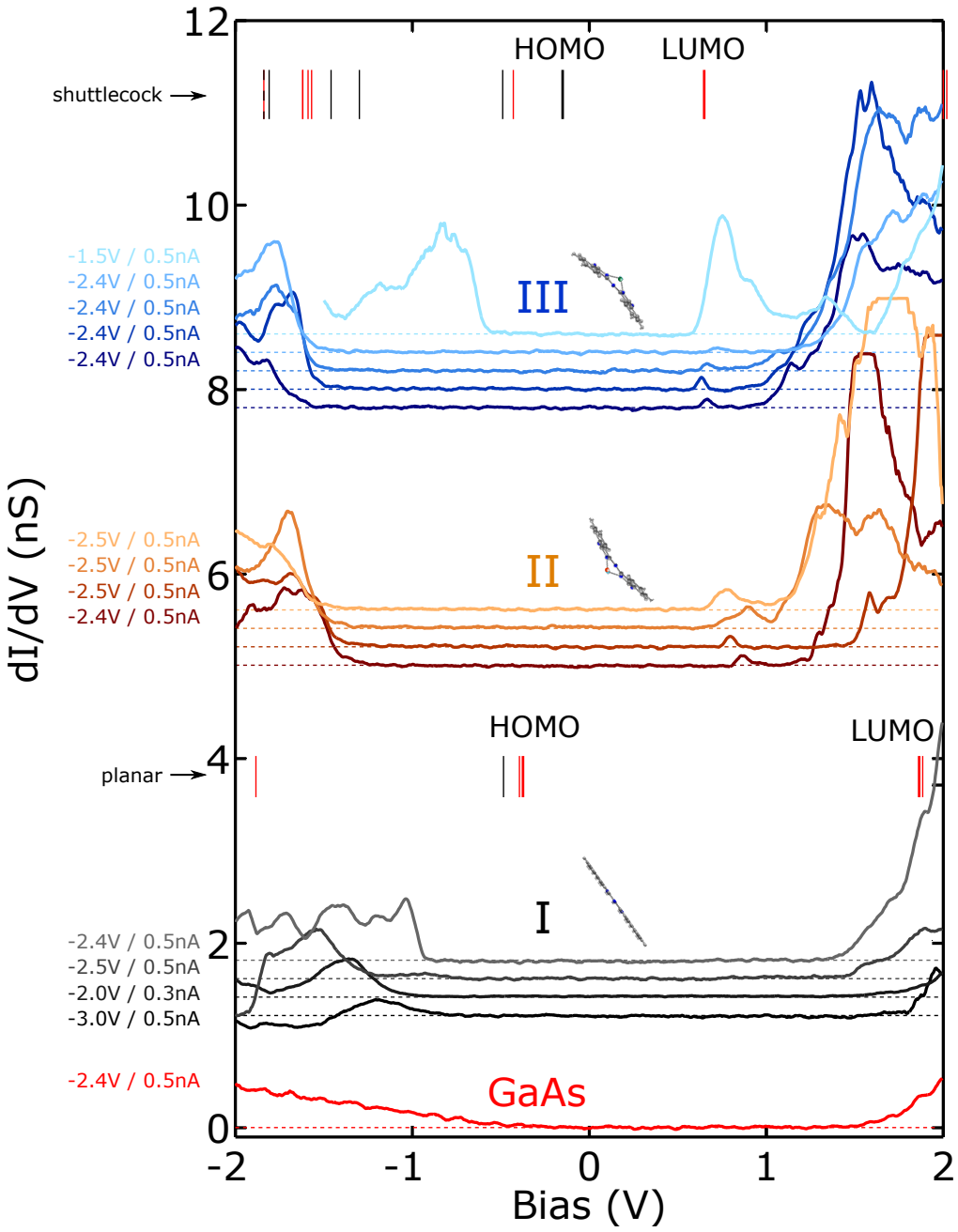

FIGURE D.1: Spectra of differential conductance taken on AgPc islands on GaAs (compare fig. 7.7 (g) in section 7.3.2), vertically shifted for clarity. I, II and III denote the repective regions where spectra were taken, bottom one was taken on the bare substrate for reference. Vertical lines indicate calculated energies of molecular orbitals of AgPc in the planar (region I) and in the shuttlecock (regions II and III) conformation. Red lines refer to orbitals located on the ligands, while black lines denote orbitals without ligand-based contributions. Thicker lines mark gas-phase HOMO and LUMO states. Color-coded values at the left denote the tunneling conditions under which the feedback loop was opened.

Bibliography

[1] W. E. Spicer. *Surface and interface states on GaAs(110): Effects of atomic and electronic rearrangements.* J. Vac. Sci. Technol. **14**(4), 885 (1977).

[2] E. M. Conwell and R. D. Burnham. *Materials for integrated optics: GaAs.* Annual Review of Materials Science **8**(1), 135 (1978).

[3] W. Ranke and K. Jacobi. *Structure and reactivity of GaAs surfaces.* Progress in Surface Science **10**(1), 1 (1981).

[4] J. S. Blakemore. *Semiconducting and other major properties of gallium arsenide.* Journal of Applied Physics **53**(10), R123 (1982).

[5] J. S. Blakemore, ed. *Gallium arsenide.* No. no. 1 in Key papers in physics (American Institute of Physics, New York, 1987).

[6] R. M. Feenstra, J. A. Stroscio, J. Tersoff, and A. P. Fein. *Atom-selective imaging of the GaAs(110) surface.* Physical Review Letters **58**(12), 1192 (1987).

[7] M. R. Brozel, ed. *Properties of Gallium Arsenide.* No. 16 in EMIS datareviews series (INSPEC - The Institution of Electrical Engineers, London, 1996), 3. ed ed.

[8] W. Dumke, J. Woodall, and V. Rideout. *GaAs-GaAlAs heterojunction transistor for high frequency operation.* Solid-State Electronics **15**(12), 1339 (1972).

[9] S. M. Sze and K. K. Ng. *Physics of semiconductor devices* (Wiley-Interscience, Hoboken, N.J., 2007).

[10] R. J. Keyes and T. Quist. *Recombination radiation emitted by gallium arsenide.* Proceedings of the IRE **50**(8), 1822 (1962).

[11] J. I. Pankove and J. Berkeyheiser. *A light source modulated at microwave frequencies.* Proceedings of the IRE **50**(9), 1976 (1962).

[12] R. N. Hall, G. E. Fenner, J. D. Kingsley, T. J. Soltys, and R. O. Carlson. *Coherent light emission from GaAs junctions.* Physical Review Letters **9**(9), 366 (1962).

[13] M. I. Nathan, W. P. Dumke, G. Burns, F. H. Dill, and G. Lasher. *Stimulated emission of radiation from GaAs p-n junctions.* Applied Physics Letters **1**(3), 62 (1962).

[14] T. M. Quist, R. H. Rediker, R. J. Keyes, W. E. Krag, B. Lax, A. L. McWhorter, and H. J. Zeigler. *Semiconductor maser of GaAs.* Applied Physics Letters **1**(4), 91 (1962).

[15] C. H. Henry. *Limiting efficiencies of ideal single and multiple energy gap terrestrial solar cells.* Journal of Applied Physics **51**(8), 4494 (1980).

[16] M. A. Green, K. Emery, Y. Hishikawa, W. Warta, and E. D. Dunlop. *Solar cell efficiency tables (version 45): Solar cell efficiency tables.* Progress in Photovoltaics: Research and Applications **23**(1), 1 (2015).

[17] D. T. Pierce and F. Meier. *Photoemission of spin-polarized electrons from GaAs.* Phys. Rev. B **13**, 5484 (1976).

[18] H. Siegmann. *Spin polarized electrons.* Europhys. News **14**(2), 9 (1983).

[19] S. F. Alvarado and P. Renaud. *Observation of spin-polarized-electron tunneling from a ferromagnet into GaAs.* Phys. Rev. Lett. **68**, 1387 (1992).

[20] V. P. LaBella, D. W. Bullock, Z. Ding, C. Emery, A. Venkatesan, W. F. Oliver, G. J. Salamo, P. M. Thibado, and M. Mortazavi. *Spatially resolved spin-injection probability for gallium arsenide.* Science **292**, 1518 (2001).

[21] I. Zutić, J. Fabian, and S. Das Sarma. *Spintronics: Fundamentals and applications.* Rev. Mod. Phys. **76**, 323 (2004).

[22] G. Schmidt. *Concepts for spin injection into semiconductors – a review.* J. Phys. D: Appl. Phys. **38**, R107 (2005).

[23] J. Levy, V. Nikitin, J. M. Kikkawa, A. Cohen, N. Samarth, R. Garcia, and D. D. Awschalom. *Spatiotemporal near-field spin microscopy in patterned magnetic heterostructures.* Phys. Rev. Lett. **76**(11), 1948 (1996).

[24] A. V. Akimov, A. Mukherjee, C. L. Yu, D. E. Chang, A. S. Zibrov, P. R. Hemmer, H. Park, and M. D. Lukin. *Generation of single optical plasmons in metallic nanowires coupled to quantum dots.* Nature **450**(7168), 402 (2007).

[25] A. Tsumura, H. Koezuka, and T. Ando. *Macromolecular electronic device: Field-effect transistor with a polythiophene thin film.* Applied Physics Letters **49**(18), 1210 (1986).

[26] H. Koezuka, A. Tsumura, and T. Ando. *Field-effect transistor with polythiophene thin film.* Synthetic Metals **18**(1-3), 699 (1987).

[27] A. Tsumura, H. Koezuka, and T. Ando. *Polythiophene field-effect transistor: Its characteristics and operation mechanism.* Synthetic Metals **25**(1), 11 (1988).

[28] Z. Bao, A. J. Lovinger, and A. Dodabalapur. *Organic field-effect transistors with high mobility based on copper phthalocyanine.* Applied Physics Letters **69**(20), 3066 (1996).

[29] H. Sirringhaus, P. J. Brown, R. H. Friend, M. M. Nielsen, K. Bechgaard, B. M. W. Langeveld-Voss, A. J. H. Spiering, R. A. J. Janssen, E. W. Meijer, P. Herwig, and D. M. de Leeuw. *Two-dimensional charge transport in self-organized, high-mobility conjugated polymers.* Nature **401**(6754), 685 (1999).

[30] C. Dimitrakopoulos and P. Malenfant. *Organic thin film transistors for large area electronics.* Advanced Materials **14**(2), 99 (2002).

[31] M. Halik, H. Klauk, U. Zschieschang, G. Schmid, C. Dehm, M. Schütz, S. Maisch, F. Effenberger, M. Brunnbauer, and F. Stellacci. *Low-voltage organic transistors with an amorphous molecular gate dielectric.* Nature **431**(7011), 963 (2004).

[32] A. C. Arias, J. D. MacKenzie, I. McCulloch, J. Rivnay, and A. Salleo. *Materials and applications for large area electronics: Solution-based approaches.* Chemical Reviews **110**(1), 3 (2010).

[33] B. Sun, W. Hong, Z. Yan, H. Aziz, and Y. Li. *Record High Electron Mobility of 6.3 cm ^{2} V $^{\hat{a}\hat{}'1}$ s $^{\hat{a}\hat{}'1}$ Achieved for Polymer Semiconductors Using a New Building Block.* Advanced Materials **26**(17), 2636 (2014).

[34] T. G. Gopakumar, M. Bernien, H. Naggert, F. Matino, C. F. Hermanns, A. Bannwarth, S. Mühlenberend, A. Krüger, D. Krüger, F. Nickel, W. Walter, R. Berndt, W. Kuch, and F. Tuczek. *Spin-crossover complex on Au(111): Structural and electronic differences between mono- and multilayers.* Chemistry - A European Journal **19**(46), 15702 (2013).

[35] K. S. Chandrasekaran, S. K. Mohanlal, and R. Saravanan. *Charge transfer in the bonding of GaAs.* physica status solidi (b) **196**(1), 3 (1996).

[36] A. R. Lubinsky, C. B. Duke, B. W. Lee, and P. Mark. *Semiconductor surface reconstruction: The rippled geometry of GaAs(110).* Physical Review Letters **36**(17), 1058 (1976).

[37] D. J. Chadi. *(110) surface atomic structures of covalent and ionic semiconductors.* Physical Review B **19**(4), 2074 (1979).

[38] G.-X. Qian, R. M. Martin, and D. J. Chadi. *First-principles calculations of atomic and electronic structure of the GaAs(110) surface.* Physical Review B **37**(3), 1303 (1988).

[39] G. J. de Raad, D. M. Bruls, P. M. Koenraad, and J. H. Wolter. *STM observations of GaAs(110) showing the top and bottom zig-zag rows of the surface.* Physical Review B **64**(7) (2001).

[40] P. E. Gregory. *Surface state band on GaAs (110) face.* Applied Physics Letters **25**(9), 511 (1974).

[41] P. Ebert, B. Engels, P. Richard, K. Schroeder, S. Blügel, C. Domke, M. Heinrich, and K. Urban. *Contribution of surface resonances to scanning tunneling microscopy images: (110) surfaces of III-V semiconductors.* Physical Review Letters **77**(14), 2997 (1996).

[42] S. Sze and J. Irvin. *Resistivity, mobility and impurity levels in GaAs, Ge, and Si at 300°K.* Solid-State Electronics **11**(6), 599 (1968).

[43] R. M. Feenstra. *Electrostatic potential for a hyperbolic probe tip near a semiconductor.* Journal of Vacuum Science & Technology B: Microelectronics and Nanometer Structures **21**(5), 2080 (2003).

[44] R. M. Feenstra, Y. Dong, M. P. Semtsiv, and W. T. Masselink. *Influence of tip-induced band bending on tunnelling spectra of semiconductor surfaces.* Nanotechnology **18**(4), 044015 (2007).

[45] R. M. Feenstra. *SEMITIP, version 6.* `http://www.andrew.cmu.edu/user/feenstra/semitip_v6/`. Accessed: 2015-06-10.

[46] D'yakonov, M.I. and Perel', V.I. *Theory of optical spin orientation of electrons and nuclei in semiconductors.* In *Optical Orientation*, vol. 8 of *Modern Problems in Condensed Matter Sciences*, chap. 2, pp. 11–71 (North-Holland, Amsterdam, 1984).

[47] S. F. Alvarado, P. Renaud, D. L. Abraham, C. Schönenberger, D. J. Arent, and H. P. Meier. *Luminescence in scanning tunneling microscopy on III–V nanostructures.* J. Vac. Sci. Technol. B **9**, 409 (1991).

[48] M. Gouterman. *Optical Spectra and Electronic Structure of Porphyrins and Related Rings in The Porphyrins*, vol. 3, chap. 1, pp. 1–165 (Academic Press, 1978).

[49] A. W. Hains, Z. Liang, M. A. Woodhouse, and B. A. Gregg. *Molecular semiconductors in organic photovoltaic cells.* Chemical Reviews **110**(11), 6689 (2010).

[50] F. H. Moser and A. L. Thomas. *The phthalocyanines* (CRC Press, Boca Raton, Fla, 1983).

[51] C. C. Leznoff and A. B. P. Lever, eds. *Phthalocyanines: properties and applications* (VCH, New York, NY, 1989).

[52] N. B. McKeown. *Phthalocyanine materials: synthesis, structure, and function*. No. 6 in Chemistry of solid state materials (Cambridge University Press, Cambridge, U.K. ; New York, 1998).

[53] R. Christie. *Colour Chemistry*. RSC Paperbacks (Royal Society of Chemistry, Cambridge, 2001).

[54] N. Papageorgiou, E. Salomon, T. Angot, J.-M. Layet, L. Giovanelli, and G. L. Lay. *Physics of ultra-thin phthalocyanine films on semiconductors*. Progress in Surface Science **77**(5-8), 139 (2004).

[55] K. M. Kadish, K. M. Smith, and R. Guilard, eds. *The porphyrin handbook*, vol. 3 (Academic Press, San Diego, 2000).

[56] Y. Wang, K. Wu, J. Kröger, and R. Berndt. *Review article: Structures of phthalocyanine molecules on surfaces studied by STM*. AIP Advances **2**(4), 041402 (2012).

[57] D. Wöhrle, G. Schnurpfeil, S. G. Makarov, A. Kazarin, and O. N. Suvorova. *Practical applications of phthalocyanines–from dyes and pigments to materials for optical, electronic and photo-electronic devices*. Macroheterocycles **5**, 191 (2012).

[58] G. Binnig, H. Rohrer, C. Gerber, and E. Weibel. *Surface studies by scanning tunneling microscopy*. Physical Review Letters **49**(1), 57 (1982).

[59] G. Binnig, H. Rohrer, C. Gerber, and E. Weibel. 7×7 *reconstruction on Si(111) resolved in real space*. Physical Review Letters **50**(2), 120 (1983).

[60] G. Binnig and H. Rohrer. *Scanning tunneling microscopy - from birth to adolescence*. Reviews of Modern Physics **59**(3), 615 (1987).

[61] G. Wentzel. *Eine Verallgemeinerung der Quantenbedingungen für die Zwecke der Wellenmechanik*. Zeitschrift für Physik **38**(6-7), 518 (1926).

[62] H. A. Kramers. *Wellenmechanik und halbzahlige Quantisierung*. Zeitschrift für Physik **39**(10-11), 828 (1926).

[63] L. Brillouin. *La mécanique ondulatoire de Schrödinger; une méthode générale de résolution par approximations successives*. CR Acad. Sci **183**(11), 24 (1926).

[64] J. G. Simmons. *Generalized formula for the electric tunnel effect between similar electrodes separated by a thin insulating film*. Journal of Applied Physics **34**(6), 1793 (1963).

[65] J. Tersoff and D. R. Hamann. *Theory and application for the scanning tunneling microscope*. Physical Review Letters **50**(25), 1998 (1983).

[66] J. Bardeen. *Tunnelling from a many-particle point of view.* Physical Review Letters **6**(2), 57 (1961).

[67] C. J. Chen. *Introduction to Scanning Tunneling Microscopy* (Oxford University Press, 2007).

[68] R. Pérez, M. C. Payne, I. Štich, and K. Terakura. *Role of covalent tip-surface interactions in noncontact atomic force microscopy on reactive surfaces.* Physical Review Letters **78**(4), 678 (1997).

[69] W. Sacks. *Tip orbitals and the atomic corrugation of metal surfaces in scanning tunneling microscopy.* Physical Review B **61**(11), 7656 (2000).

[70] W. A. Hofer, J. Redinger, and R. Podloucky. *Modeling STM tips by single absorbed atoms on W(100) films: 3d and 4d transition-metal atoms.* Physical Review B **64**(12) (2001).

[71] R. Hamers. *STM on semiconductors.* In *Scanning Tunneling Microscopy I*, chap. 5, pp. 83–129 (Springer, 1994).

[72] J. P. Rabe and S. Buchholz. *Direct observation of molecular structure and dynamics at the interface between a solid wall and an organic solution by scanning tunneling microscopy.* Physical Review Letters **66**(16), 2096 (1991).

[73] C. Ludwig, B. Gompf, W. Glatz, J. Petersen, W. Eisenmenger, M. Möbus, U. Zimmermann, and N. Karl. *Video-STM, LEED and X-ray diffraction investigations of PTCDA on graphite.* Zeitschrift fi¿½r Physik B Condensed Matter **86**(3), 397 (1992).

[74] A. Baratoff, G. Binnig, H. Fuchs, F. Salvan, and E. Stoll. *Tunneling microscopy and spectroscopy of semiconductor surfaces and interfaces.* Surface Science **168**(1-3), 734 (1986).

[75] A. Baratoff, G. Binnig, H. Fuchs, H. Rohrer, E. Stoll, and F. Salvan. *Interpretation of scanning tunneling spectroscopic (STS) images–applications to 7 x 7 Si (111).* In *Europhys. Conf Abstr. B*, vol. 10, pp. 0–31 (1986).

[76] R. Feenstra, J. A. Stroscio, and A. Fein. *Tunneling spectroscopy of the Si(111)*2×1 *surface.* Surface Science **181**(1-2), 295 (1987).

[77] J. A. Stroscio. *Imaging electronic surface states in real space on the Si(111)* 2×1 *surface.* Journal of Vacuum Science & Technology A: Vacuum, Surfaces, and Films **5**(4), 838 (1987).

[78] R. M. Feenstra. *Tunneling spectroscopy of the GaAs(110) surface.* Journal of Vacuum Science & Technology B: Microelectronics and Nanometer Structures **5**(4), 923 (1987).

[79] B. C. Stipe. *Single-molecule vibrational spectroscopy and microscopy.* Science **280**(5370), 1732 (1998).

[80] L. Meade. *Lock-in Amplifiers: Principles and Applications.* IEE electrical measurement series (P. Peregrinus, 1983).

[81] J. Klein, A. Léger, M. Belin, D. Défourneau, and M. J. L. Sangster. *Inelastic-electron-tunneling spectroscopy of metal-insulator-metal junctions.* Physical Review B **7**(6), 2336 (1973).

[82] M. F. Crommie, C. P. Lutz, and D. M. Eigler. *Imaging standing waves in a two-dimensional electron gas.* Nature **363**(6429), 524 (1993).

[83] J. A. Kubby. *Imaging extrinsic defects at the $NiSi_2$/Si(111) metal-semiconductor interface.* Journal of Vacuum Science & Technology A: Vacuum, Surfaces, and Films **12**(4), 2009 (1994).

[84] G. V. Nazin. *Visualization and spectroscopy of a metal-molecule-metal bridge.* Science **302**(5642), 77 (2003).

[85] C. Krull, R. Robles, A. Mugarza, and P. Gambardella. *Site- and orbital-dependent charge donation and spin manipulation in electron-doped metal phthalocyanines.* Nature Materials **12**(4), 337 (2013).

[86] S. J. Altenburg, M. Lattelais, B. Wang, M.-L. Bocquet, and R. Berndt. *Reaction of phthalocyanines with graphene on Ir(111).* Journal of the American Chemical Society **137**(29), 9452 (2015).

[87] Y. Hasegawa and P. Avouris. *Direct observation of standing wave formation at surface steps using scanning tunneling spectroscopy.* Physical Review Letters **71**(7), 1071 (1993).

[88] E. J. Heller, M. F. Crommie, C. P. Lutz, and D. M. Eigler. *Scattering and absorption of surface electron waves in quantum corrals.* Nature **369**(6480), 464 (1994).

[89] J. Li, W.-D. Schneider, and R. Berndt. *Local density of states from spectroscopic scanning-tunneling-microscope images: Ag(111).* Physical Review B **56**(12), 7656 (1997).

[90] J. K. Gimzewski, B. Reihl, J. H. Coombs, and R. R. Schlittler. *Photon emission with the scanning tunneling microscope.* Z. Phys. B: Condens. Matter **72**, 497 (1988).

[91] J. H. Coombs, J. K. Gimzewski, B. Reihl, J. K. Sass, and R. R. Schlittler. *Photon emission experiments with the scanning tunnelling microscope.* Journal of Microscopy **152**(2), 325 (1988).

[92] R. Berndt. *Photon emission scanning tunneling microscope.* Journal of Vacuum Science & Technology B: Microelectronics and Nanometer Structures **9**(2), 573 (1991).

[93] J. K. Gimzewski, J. K. Sass, R. R. Schlitter, and J. Schott. *Enhanced photon emission in scanning tunnelling microscopy.* Europhys. Lett. **8**(5), 435 (1989).

[94] R. Berndt and J. K. Gimzewski. *Injection luminescence from CdS*$(11\bar{2}0)$ *studied with scanning tunneling microscopy.* Physical Review B **45**(24), 14095 (1992).

[95] D. L. Abraham, A. Veider, C. Schönenberger, H. P. Meier, D. J. Arent, and S. F. Alvarado. *Nanometer resolution in luminescence microscopy of III-V heterostructures.* Applied Physics Letters **56**(16), 1564 (1990).

[96] R. Berndt, R. Gaisch, W. D. Schneider, J. K. Gimzewski, B. Reihl, R. R. Schlittler, and M. Tschudy. *Photon emission from adsorbed C_{60} molecules with subnanometer lateral resolution.* Applied Physics A Solids and Surfaces **57**(6), 513 (1993).

[97] R. Berndt, J. Gimzewski, and R. Schlittler. *Photon emission from nanostructures in an STM.* Nanostructured Materials **3**(1-6), 345 (1993).

[98] R. Berndt and J. K. Gimzewski. *Photon emission in scanning tunneling microscopy: Interpretation of photon maps of metallic systems.* Physical Review B **48**(7), 4746 (1993).

[99] R. Berndt, J. K. Gimzewski, and R. R. Schlittler. *Photon emission from small particles in an STM.* Zeitschrift für Physik D Atoms, Molecules and Clusters **26**(S1), 87 (1993).

[100] P. Johansson, R. Monreal, and P. Apell. *Theory for light emission from a scanning tunneling microscope.* Phys. Rev. B **42**, 9210 (1990).

[101] B. N. J. Persson and A. Baratoff. *Theory of photon emission in electron tunneling to metallic particles.* Physical Review Letters **68**(21), 3224 (1992).

[102] P. Johansson. *Light emission from a scanning tunneling microscope: Fully retarded calculation.* Physical Review B **58**(16), 10823 (1998).

[103] A. Sommerfeld. *Zur Elektronentheorie der Metalle auf Grund der Fermischen Statistik: I. Teil: Allgemeines, Strömungs- und Austrittsvorgänge.* Zeitschrift für Physik **47**(1-2), 1 (1928).

[104] P. Debye and A. Sommerfeld. *Theorie des lichtelektrischen Effektes vom Standpunkt des Wirkungsquantums.* Annalen der Physik **41**(10), 873 (1913).

[105] R. Berndt, J. K. Gimzewski, and P. Johansson. *Inelastic tunneling excitation of tip-induced plasmon modes on noble-metal surfaces.* Phys. Rev. Lett. **67**(27), 3796 (1991).

[106] M. Chung, T. Callcott, E. Kretschmann, and E. Arakawa. *Radiation from silver films bombarded by low-energy electrons.* Surface Science **91**(1), 245 (1980).

[107] B. Reihl, J. Coombs, and J. Gimzewski. *Local inverse photoemission with the scanning tunneling microscope.* Surface Science **211-212**, 156 (1989).

[108] G. Hoffmann, R. Berndt, and P. Johansson. *Two-electron photon emission from metallic quantum wells.* Physical Review Letters **90**(4) (2003).

[109] R. Berndt and J. K. Gimzewski. *Isochromat spectroscopy of photons emitted from metal surfaces in an STM.* Ann.Physik **505**(2), 133 (1993).

[110] D. E. Hill. *Internal quantum efficiency of GaAs electroluminescent diodes.* Journal of Applied Physics **36**(11), 3405 (1965).

[111] R. J. Nelson and R. G. Sobers. *Minority-carrier lifetimes and internal quantum efficiency of surface-free GaAs.* Journal of Applied Physics **49**(12), 6103 (1978).

[112] M. Kemerink, K. Sauthoff, P. M. Koenraad, J. W. Gerritsen, H. van Kempen, and J. H. Wolter. *Optical detection of ballistic electrons injected by a scanning-tunneling microscope.* Phys. Rev. Lett. **86**, 2404 (2001).

[113] R. Brander. *A review of the merits of direct and indirect gap semiconductors for electroluminescence devices.* Reviews of Physics in Technology **3**(3), 145 (1972).

[114] T. Maruyama, E. L. Garwin, R. Prepost, and G. H. Zapalac. *Electron-spin polarization in photoemission from strained GaAs grown on* $GaAs_{1-x}P_x$. Phys. Rev. B **46**, 4261 (1992).

[115] R. N. Bhargava and M. I. Nathan. *Stress dependence of photoluminescence in GaAs.* Phys. Rev. **161**(3), 695 (1967).

[116] F. H. Pollak, M. Cardona, and K. L. Shaklee. *Piezoelectroreflectance in GaAs.* Phys. Rev. Lett. **16**(21), 942 (1966).

[117] B. T. Jonker, Y. D. Park, B. R. Bennett, H. D. Cheong, G. Kioseoglou, and A. Petrou. *Robust electrical spin injection into a semiconductor heterostructure.* Phys. Rev. B **62**, 8180 (2000).

[118] J. I. Pankove. *Absorption edge of impure gallium arsenide.* Phys. Rev. **140**, A2059 (1965).

[119] P. M. Krstajić, F. M. Peeters, V. A. Ivanov, V. Fleurov, and K. Kikoin. *Double-exchange mechanisms for Mn-doped III-V ferromagnetic semiconductors.* Phys. Rev. B **70**, 195215 (2004).

[120] T. Jungwirth, J. Sinova, A. H. MacDonald, B. L. Gallagher, V. Novák, K. W. Edmonds, A. W. Rushforth, R. P. Campion, C. T. Foxon, L. Eaves, J. Olejnsek, S. R. E. Yang, J. Wunderlich, C. Gould, L. W. Molenkamp, T. Dietl, and H. Ohno. *Character of states near the fermi level in (Ga,Mn)As: Impurity to valence band crossover.* Phys. Rev. B **76**, 125206 (2007).

[121] O. Yastrubchak, J. Zuk, H. Krzyzzanowska, J. Z. Domagala, T. Andrearczyk, J. Sadowski, and T. Wosinski. *Photoreflectance study of the fundamental optical properties of (Ga,Mn)As epitaxial films.* Phys. Rev. B **83**, 245201 (2011).

[122] G. Borghs, K. Bhattacharyya, K. Deneffe, P. Van Mieghem, and R. Mertens. *Band-gap narrowing in highly doped n- and p-type GaAs studied by photoluminescence spectroscopy.* J. Appl. Phys. **66**(9), 4381 (1989).

[123] R. Berndt, R. Gaisch, J. K. Gimzewski, B. Reihl, R. R. Schlittler, W. D. Schneider, and M. Tschudy. *Photon emission at molecular resolution induced by a scanning tunneling microscope.* Science **262**(5138), 1425 (1993).

[124] D. Fujita, T. Ohgi, W.-L. Deng, H. Nejo, T. Okamoto, S. Yokoyama, K. Kamikado, and S. Mashiko. *STM induced photon emission from adsorbed porphyrin molecules on a Cu(100) surface in ultrahigh vacuum.* Surf. Sci. **454-456**, 1021 (2000).

[125] P. Avouris and B. N. J. Persson. *Excited states at metal surfaces and their nonradiative relaxation.* The Journal of Physical Chemistry **88**(5), 837 (1984).

[126] D. Waldeck, A. Alivisatos, and C. Harris. *Nonradiative damping of molecular electronic excited states by metal surfaces.* Surface Science **158**(1-3), 103 (1985).

[127] Z.-C. Dong, A. Trifonov, X.-L. Guo, K. Amemiya, S. Yokoyama, T. Kamikado, T. Yamada, S. Mashiko, and T. Okamoto. *Tunneling electron induced photon emission from monolayered H_2TBP porphyrin molecules on Cu(100).* Surface Science **532-535**, 237 (2003).

[128] Z.-C. Dong, X.-L. Guo, A. S. Trifonov, P. S. Dorozhkin, K. Miki, K. Kimura, S. Yokoyama, and S. Mashiko. *Vibrationally resolved fluorescence from organic molecules near metal surfaces in a scanning tunneling microscope.* Phys. Rev. Lett. **92**, 086801 (2004).

[129] H. W. Liu, Y. Ie, R. Nishitani, Y. Aso, and H. Iwasaki. *Bias dependence of tunneling-electron-induced molecular fluorescence from porphyrin films on noble-metal substrates.* Phys. Rev. B **75**(11), 115429 (2007).

[130] Z.-C. Dong, X. L. Zhang, H. Y. Gao, Y. Luo, C. Zhang, L. G. Chen, R. Zhang, X. Tao, Y. Zhang, J. L. Yang, and J. G. Hou. *Generation of molecular hot electroluminescence by resonant nanocavity plasmons.* Nat. Photonics **4**, 50 (2010).

[131] X. H. Qiu, G. V. Nazin, and W. Ho. *Vibrationally resolved fluorescence excited with submolecular precision.* Science **299**(5606), 542 (2003).

[132] E. Cavar, M.-C. Blüm, M. Pivetta, F. Patthey, M. Chergui, and W.-D. Schneider. *Fluorescence and phosphorescence from individual C_{60} molecules excited by local electron tunneling.* Phys. Rev. Lett. **95**(19), 196102 (2005).

[133] G. Hoffmann, L. Libioulle, and R. Berndt. *Tunneling-induced luminescence from adsorbed organic molecules with submolecular lateral resolution.* Physical Review B **65**(21) (2002).

[134] T. Uemura, M. Furumoto, T. Nakano, M. Akai-Kasaya, A. Saito, M. Aono, and Y. Kuwahara. *Local-plasmon-enhanced up-conversion fluorescence from copper phthalocyanine.* Chem. Phys. Lett. **448**(4-6), 232 (2007).

[135] H. W. Liu, R. Nishitani, T. Z. Han, Y. Ie, Y. Aso, and H. Iwasaki. *STM fluorescence of porphyrin enhanced by a strong plasmonic field and its nanoscale confinement in an STM cavity.* Physical Review B **79**(12) (2009).

[136] F. Rossel, M. Pivetta, F. Patthey, and W.-D. Schneider. *Plasmon enhanced luminescence from fullerene molecules excited by local electron tunneling.* Optics Express **17**(4), 2714 (2009).

[137] A. Kabakchiev, K. Kuhnke, T. Lutz, and K. Kern. *Electroluminescence from individual pentacene nanocrystals.* ChemPhysChem **11**(16), 3412 (2010).

[138] N. L. Schneider, F. Matino, G. Schull, S. Gabutti, M. Mayor, and R. Berndt. *Light emission from a double-decker molecule on a metal surface.* Physical Review B **84**(15) (2011).

[139] C. Zhang, R. Zhang, S. Jiang, L. Zhang, H. Y. Gao, X. L. Zhang, L. G. Chen, Y. Liao, and Z. C. Dong. *Tip-plasmon mediated molecular electroluminescence on the highly oriented pyrolytic graphite substrate.* Appl. Phys. Lett. **100**(7), 073111 (pages 4) (2012).

[140] S. Mühlenberend, N. L. Schneider, M. Gruyters, and R. Berndt. *Plasmon-induced fluorescence and electroluminescence from porphine molecules on GaAs(110) in a scanning tunneling microscope.* Applied Physics Letters **101**(20), 203107 (2012).

[141] D. Olego and M. Cardona. *Raman scattering by coupled lo-phononplasmon modes and forbidden to-phonon raman scattering in heavily doped p-type GaAs.* Phys. Rev. B **24**, 7217 (1981).

[142] M. Hollis, S. Palmateer, L. Eastman, N. Dandekar, and P. Smith. *Importance of electron scattering with coupled plasmon-optical phonon modes in GaAs planar-doped barrier transistors.* Electron Device Letters, IEEE **4**(12), 440 (1983).

[143] R. Fukasawa and S. Perkowitz. *Raman-scattering spectra of coupled lo-phonon hole-plasmon modes in p -type GaAs.* Phys. Rev. B **50**, 14119 (1994).

[144] Kliewer, Jörg Uwe. *Dynamics and Manipulation of Surfaces States.* Ph.D. thesis, RWTH Aachen, Aachen (2000).

[145] T. Jürgens. *Aufbau und Test eines Raumtemperatur-Ultrahochvakuum-Rastertunnelmikroskops.* Ph.D. thesis, Christian-Albrechts-Universität zu Kiel, Institut für Experimentelle und Angewandte Physik (2003).

[146] G. Hoffmann. *Light Emission from Metals and Adsorbates in the Scanning Tunneling Microscope.* Ph.D. thesis, Christian-Albrechts-Universität zu Kiel, Institut für Experimentelle und Angewandte Physik (2001).

[147] J. A. Stroscio and W. J. Kaiser. *Scanning tunneling microscopy* (Academic Press, Boston, 1993).

[148] R. Wiesendanger. *Scanning probe microscopy and spectroscopy: methods and applications* (Cambridge University Press, Cambridge [England] ; New York, 1994).

[149] Güntherodt, H.-J. and Wiesendanger, R. *Scanning Tunneling Microscopy I General Principles and Applications to Clean and Absorbate-Covered Surfaces* (Springer Berlin Heidelberg, Berlin, Heidelberg, 1994).

[150] M. Bowker, P. R. Davies, and Wiley InterScience (Online service). *Scanning tunneling microscopy in surface science* (Wiley-VCH ; John Wiley [distributor], Weinheim; Chichester, 2009).

[151] R. Gaisch, J. Gimzewski, B. Reihl, R. Schlittler, M. Tschudy, and W. Schneider. *Low-temperature ultra-high-vacuum scanning tunneling microscope.* Ultramicroscopy **42-44**, 1621 (1992).

[152] R. Gaisch. *Scanning Tunneling Microscopy in Ultra High Vacuum at Low Temperatures.* Ph.D. thesis, Université de Lausanne, Faculté des Sciences (1994).

[153] G. Hoffmann, J. Kröger, and R. Berndt. *Color imaging with a low temperature scanning tunneling microscope.* Rev. Sci. Instrum. **73**, 305 (2002).

[154] S. Mühlenberend. *Entwicklung einer Polarisationsanalyse für die STM-induzierte Lichtemission.* Diploma thesis, Mathematisch-Naturwissenschaftliche Fakultät der Christian-Albrechts-Universität zu Kiel (2010).

[155] E. Ozbay. *Plasmonics: Merging photonics and electronics at nanoscale dimensions.* Science **311**(5758), 189 (2006).

[156] H. Kuhn. *Versuche zur Herstellung einfacher organisierter Systeme von Molekülen.* Pure Appl. Chem. **11**, 345 (1965).

[157] K.-H. Drexhage. *Interaction of light with monomolecular dye layers.* Prog. Optics **12**, 163 (1974).

[158] P. Johansson, H. Xu, and M. Käll. *Surface-enhanced raman scattering and fluorescence near metal nanoparticles.* Phys. Rev. B **72**, 035427 (2005).

[159] H. Morawitz and M. R. Philpott. *Coupling of an excited molecule to surface plasmons.* Phys. Rev. B **10**, 4863 (1974).

[160] B. Rothenhausler and W. Knoll. *Surface-plasmon microscopy.* Nature **332**(6165), 615 (1988).

[161] A. Ishida and T. Majima. *Surface plasmon excitation of porphyrin self-assembly monolayers on an Au surface.* Nanotech. **10**(3), 308 (1999).

[162] A. A. Toropov, T. V. Shubina, V. N. Jmerik, S. V. Ivanov, Y. Ogawa, and F. Minami. *Optically enhanced emission of localized excitons in $In_xGa_{1-x}N$ films by coupling to plasmons in a gold nanoparticle.* Phys. Rev. Lett. **103**, 037403 (2009).

[163] E. Rabinowitch. *Spectra of porphyrins and chlorophyll.* Rev. Mod. Phys. **16**, 226 (1944).

[164] M. Reinhardt, G. Schull, P. Ebert, and R. Berndt. *Atomic resolution in tunneling induced light emission from GaAs(110).* Appl. Phys. Lett. **96**, 152107 (2010).

[165] D. Fujita, K. Onishi, and N. Niori. *Light emission induced by tunnelling electrons from a p-type GaAs(110) surface observed at near-field by a conductive optical fibre probe.* Nanotech. **15**(6), S355 (2004).

[166] T. Yokoyama and Y. Takiguchi. *Scanning tunneling microscope induced light emission from GaAs(110) surfaces.* Surf. Sci. **482-485**, 1163 (2001).

[167] E. Anisimovas and P. Johansson. *Tip-geometry effects in circularly polarized light emission from a scanning tunneling microscope.* Phys. Rev. B **59**, 5126 (1999).

[168] A. L. V. d. Parga and S. F. Alvarado. *Circular dichroism in STM-excited luminescence on metals.* Europhys. Lett. **36**(8), 577 (1996).

[169] D. Pierce, A. Davies, J. Stroscio, and R. Celotta. *Polarized light emission from the metal-metal STM junction.* Appl. Phys. A **66**, S403 (1998).

[170] W. Lukosz. *Light emission by magnetic and electric dipoles close to a plane dielectric interface. III. radiation patterns of dipoles with arbitrary orientation.* J. Opt. Soc. Am. **69**(11), 1495 (1979).

[171] X.-L. Guo, Z.-C. Dong, A. S. Trifonov, K. Miki, Y. Wakayama, D. Fujita, K. Kimura, S. Yokoyama, and S. Mashiko. *Nanoscale organic electroluminescence from tunnel junctions.* Phys. Rev. B **70**, 233204 (2004).

[172] G. Tian, J.-C. Liu, and Y. Luo. *Density-matrix approach for the electroluminescence of molecules in a scanning tunneling microscope.* Phys. Rev. Lett. **106**, 177401 (2011).

[173] R. Berndt, A. Baratoff, and J. K. Gimzewski. *Scanning Tunneling Microscopy and Related Methods*, chap. Scanning tunneling optical microscopy (STOM) of silver nanostructures, pp. 269–280 (Behm, R.J. and Garcia, N. and Rohrer, H., 1990).

[174] The generation of molecular fluorescence at negative sample voltage via hot holes would require an Auger-type process to promote a valence band electron to the LUMO along with the injection of a hole to the HOMO. Such a mechanism is unlikely.

[175] S. Mühlenberend, M. Gruyters, and R. Berndt. *Plasmon-mediated circularly polarized luminescence of GaAs in a scanning tunneling microscope.* Applied Physics Letters **107**(24), 241110 (2015).

[176] M. N. Baibich, J. M. Broto, A. Fert, F. N. Van Dau, F. Petroff, P. Etienne, G. Creuzet, A. Friederich, and J. Chazelas. *Giant magnetoresistance of (001)Fe/(001)Cr magnetic superlattices.* Physical Review Letters **61**(21), 2472 (1988).

[177] G. Binasch, P. Grünberg, F. Saurenbach, and W. Zinn. *Enhanced magnetoresistance in layered magnetic structures with antiferromagnetic interlayer exchange.* Physical Review B **39**(7), 4828 (1989).

[178] Ching Tsang, R. Fontana, Tsann Lin, D. Heim, V. Speriosu, B. Gurney, and M. Williams. *Design, fabrication and testing of spin-valve read heads for high density recording.* IEEE Transactions on Magnetics **30**(6), 3801 (1994).

[179] H. Kanai, K. Yamada, K. Aoshima, Y. Ohtsuka, J. Kane, M. Kanamine, J. Toda, and Y. Mizoshita. *Spin-valve read heads with $NiFe/Co_{90}Fe_{10}$ layers for 5 Gbit/in^2 density recording.* IEEE Transactions on Magnetics **32**(5), 3368 (1996).

[180] H. Yoda, H. Iwasaki, T. Kobayashi, A. Tsutai, and M. Sahashi. *Dual-element GMR/inductive heads for gigabits density recording using CoFe spin-valves.* IEEE Transactions on Magnetics **32**(5), 3363 (1996).

[181] Parkin, S.S.P. *Applications of magnetic nanostructures.* In *Spin Dependent Transport in Magnetic Nanostructures*, pp. 237–279 (Taylor & Francis, London, 2002).

[182] C. Chappert, A. Fert, and F. N. Van Dau. *The emergence of spin electronics in data storage.* Nature Materials **6**(11), 813 (2007).

[183] X. Jiang, R. Wang, R. M. Shelby, R. M. Macfarlane, S. R. Bank, J. S. Harris, and S. S. P. Parkin. *Highly spin-polarized room-temperature tunnel injector for semiconductor spintronics using MgO(100).* Phys. Rev. Lett. **94**, 056601 (2005).

[184] Y. Ohno, D. K. Young, B. Beschoten, F. Matsukura, H. Ohno, and D. D. Awschalom. *Electrical spin injection in a ferromagnetic semiconductor heterostructure.* Nature **402**, 790 (1999).

[185] R. Fiederling, M. Keim, G. Reuscher, W. Ossau, G. Schmidt, A. Waag, and L. W. Molenkamp. *Injection and detection of a spin-polarized current in a light-emitting diode.* Nature **402**, 787 (1999).

[186] C. Adelmann, X. Lou, J. Strand, C. J. Palmstrom, and P. A. Crowell. *Spin injection and relaxation in ferromagnet-semiconductor heterostructures.* Phys. Rev. B **71**, 121301 (2005).

[187] O. M. J. van't Erve, G. Kioseoglou, A. T. Hanbicki, C. H. Li, and B. T. Jonker. *Remanent electrical spin injection from Fe into light emitting diodes.* Appl. Phys. Lett. **89**, 072505 (2006).

[188] M. C. Hickey, S. N. Holmes, T. Meng, I. Farrer, G. A. C. Jones, D. A. Ritchie, and M. Pepper. *Strongly bias-dependent spin injection from Fe into n-type GaAs.* Phys. Rev. B **75**, 193204 (2007).

[189] J. Zarpellon, H. Jaffrès, J. Frougier, C. Deranlot, J. M. George, D. H. Mosca, A. Lemaître, F. Freimuth, Q. H. Dong, P. Renucci, and X. Marie. *Spin injection at remanence into III-V spin light-emitting diodes using (Co/Pt) ferromagnetic injectors.* Phys. Rev. B **86**, 205314 (2012).

[190] S. Hershfield and H. L. Zhao. *Charge and spin transport through a metallic ferromagnetic-paramagnetic-ferromagnetic junction.* Phys. Rev. B **56**(6), 3296 (1997).

[191] E. Rashba. *Diffusion theory of spin injection through resistive contacts.* Eur. Phys. J. B **29**(4), 513 (2002).

[192] A. Fert and H. Jaffrès. *Conditions for efficient spin injection from a ferromagnetic metal into a semiconductor.* Phys. Rev. B **64**(18) (2001).

[193] C. Schönenberger and S. F. Alvarado. *Understanding magnetic force microscopy.* Z. Phys. B: Condens. Matter **80**, 373 (1990).

[194] W. Eib and S. F. Alvarado. *Spin-polarized photoelectrons from nickel single crystals.* Phys. Rev. Lett. **37**(7), 444 (1976).

[195] M. Landolt and M. Campagna. *Spin polarization of field-emitted electrons and magnetism at the (100) surface of Ni.* Phys. Rev. Lett. **38**(12), 663 (1977).

[196] E. Kisker, W. Gudat, E. Kuhlmann, R. Clauberg, and M. Campagna. *Observation of —100% spin-polarized photoelectrons from a transversely magnetized Ni(110) single crystal.* Physical Review Letters **45**(25), 2053 (1980).

[197] C. Rau and S. Eichner. *Electron-spin polarization at single-crystalline Cr and Ni surfaces determined with electron-capture spectroscopy.* Phys. Rev. Lett. **47**(13), 939 (1981).

[198] A. Schlenhoff, S. Krause, G. Herzog, and R. Wiesendanger. *Bulk Cr tips with full spatial magnetic sensitivity for spin-polarized scanning tunneling microscopy.* Appl. Phys. Lett. **97**(8), 083104 (2010).

[199] S. Loth, M. Wenderoth, and R. G. Ulbrich. *Asymmetry of acceptor wave functions caused by surface-related strain and electric field in InAs.* Phys. Rev. B **77**(11) (2008).

[200] M. L. Lovejoy, M. R. Melloch, and M. S. Lundstrom. *Temperature dependence of minority and majority carrier mobilities in degenerately doped GaAs.* Appl. Phys. Lett. **67**(8), 1101 (1995).

[201] T. Kaneto, K. W. Kim, and M. A. Littlejohn. *A comparison of minority electron transport in $In_{0.53}Ga_{0.47}As$ and GaAs.* Applied Physics Letters **63**(1), 48 (1993).

[202] Y. Varshni. *Temperature dependence of the energy gap in semiconductors.* Physica **34**(1), 149 (1967).

[203] D. Olego and M. Cardona. *Photoluminescence in heavily doped GaAs. i. temperature and hole-concentration dependence.* Phys. Rev. B **22**, 886 (1980).

[204] J. S. Lee, I. Kim, B. D. Choe, W. G. Jeong, Y. K. Sin, and W. S. Min. *Luminescence properties of heavily carbon doped GaAs.* J. Appl. Phys. **79**, 9278 (1996).

[205] M. K. Hudait, P. Modak, S. Hardikar, and S. B. Krupanidhi. *Zn incorporation and band gap shrinkage in p-type GaAs.* J. Appl. Phys. **82**, 4931 (1997).

[206] Y. Uehara, H. Gotoh, R. Arafune, and S. Ushioda. *Electromagnetic enhancement effect in scanning tunneling microscope light emission from GaAs.* J. Appl. Phys. **93**(7), 3784 (2003).

[207] P. M. Tedrow and R. Meservey. *Spin-dependent tunneling into ferromagnetic nickel.* Phys. Rev. Lett. **26**(4), 192 (1971).

[208] P. M. Tedrow and R. Meservey. *Spin polarization of electrons tunneling from films of Fe, Co, Ni, and Gd.* Physical Review B **7**(1), 318 (1973).

[209] A. T. Hanbicki, B. T. Jonker, G. Itskos, G. Kioseoglou, and A. Petrou. *Efficient electrical spin injection from a magnetic metal/tunnel barrier contact into a semiconductor.* Applied Physics Letters **80**(7), 1240 (2002).

[210] A. T. Hanbicki, O. M. J. van 't Erve, R. Magno, G. Kioseoglou, C. H. Li, B. T. Jonker, G. Itskos, R. Mallory, M. Yasar, and A. Petrou. *Analysis of the transport process providing spin injection through an Fe/AlGaAs Schottky barrier.* Applied Physics Letters **82**(23), 4092 (2003).

[211] P. Van Dorpe, W. Van Roy, V. F. Motsny, G. Borghs, and J. De Boeck. *Efficient electrical spin injection in GaAs: A comparison between AlOx and Schottky injectors.* Journal of Vacuum Science & Technology A: Vacuum, Surfaces, and Films **22**(4), 1862 (2004).

[212] G. E. Pikus and A. N. Titkov. *Optical Orientation* (North-Holland, Amsterdam, 1984).

[213] G. Fishman and G. Lampel. *Spin relaxation of photoelectrons in p-type gallium arsenide.* Phys. Rev. B **16**, 820 (1977).

[214] G. Fishman and C. Hermann. *Optical pumping and transverse magnetic field effect for excitation above the band edge in p-type semiconductors.* physica status solidi (b) **63**(1), 307 (1974).

[215] H. C. Casey. *Concentration-dependent absorption and spontaneous emission of heavily doped GaAs.* J. Appl. Phys. **47**(2), 631 (1976).

[216] Garwin,E.L., Pierce, D.T., and Siegmann, H.C. *Polarized photoelectrons from optically magnetized semiconductors.* Tech. rep., Technical report, Stanford Research Inst., Menlo Park, CA (USA) (1975).

[217] Zakharchenya B.I., Fleisher V. G., Dzhioev R. I., Veshchunov Yu. P., and Rusanov I.B. *Effect of optical orientation of electron spins in a GaAs crystal.* JETP Lett. **13**(4), 137 (1971).

[218] Ekimov A . I . and Safarov V.I. *Influence of spin relaxation of "hot" electrons in the effectiveness of optical orientationin semiconductors.* JETP Lett. **13**(12), 495 (1971).

[219] M. Julliere. *Tunneling between ferromagnetic films.* Phys. Lett. A **54**(3), 225 (1975).

[220] R. Wiesendanger, H.-J. Güntherodt, G. Güntherodt, R. J. Gambino, and R. Ruf. *Observation of vacuum tunneling of spin-polarized electrons with the scanning tunneling microscope.* Phys. Rev. Lett. **65**(2), 247 (1990).

[221] R. Wiesendanger, H. J. Günterodt, G. Güntherodt, R. J. Gambino, and R. Ruf. *Scanning tunneling microscopy with spin-polarized electrons.* Z. Phys. B: Condens. Matter **80**(1), 5 (1990).

[222] M. Bode, M. Getzlaff, and R. Wiesendanger. *Spin-polarized vacuum tunneling into the exchange-split surface state of Gd(0001).* Physical Review Letters **81**(19), 4256 (1998).

[223] O. Pietzsch, A. Kubetzka, M. Bode, and R. Wiesendanger. *Real-space observation of dipolar antiferromagnetism in magnetic nanowires by spin-polarized scanning tunneling spectroscopy.* Physical Review Letters **84**(22), 5212 (2000).

[224] S. Heinze. *Real-space imaging of two-dimensional antiferromagnetism on the atomic scale.* Science **288**(5472), 1805 (2000).

[225] R. Wiesendanger and M. Bode. *Nano- and atomic-scale magnetism studied by spin-polarized scanning tunneling microscopy and spectroscopy.* Solid State Communications **119**(4-5), 341 (2001).

[226] P. Bharadwaj, P. Anger, and L. Novotny. *Nanoplasmonic enhancement of single-molecule fluorescence.* Nanotech. **18**(4), 044017 (2007).

[227] N. L. Schneider and R. Berndt. *Plasmonic excitation of light emission and absorption by porphyrine molecules in a scanning tunneling microscope.* Phys. Rev. B **86**, 035445 (2012).

[228] P. Vasa, R. Pomraenke, S. Schwieger, Y. I. Mazur, V. Kunets, P. Srinivasan, E. Johnson, J. E. Kihm, D. S. Kim, E. Runge, G. Salamo, and C. Lienau. *Coherent exciton–surface-plasmon-polariton interaction in hybrid metal-semiconductor nanostructures.* Physical Review Letters **101**(11) (2008).

[229] P. Klaer, F. Schertz, M. Lehr, G. Schönhense, and H. J. Elmers. *Spin-polarized photoelectrons resonantly excited by circularly polarized light from a fractional Ag film on GaAs(100).* Physical Review B **88**(21) (2013).

[230] D. Lynch, R. Rosei, and J. Weaver. *Infrared and visible optical properties of single crystal Ni at 4K.* Solid State Commun. **9**(24), 2195 (1971).

[231] M. A. Ordal, L. L. Long, R. J. Bell, S. E. Bell, R. R. Bell, R. W. Alexander, Jr., and C. A. Ward. *Optical properties of the metals Al, Co, Cu, Au, Fe, Pb, Ni, Pd, Pt, Ag, Ti, and W in the infrared and far infrared.* Appl. Opt. **22**(7), 1099 (1983).

[232] R. Berndt, J. K. Gimzewski, and R. R. Schlittler. *Enhanced photon emission from the STM: a general property of metal surfaces.* Ultramicroscopy **42-44**, 355 (1992).

[233] J. Chen, P. Albella, Z. Pirzadeh, P. Alonso-González, F. Huth, S. Bonetti, V. Bonanni, J. Åkerman, J. Nogués, P. Vavassori, A. Dmitriev, J. Aizpurua, and R. Hillenbrand. *Plasmonic nickel nanoantennas.* Small **7**(16), 2341 (2011).

[234] P. Renaud and S. F. Alvarado. *Mapping quantum-well energy profiles of III-V heterostructures by scanning-tunneling-microscope-excited luminescence.* Physical Review B **44**(12), 6340 (1991).

[235] M. Wenderoth, M. J. Gregor, and R. G. Ulbrich. *Luminescence from gold-passivated gallium arsenide surfaces excited with a scanning tunneling microscope.* Solid State Commun. **83**, 535 (1992).

[236] X. L. Guo, D. Fujita, N. Niori, S. Keisuke, and K. Onishi. *Nanoscale electroluminescence from n-type GaAs(110) in tunnel junctions.* Nanotechnology **18**(19), 195201 (2007).

[237] H. J. Zhu, M. Ramsteiner, H. Kostial, M. Wassermeier, H.-P. Schönherr, and K. H. Ploog. *Room-temperature spin injection from Fe into GaAs.* Physical Review Letters **87**(1) (2001).

[238] H. Ohno, K. Yoh, K. Sueoka, K. Mukasa, A. Kawaharazuka, and M. E. Ramsteiner. *Spin-polarized electron injection through an Fe/InAs junction.* Jap. J. Appl. Phys. **42**(Part 2, No. 2A), L87 (2003).

[239] D. Hägele, M. Oestreich, W. W. Rühle, N. Nestle, and K. Eberl. *Spin transport in GaAs.* Appl. Phys. Lett. **73**(11), 1580 (1998).

[240] R. J. Seymour and R. R. Alfano. *Time-resolved measurement of the electron-spin relaxation kinetics in GaAs.* Appl. Phys. Lett. **37**(2), 231 (1980).

[241] A. Aviram and M. A. Ratner. *Molecular rectifiers.* Chemical Physics Letters **29**(2), 277 (1974).

[242] A. H. Flood. *Chemistry: Enhanced: Whence molecular electronics?* Science **306**(5704), 2055 (2004).

[243] N. S. Hush. *An overview of the first half-century of molecular electronics.* Annals of the New York Academy of Sciences **1006**(1), 1 (2003).

[244] W. Haiss, C. Wang, I. Grace, A. S. Batsanov, D. J. Schiffrin, S. J. Higgins, M. R. Bryce, C. J. Lambert, and R. J. Nichols. *Precision control of single-molecule electrical junctions.* Nature Materials **5**(12), 995 (2006).

[245] J. Repp. *Imaging bond formation between a gold atom and pentacene on an insulating surface.* Science **312**(5777), 1196 (2006).

[246] J. Repp, G. Meyer, S. M. Stojković, A. Gourdon, and C. Joachim. *Molecules on insulating films: Scanning-tunneling microscopy imaging of individual molecular orbitals.* Physical Review Letters **94**(2) (2005).

[247] Y. Wang, J. Kröger, R. Berndt, and W. A. Hofer. *Pushing and pulling a Sn ion through an adsorbed phthalocyanine molecule.* Journal of the American Chemical Society **131**(10), 3639 (2009).

[248] G. Münnich, F. Albrecht, C. Nacci, M. Utz, D. Schuh, K. Kanisawa, S. Fölsch, and J. Repp. *Probing individual weakly-coupled ϕ-conjugated molecules on semiconductor surfaces.* Journal of Applied Physics **112**(3), 034312 (2012).

[249] L. Ramoino, M. von Arx, S. Schintke, A. Baratoff, H.-J. Güntherodt, and T. Jung. *Layer-selective epitaxial self-assembly of porphyrins on ultrathin insulators.* Chemical Physics Letters **417**(1-3), 22 (2006).

[250] C. Bombis, N. Kalashnyk, W. Xu, E. Laegsgaard, F. Besenbacher, and T. R. Linderoth. *Hydrogen-bonded molecular networks of melamine and cyanuric acid on thin films of NaCl on Au(111).* Small **5**(19), 2177 (2009).

[251] Y. Wang, J. Kröger, R. Berndt, and H. Tang. *Molecular nanocrystals on ultrathin NaCl films on Au(111).* Journal of the American Chemical Society **132**(36), 12546 (2010).

[252] Y. Hirose, S. R. Forrest, and A. Kahn. *Quasiepitaxial growth of the organic molecular semiconductor 3,4,9,10-perylenetetracarboxylic dianhydride.* Physical Review B **52**(19), 14040 (1995).

[253] J. Cox, S. Bayliss, and T. Jones. *Ordered copper phthalocyanine overlayers on InAs and InSb (100) surfaces.* Surface Science **433-435**, 152 (1999).

[254] J. Cox and T. Jones. *The structure of copper phthalocyanine and perylene-3,4,9,10-tetracarboxylic dianhydride overlayers on the (111)A surfaces of InAs and InSb.* Surface Science **457**(3), 311 (2000).

[255] L. Giovanelli, H. Von Schenck, M. Sinner-Hettenbach, N. Papageorgiou, M. Göthelid, and G. Le Lay. *Synchrotron radiation photoelectron spectroscopy study of Pb-Pc thin films on InSb(100)-$(4\times2)/c(8\times2)$.* Surface Science **486**(1-2), 55 (2001).

[256] L. Giovanelli, N. Papageorgiou, G. Terzian, J. Layet, J. Mossoyan, M. Mossoyan-Deneux, M. Göthelid, and G. Le Lay. *Electronic structure of self-assembled organic/inorganic semiconductor interfaces: lead phthalocyanine on InSb and InAs(100)–$4 \times 2/c(8 \times 2)$.* Journal of Electron Spectroscopy and Related Phenomena **114-116**, 375 (2001).

[257] A. Tekiel, M. Goryl, and M. Szymonski. *Copper phthalocyanine molecules on an InSb(001) $c(8 \times 2)$ surface studied by ultra-high-vacuum STM and non-contact AFM.* Nanotechnology **18**(47), 475707 (2007).

[258] M. Gruyters, T. Pingel, T. G. Gopakumar, N. Néel, C. Schütt, F. Köhler, R. Herges, and R. Berndt. *Electronic ground-state and orbital ordering of iron phthalocyanine on H/Si(111) unraveled by spatially resolved tunneling spectroscopy.* The Journal of Physical Chemistry C **116**(39), 20882 (2012).

[259] F. Marczinowski, J. Wiebe, F. Meier, K. Hashimoto, and R. Wiesendanger. *Effect of charge manipulation on scanning tunneling spectra of single Mn acceptors in InAs.* Physical Review B **77**(11) (2008).

[260] K. Teichmann, M. Wenderoth, S. Loth, R. Ulbrich, J. Garleff, A. Wijnheijmer, and P. Koenraad. *Controlled charge switching on a single donor with a scanning tunneling microscope.* Physical Review Letters **101**(7) (2008).

[261] A. P. Wijnheijmer, J. K. Garleff, K. Teichmann, M. Wenderoth, S. Loth, and P. M. Koenraad. *Single Si dopants in GaAs studied by scanning tunneling microscopy and spectroscopy.* Physical Review B **84**(12) (2011).

[262] H. Zheng, J. Kröger, and R. Berndt. *Spectroscopy of single donors at ZnO(0001) surfaces.* Physical Review Letters **108**(7) (2012).

[263] N. A. Pradhan, N. Liu, C. Silien, and W. Ho. *Atomic scale conductance induced by single impurity charging.* Physical Review Letters **94**(7) (2005).

[264] G. Nazin, X. Qiu, and W. Ho. *Charging and interaction of individual impurities in a monolayer organic crystal.* Physical Review Letters **95**(16) (2005).

[265] G. Mikaelian, N. Ogawa, X. W. Tu, and W. Ho. *Atomic scale control of single molecule charging.* The Journal of Chemical Physics **124**(13), 131101 (2006).

[266] G. J. de Raad, D. M. Bruls, P. M. Koenraad, and J. H. Wolter. *Interplay between tip-induced band bending and voltage-dependent surface corrugation on GaAs(110) surfaces.* Physical Review B **66**(19) (2002).

[267] S. Loth, M. Wenderoth, R. G. Ulbrich, S. Malzer, and G. H. Döhler. *Connection of anisotropic conductivity to tip-induced space-charge layers in scanning tunneling spectroscopy of p-doped GaAs.* Phys. Rev. B **76**, 235318 (2007).

[268] M. J. Frisch, G. W. Trucks, H. B. Schlegel, G. E. Scuseria, M. A. Robb, J. R. Cheeseman, G. Scalmani, V. Barone, B. Mennucci, G. A. Petersson, H. Nakatsuji, M. Caricato, X. Li, H. P. Hratchian, A. F. Izmaylov, J. Bloino, G. Zheng, J. L. Sonnenberg, M. Hada, M. Ehara, K. Toyota, R. Fukuda, J. Hasegawa, M. Ishida, T. Nakajima, Y. Honda, O. Kitao, H. Nakai, T. Vreven, J. A. Montgomery Jr., J. E. Peralta, F. Ogliaro, M. Bearpark, J. J. Heyd, E. Brothers, K. N. Kudin, V. N. Staroverov, R. Kobayashi, J. Normand, K. Raghavachari, A. Rendell, J. C. Burant, S. S. Iyengar, J. Tomasi, M. Cossi, N. Rega, J. M. Millam, M. Klene, J. E. Knox, J. B. Cross, V. Bakken, C. Adamo, J. Jaramillo, R. Gomperts, R. E. Stratmann, O. Yazyev, A. J. Austin, R. Cammi, C. Pomelli, J. W. Ochterski, R. L. Martin, K. Morokuma, V. G. Zakrzewski, G. A. Voth, P. Salvador, J. J. Dannenberg, S. Dapprich, A. D. Daniels, O. Farkas, J. B. Foresman, J. V. Ortiz, J. Cioslowski, and D. J. Fox. *Gaussian 09, Revision A.02.* Gaussian, Inc., Wallingford CT (2009).

[269] C. Lee, W. Yang, and R. G. Parr. *Development of the Colle-Salvetti correlation-energy formula into a functional of the electron density.* Physical Review B **37**(2), 785 (1988).

[270] A. D. Becke. *Density-functional thermochemistry. III. The role of exact exchange.* The Journal of Chemical Physics **98**(7), 5648 (1993).

[271] P. J. Stephens, F. J. Devlin, C. F. Chabalowski, and M. J. Frisch. *Ab Initio Calculation of Vibrational Absorption and Circular Dichroism Spectra Using Density Functional Force Fields.* The Journal of Physical Chemistry **98**(45), 11623 (1994).

[272] P. J. Hay and W. R. Wadt. *Ab initio effective core potentials for molecular calculations. Potentials for the transition metal atoms Sc to Hg.* The Journal of Chemical Physics **82**(1), 270 (1985).

[273] W. R. Wadt and P. J. Hay. *Ab initio effective core potentials for molecular calculations. Potentials for main group elements Na to Bi.* The Journal of Chemical Physics **82**(1), 284 (1985).

[274] P. J. Hay and W. R. Wadt. *Ab initio effective core potentials for molecular calculations. Potentials for K to Au including the outermost core orbitals.* The Journal of Chemical Physics **82**(1), 299 (1985).

[275] J. Wright. *Gas adsorption on phthalocyanines and its effects on electrical properties.* Progress in Surface Science **31**(1-2), 1 (1989).

[276] A. Dandridge, H. Drescher, and J. Thomas. *British patent 322,169* (1929).

[277] M.-S. Liao and S. Scheiner. *Electronic structure and bonding in metal phthalocyanines, metal=Fe, Co, Ni, Cu, Zn, Mg.* The Journal of Chemical Physics **114**(22), 9780 (2001).

[278] D. Eley. *Phthalocyanines as semiconductors.* Nature **162**, 819 (1948).

[279] D. D. Eley, G. D. Parfitt, M. J. Perry, and D. H. Taysum. *The semiconductivity of organic substances. part 1.* Transactions of the Faraday Society **49**, 79 (1953).

[280] G. Horowitz. *Organic field-effect transistors.* Advanced Materials **10**(5), 365 (1998).

[281] F. Schauer, I. Zhivkov, and S. Nespurek. *Organic phthalocyanine films with high mobilities for efficient field-effect transistor switches.* Journal of Non-Crystalline Solids **266-269**, 999 (2000).

[282] S. Heutz, S. M. Bayliss, R. L. Middleton, G. Rumbles, and T. S. Jones. *Polymorphism in phthalocyanine thin films: Mechanism of the $\alpha \rightarrow \beta$ transition.* The Journal of Physical Chemistry B **104**(30), 7124 (2000).

[283] H. Wang, D. Song, J. Yang, B. Yu, Y. Geng, and D. Yan. *High mobility vanadylphthalocyanine polycrystalline films for organic field-effect transistors.* Applied Physics Letters **90**(25), 253510 (2007).

[284] M. Nakamura and H. Tokumoto. *Molecular arrangement of copper phthalocyanine on Si(001)-(2×1)-H: a high-resolution frictional force microscopy and molecular mechanics study.* Surface Science **398**(1-2), 143 (1998).

[285] H. Engelkamp. *Self-assembly of disk-shaped molecules to coiled-coil aggregates with tunable helicity.* Science **284**(5415), 785 (1999).

[286] M. Craciun, S. Rogge, M.-J. den Boer, S. Margadonna, K. Prassides, Y. Iwasa, and A. Morpurgo. *Electronic transport through electron-doped metal phthalocyanine materials.* Advanced Materials **18**(3), 320 (2006).

[287] N. Karl, K.-H. Kraft, J. Marktanner, M. Münch, F. Schatz, R. Stehle, and H.-M. Uhde. *Fast electronic transport in organic molecular solids?* Journal of Vacuum Science & Technology A: Vacuum, Surfaces, and Films **17**(4), 2318 (1999).

[288] R. A. Street, J. E. Northrup, and A. Salleo. *Transport in polycrystalline polymer thin-film transistors.* Physical Review B **71**(16) (2005).

[289] Z. Bao, A. J. Lovinger, and A. Dodabalapur. *Highly ordered vacuum-deposited thin films of metallophthalocyanines and their applications in field-effect transistors.* Advanced Materials **9**(1), 42 (1997).

[290] H. Gupta, R. K. Bedi, and A. Mahajan. *Characterization of hot wall grown silver phthalocyanine films.* Journal of Applied Physics **102**(7), 073502 (2007).

[291] H. Yamamoto, H. Tada, T. Kawaguchi, and A. Koma. *Epitaxial growth of metalphthalocyanines on selenium-terminated GaAs(111) surfaces.* Applied Physics Letters **64**(16), 2099 (1994).

[292] J. Åhlund, J. Schnadt, K. Nilson, E. Göthelid, J. Schiessling, F. Besenbacher, N. Mårtensson, and C. Puglia. *The adsorption of iron phthalocyanine on graphite: A scanning tunnelling microscopy study.* Surface Science **601**(17), 3661 (2007).

[293] S. R. Wagner, B. Huang, C. Park, J. Feng, M. Yoon, and P. Zhang. *Growth of metal phthalocyanine on deactivated semiconducting surfaces steered by selective orbital coupling.* Physical Review Letters **115**(9) (2015).

[294] Z. Cheng, L. Gao, Z. Deng, Q. Liu, N. Jiang, X. Lin, X. He, S. Du, and H.-J. Gao. *Epitaxial growth of iron phthalocyanine at the initial stage on Au(111) surface.* Journal of Physical Chemistry C **111**(6), 2656 (2007).

[295] Z. Cheng, L. Gao, Z. Deng, N. Jiang, Q. Liu, D. Shi, S. Du, H. Guo, and H.-J. Gao. *Adsorption behavior of iron phthalocyanine on Au(111) surface at submonolayer coverage.* Journal of Physical Chemistry C **111**(26), 9240 (2007).

[296] A. Scarfato, S.-H. Chang, S. Kuck, J. Brede, G. Hoffmann, and R. Wiesendanger. *Scanning tunneling microscope study of iron(II) phthalocyanine growth on metals and insulating surfaces.* Surface Science **602**(3), 677 (2008).

[297] T. G. Gopakumar, T. Brumme, J. Kröger, C. Toher, G. Cuniberti, and R. Berndt. *Coverage-driven electronic decoupling of Fe-phthalocyanine from a Ag(111) substrate.* The Journal of Physical Chemistry C **115**(24), 12173 (2011).

[298] S. R. Wagner, R. R. Lunt, and P. Zhang. *Anisotropic crystalline organic step-flow growth on deactivated Si surfaces.* Physical Review Letters **110**(8) (2013).

[299] S. Yim and T. S. Jones. *Ordered structures of phthalocyanine overlayers on unpassivated InAs and InSb surfaces.* Journal of Physics: Condensed Matter **15**(38), S2631 (2003).

[300] A. Yamashita and T. Hayashi. *Organic molecular beam deposition of metallophthalocyanines for opto-electronics applications.* Advanced Materials **8**(10), 791 (1996).

[301] Y. Naitoh, T. Matsumoto, K.-i. Sugiura, Y. Sakata, and T. Kawai. *Self-assembled stripe structure of zinc–phthalocyanine on graphite surfaces.* Surface Science **487**(1-3), L534 (2001).

[302] T. Wang, J. Yang, H. Wang, F. Zhu, and D. Yan. *Weak epitaxy growth and phase behavior of planar phthalocyanines on p -sexiphenyl monolayer film.* The Journal of Physical Chemistry B **112**(22), 6786 (2008).

[303] J. Yang and D. Yan. *Weak epitaxy growth of organic semiconductor thin films.* Chemical Society Reviews **38**(9), 2634 (2009).

[304] S. R. Wagner and P. Zhang. *Nucleation and evolution of zinc phthalocyanine thin films on the deactivated Si(111)-B $\sqrt{3} \times \sqrt{3}$ R30° surface.* Surface Science **630**, 22 (2014).

[305] S. R. Wagner and P. Zhang. *Formation of highly ordered organic molecular thin films on deactivated Si surfaces studied by scanning tunneling microscopy and low energy electron diffraction.* The Journal of Physical Chemistry C **118**(4), 2194 (2014).

[306] H. Peisert, T. Schwieger, J. M. Auerhammer, M. Knupfer, M. S. Golden, J. Fink, P. R. Bressler, and M. Mast. *Order on disorder: Copper phthalocyanine thin films on technical substrates.* Journal of Applied Physics **90**(1), 466 (2001).

[307] A. S. Milev, N. Tran, G. S. Kamali Kannangara, M. A. Wilson, and I. Avramov. *Polymorphic transformation of iron-phthalocyanine and the effect on carbon nanotube synthesis.* The Journal of Physical Chemistry C **112**(14), 5339 (2008).

[308] T. Kobayashi, Y. Fujiyoshi, F. Iwatsu, and N. Uyeda. *High-resolution TEM images of zinc phthalocyanine polymorphs in thin films.* Acta Crystallographica Section A **37**(5), 692 (1981).

[309] F. Iwatsu. *Size effects on the α-β transformation of phthalocyanine crystals.* The Journal of Physical Chemistry **92**(6), 1678 (1988).

[310] E. Kuzmann, A. Nath, V. Chechersky, S. Li, Y. Wei, X. Chen, J. Li, Z. Homonnay, M. Gál, V. K. Garg, Z. Klencsár, and A. Vértes. *Mössbauer study of oxygenated iron-phthalocyanines, a precursor of magnetic storage material.* In D. C. Cook and G. R. Hoy, eds., *Industrial Applications of the Mössbauer Effect*, pp. 631–639 (Springer Netherlands, Dordrecht, 2002).

[311] A. Hoshino, Y. Takenaka, and H. Miyaji. *Redetermination of the crystal structure of α-copper phthalocyanine grown on KCl.* Acta Crystallographica Section B Structural Science **59**(3), 393 (2003).

[312] M. S. Mindorff and D. E. Brodie. *Some properties of metal-free amorphous phthalocyanine vacuum deposited films.* Canadian Journal of Physics **59**(2), 249 (1981).

[313] R. Gould. *Structure and electrical conduction properties of phthalocyanine thin films.* Coordination Chemistry Reviews **156**, 237 (1996).

[314] Z. Liu, X. Zhang, Y. Zhang, and J. Jiang. *Theoretical investigation of the molecular, electronic structures and vibrational spectra of a series of first transition metal phthalocyanines.* Spectrochimica Acta Part A: Molecular and Biomolecular Spectroscopy **67**(5), 1232 (2007).

[315] S. Ahmadi, M. N. Shariati, S. Yu, and M. Göthelid. *Molecular layers of ZnPc and FePc on Au(111) surface: Charge transfer and chemical interaction.* The Journal of Chemical Physics **137**(8), 084705 (2012).

[316] M. F. Craciun, S. Rogge, and A. F. Morpurgo. *Correlation between molecular orbitals and doping dependence of the electrical conductivity in electron-doped metal−phthalocyanine compounds.* Journal of the American Chemical Society **127**(35), 12210 (2005).

[317] Q. Tang, H. Li, M. He, W. Hu, C. Liu, K. Chen, C. Wang, Y. Liu, and D. Zhu. *Low threshold voltage transistors based on individual single-crystalline submicrometer-sized ribbons of copper phthalocyanine.* Advanced Materials **18**(1), 65 (2006).

[318] H. Wang, F. Zhu, J. Yang, Y. Geng, and D. Yan. *Weak epitaxy growth affording high-mobility thin films of disk-like organic semiconductors.* Advanced Materials **19**(16), 2168 (2007).

[319] D. Song, H. Wang, F. Zhu, J. Yang, H. Tian, Y. Geng, and D. Yan. *Phthalocyanato Tin(IV) dichloride: An air-stable, high-performance, n-type organic semiconductor with a high field-effect electron mobility.* Advanced Materials **20**(11), 2142 (2008).

[320] O. P. Jaseentha and C. S. Menon. *Characterization of optical, electrical and structural properties of silverphthalocyanine thin films.* Journal of Materials Science: Materials in Electronics **19**(7), 602 (2008).

[321] W. Y. Tong, A. B. Djurišić, M. H. Xie, A. C. M. Ng, K. Y. Cheung, W. K. Chan, Y. H. Leung, H. W. Lin, and S. Gwo. *Metal phthalocyanine nanoribbons and nanowires.* The Journal of Physical Chemistry B **110**(35), 17406 (2006).

[322] H. Wang, S. Mauthoor, S. Din, J. A. Gardener, R. Chang, M. Warner, G. Aeppli, D. W. McComb, M. P. Ryan, W. Wu, A. J. Fisher, M. Stoneham, and S. Heutz. *Ultralong copper phthalocyanine nanowires with new crystal structure and broad optical absorption.* ACS Nano **4**(7), 3921 (2010).

[323] Y. Zhang, H. Dong, Q. Tang, S. Ferdous, F. Liu, S. C. B. Mannsfeld, W. Hu, and A. L. Briseno. *Organic single-crystalline p−n junction nanoribbons.* Journal of the American Chemical Society **132**(33), 11580 (2010).

[324] J. Mizuguchi. *Crystal Structure of Magnesiumphthalocyanine and Its Polarized Reflection Spectra.* The Journal of Physical Chemistry A **105**(7), 1121 (2001).

[325] J. Janczak and R. Kubiak. *X-ray single crystal investigations of magnesium phthalocyanine. The 4+1 coordination of the Mg ion and its consequence.* Polyhedron **20**(24-25), 2901 (2001).

[326] J. M. Robertson. *255. An X-ray study of the phthalocyanines. part II. quantitative structure determination of the metal-free compound.* Journal of the Chemical Society (Resumed) pp. 1195–1209 (1936).

[327] J. M. Robertson and I. Woodward. *37. An X-ray study of the phthalocyanines. part III. quantitative structure determination of nickel phthalocyanine.* Journal of the Chemical Society (Resumed) pp. 219–230 (1937).

[328] J. M. Robertson and I. Woodward. *7. An X-ray study of the phthalocyanines. part IV. direct quantitative analysis of the platinum compound.* Journal of the Chemical Society (Resumed) pp. 36–48 (1940).

[329] C. J. Brown. *Crystal structure of β-copper phthalocyanine.* Journal of the Chemical Society A: Inorganic, Physical, Theoretical p. 2488 (1968).

[330] M. K. Friedel, B. F. Hoskins, R. L. Martin, and S. A. Mason. *A new metal(II) phthalocyanine structure: X-ray and Mössbauer studies of the triclinic tin(II) phthalocyanine.* Journal of the Chemical Society D: Chemical Communications (7), 400 (1970).

[331] Y. Iyechika, K. Yakushi, I. Ikemoto, and H. Kuroda. *Structure of lead phthalocyanine (triclinic form).* Acta Crystallographica Section B Structural Crystallography and Crystal Chemistry **38**(3), 766 (1982).

[332] K. Ukei. *Lead phthalocyanine.* Acta Crystallographica Section B Structural Crystallography and Crystal Chemistry **29**(10), 2290 (1973).

[333] K. Ukei. *Electroconductive properties of a one-dimensional conductor lead phthalocyanine.* Journal of the Physical Society of Japan **40**(1), 140 (1976).

[334] A. MacCragh and W. Koski. *The electron paramagnetic resonance spectrum of silver phthalocyanine.* Journal of the American Chemical Society **85**(16), 2375 (1963).

[335] A. Sperl, J. Kröger, and R. Berndt. *Controlled metalation of a single adsorbed phthalocyanine.* Angewandte Chemie **123**(23), 5406 (2011).

[336] R. Strohmaier. *Scanning tunneling microscope investigations of lead–phthalocyanine on MoS_2.* Journal of Vacuum Science & Technology B: Microelectronics and Nanometer Structures **14**(2), 1079 (1996).

[337] B. Koslowski, C. Dietrich, A. Tschetschetkin, and P. Ziemann. *Evaluation of scanning tunneling spectroscopy data: Approaching a quantitative determination of the electronic density of states.* Physical Review B **75**(3) (2007).

[338] M. Ziegler, N. Néel, A. Sperl, J. Kröger, and R. Berndt. *Local density of states from constant-current tunneling spectra.* Physical Review B **80**(12) (2009).

[339] X. W. Tu, G. Mikaelian, and W. Ho. *Controlling single-molecule negative differential resistance in a double-barrier tunnel junction.* Physical Review Letters **100**(12) (2008).

[340] N. P. Guisinger, M. E. Greene, R. Basu, A. S. Baluch, and M. C. Hersam. *Room temperature negative differential resistance through individual organic molecules on silicon surfaces.* Nano Letters **4**(1), 55 (2004).

[341] A. Zhao. *Controlling the kondo effect of an adsorbed magnetic ion through its chemical bonding.* Science **309**(5740), 1542 (2005).

[342] Y. F. Wang, J. Kröger, R. Berndt, H. Vázquez, M. Brandbyge, and M. Paulsson. *Atomic-scale control of electron transport through single molecules.* Physical Review Letters **104**(17) (2010).

[343] A. Sperl, J. Kröger, and R. Berndt. *Demetalation of a single organometallic complex.* Journal of the American Chemical Society **133**(29), 11007 (2011).

[344] J. Repp. *Controlling the charge state of individual gold adatoms.* Science **305**(5683), 493 (2004).

[345] F. Schwarz, Y. F. Wang, W. A. Hofer, R. Berndt, E. Runge, and J. Kröger. *Electronic and vibrational states of single tin–phthalocyanine molecules in double layers on Ag(111).* The Journal of Physical Chemistry C **119**(27), 15716 (2015).

[346] T. G. Gopakumar, F. Müller, and M. Hietschold. *Scanning tunneling microscopy and scanning tunneling spectroscopy studies of planar and nonplanar naphthalocyanines on graphite (0001). Part 1: Effect of nonplanarity on the adlayer structure and voltage-induced flipping of nonplanar tin−naphthalocyanine.* The Journal of Physical Chemistry B **110**(12), 6051 (2006).

[347] S.-E. Zhu, Y.-M. Kuang, F. Geng, J.-Z. Zhu, C.-Z. Wang, Y.-J. Yu, Y. Luo, Y. Xiao, K.-Q. Liu, Q.-S. Meng, L. Zhang, S. Jiang, Y. Zhang, G.-W. Wang, Z.-C. Dong, and J. G. Hou. *Self-decoupled porphyrin with a tripodal anchor for molecular-scale electroluminescence.* Journal of the American Chemical Society **135**(42), 15794 (2013).

[348] Q. Meng, C. Zhang, Y. Zhang, Y. Zhang, Y. Liao, and Z. Dong. *Tunneling electron induced molecular electroluminescence from individual porphyrin J-aggregates.* Applied Physics Letters **107**(4), 043103 (2015).

[349] K. Kuhnke, R. Becker, M. Epple, and K. Kern. *C_{60} exciton quenching near metal surfaces.* Physical Review Letters **79**(17), 3246 (1997).

[350] S. Mühlenberend, M. Gruyters, and R. Berndt. *Fe impurity-induced electronic states at the GaAs(110) surface.* Phys. Rev. B **88**, 115301 (2013).

[351] K. Sato, L. Bergqvist, J. Kudrnovský, P. H. Dederichs, O. Eriksson, I. Turek, B. Sanyal, G. Bouzerar, H. Katayama-Yoshida, V. A. Dinh, T. Fukushima, H. Kizaki, and R. Zeller. *First-principles theory of dilute magnetic semiconductors.* Reviews of Modern Physics **82**(2), 1633 (2010).

[352] T. Jungwirth, J. Sinova, J. Mašek, J. Kučera, and A. H. MacDonald. *Theory of ferromagnetic (III,Mn)V semiconductors.* Reviews of Modern Physics **78**(3), 809 (2006).

[353] A. M. Yakunin, A. Y. Silov, P. M. Koenraad, J. H. Wolter, W. Van Roy, J. De Boeck, J.-M. Tang, and M. E. Flatté. *Spatial structure of an individual Mn acceptor in GaAs.* Physical Review Letters **92**(21) (2004).

[354] D. Kitchen, A. Richardella, J.-M. Tang, M. E. Flatté, and A. Yazdani. *Atom-by-atom substitution of Mn in GaAs and visualization of their hole-mediated interactions.* Nature **442**(7101), 436 (2006).

[355] J. K. Garleff, C. Çelebi, W. Van Roy, J.-M. Tang, M. E. Flatté, and P. M. Koenraad. *Atomically precise impurity identification and modification on the manganese doped GaAs(110) surface with scanning tunneling microscopy.* Physical Review B **78**(7) (2008).

[356] J.-M. Jancu, J.-C. Girard, M. O. Nestoklon, A. Lemaître, F. Glas, Z. Z. Wang, and P. Voisin. *STM images of subsurface Mn atoms in GaAs: Evidence of hybridization of surface and impurity states.* Physical Review Letters **101**(19) (2008).

[357] T. O. Strandberg, C. M. Canali, and A. H. MacDonald. *Magnetic properties of substitutional Mn in (110) GaAs surface and subsurface layers.* Physical Review B **80**(2) (2009).

[358] P. Mahadevan and A. Zunger. *First-principles investigation of the assumptions underlying model-Hamiltonian approaches to ferromagnetism of 3 d impurities in III-V semiconductors.* Physical Review B **69**(11) (2004).

[359] A. Richardella, D. Kitchen, and A. Yazdani. *Mapping the wave function of transition metal acceptor states in the GaAs surface.* Physical Review B **80**(4) (2009).

[360] J. K. Garleff, A. P. Wijnheijmer, A. Y. Silov, J. van Bree, W. Van Roy, J.-M. Tang, M. E. Flatté, and P. M. Koenraad. *Enhanced binding energy of manganese acceptors close to the GaAs(110) surface.* Physical Review B **82**(3) (2010).

[361] G. Mahieu, B. Grandidier, D. Deresmes, J. P. Nys, D. Stiévenard, and P. Ebert. *Direct evidence for shallow acceptor states with nonspherical symmetry in GaAs.* Physical Review Letters **94**(2) (2005).

[362] S. Loth, M. Wenderoth, L. Winking, R. G. Ulbrich, S. Malzer, and G. H. Döhler. *Probing semiconductor gap states with resonant tunneling.* Physical Review Letters **96**(6) (2006).

[363] J. Bocquel, V. R. Kortan, C. Åžahin, R. P. Campion, B. L. Gallagher, M. E. Flatté, and P. M. Koenraad. *Core-state manipulation of single Fe impurities in GaAs with a scanning tunneling microscope.* Physical Review B **87**(7) (2013).

[364] T. Matsui, C. Meyer, L. Sacharow, J. Wiebe, and R. Wiesendanger. *Electronic states of Fe atoms and chains on InAs(110) from scanning tunneling spectroscopy.* Physical Review B **75**(16) (2007).

[365] A. Kahn. *Semiconductor surface structures.* Surface Science Reports **3**(4-5), 193 (1983).

[366] Z. F. Zheng, M. B. Salmeron, and E. R. Weber. *Empty state and filled state image of ZnGa acceptor in GaAs studied by scanning tunneling microscopy.* Applied Physics Letters **64**(14), 1836 (1994).

[367] R. de Kort, M. C. M. M. van der Wielen, A. J. A. van Roij, W. Kets, and H. van Kempen. *Zn- and Cd-induced features at the GaAs(110) and InP(110) surfaces studied by low-temperature scanning tunneling microscopy.* Physical Review B **63**(12) (2001).

[368] A. Höglund, S. Mirbt, C. W. M. Castleton, and M. Göthelid. *Breakdown of cation vacancies into anion vacancy-antisite complexes on III-V semiconductor surfaces.* Physical Review B **78**(15) (2008).

[369] A. Ionescu, M. Tselepi, D. M. Gillingham, G. Wastlbauer, S. J. Steinmüller, H. E. Beere, D. A. Ritchie, and J. A. C. Bland. *Submonolayer growth of Fe on a Ga As (100) − 2 × 6 reconstructed surface.* Physical Review B **72**(12) (2005).

[370] K. Stiles. *Trends in temperature-dependent Schottky barrier formation: The Ga/GaAs and Mn/GaAs interfaces.* Journal of Vacuum Science & Technology B: Microelectronics and Nanometer Structures **6**(4), 1392 (1988).

[371] H. Fu, L. Ye, K. Zhang, and X. Xie. *Chemisorption of Mn on a GaAs(110) surface.* Surface Science **341**(3), 273 (1995).

[372] S. C. Erwin, S.-H. Lee, and M. Scheffler. *First-principles study of nucleation, growth, and interface structure of Fe/GaAs.* Physical Review B **65**(20) (2002).

[373] S. Mirbt, B. Sanyal, C. Isheden, and B. Johansson. *First-principles calculations of Fe on GaAs(100).* Physical Review B **67**(15) (2003).

[374] H. Zheng, A. Weismann, and R. Berndt. *Manipulation of subsurface donors in ZnO.* Physical Review Letters **110**(22) (2013).

[375] R. M. Feenstra, G. Meyer, F. Moresco, and K. H. Rieder. *Low-temperature scanning tunneling spectroscopy of n -type GaAs(110) surfaces.* Physical Review B **66**(16) (2002).

[376] R. J. Elliott. *Theory of the effect of spin-orbit coupling on magnetic resonance in some semiconductors.* Phys. Rev. **96**(2), 266 (1954).

[377] Y. Yafet. *Conduction electron spin relaxation in the superconducting state.* Phys. Lett. A **98**(5-6), 287 (1983).

[378] P. H. Song and K. W. Kim. *Spin relaxation of conduction electrons in bulk III-V semiconductors.* Phys. Rev. B **66**, 035207 (2002).

[379] J. H. Jiang and M. W. Wu. *Electron-spin relaxation in bulk III-V semiconductors from a fully microscopic kinetic spin bloch equation approach.* Phys. Rev. B **79**, 125206 (2009).

[380] D'yakonov, M.I. and Perel', V.I. *On spin orientation of electrons in interband absorption of light in semiconductors.* Zh. Eksp. Teor. Fiz. **60**, 1954 (1971).

[381] D'yakonov, M.I. and Perel, V.I. *Spin relaxation of conduction electrons in non-centrosymmetric semiconductors.* Sov. Phys. Sol. State **13**(12), 3023 (1971).

[382] Bir, G.L., Aronov, A.G., and Pikus, G.E. *Spin relaxation of electrons due to scattering by holes.* JETP **42**, 705 (1975).

[383] G. W. Gobeli and F. G. Allen. *Photoelectric properties of cleaved GaAs, GaSb, InAs, and InSb surfaces; comparison with Si and Ge.* Physical Review **137**(1A), A245 (1965).

[384] A. Huijser and J. Van Laar. *Work function variations of gallium arsenide cleaved single crystals.* Surface Science **52**(1), 202 (1975).

[385] G. M. Guichar, C. A. Sebenne, and G. A. Garry. *Intrinsic and defect-induced surface states of cleaved GaAs(110).* Physical Review Letters **37**(17), 1158 (1976).

[386] A. Huijser, J. van Laar, and T. van Rooy. *Electronic surface properties of uhv-cleaved III-V compounds.* Surface Science **62**(2), 472 (1977).

[387] D. R. Lide and Chemical Rubber Company, eds. *CRC handbook of chemistry and physics: a ready-reference book of chemical and physical data* (CRC Press, Boca Raton, Fla., 1995), 76. ed., 1995-1996 ed.

[388] Q. M. Zhang, H. Li, M. Poh, F. Xia, Z.-Y. Cheng, H. Xu, and C. Huang. *An all-organic composite actuator material with a high dielectric constant.* Nature **419**(6904), 284 (2002).